FINITE ELEMENT ANALYSIS OF MODIFIED HIGH STRENGTH ALUMINIUM ALLOYS USING PROGRESSIVE FAILURE ALGORITHM

By

Md. Faisal Hossain
STUDENT NUMBER 1015112019

A thesis paper submitted in partial fulfillment of the requirements for the award of

Master of Science in

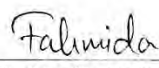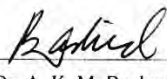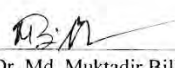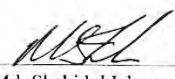Materials and Metallurgical Engineering

DEPARTMENT OF MATERIALS AND METALLURGICAL ENGINEERING

BANGLADESH UNIVERSITY OF ENGINEERING AND TECHNOLOGY

March, 2020

The thesis titled "Finite Element Analysis of Modified High Strength Aluminium Alloys Using Progressive Failure Algorithm" submitted by Md. Faisal Hossain, Roll No.: 1015112019, Session: October 2015, has been accepted as satisfactory in partial fulfillment of the requirement for the degree of Master of Science in Materials and Metallurgical Engineering on 11th March, 2020.

BOARD OF EXAMINERS

(i)   Dr. Kazi Md. Shorowordi   Chairman
        Professor   (Supervisor)
        Dept of Materials and Metallurgical Engg.,
        BUET, Dhaka-1000.

(ii)   Dr. Fahmida Gulshan   Member
        Professor and Head   (Ex-Officio)
        Dept of Materials and Metallurgical Engg.,
        BUET, Dhaka – 1000.

(iii)   Dr. A. K. M. Bazlur Rashid   Member
        Professor
        Dept of Materials and Metallurgical Engg.,
        BUET, Dhaka-1000.

(iv)   Dr. Md. Muktadir Billah   Member
        Assistant Professor
        Dept of Materials and Metallurgical Engg.,
        BUET, Dhaka-1000.

(v)   Dr. Md. Shahidul Islam   Member
        Professor   (External)
        Dept. of Naval Architecture and Marine Engg.,
        BUET, Dhaka-1000.

CANDIDATE'S DECLARATION

It is hereby declared that this thesis or any part of it has not been submitted elsewhere for the award of any degree or diploma.

....
Md. Faisal Hossain
1015112019

ACKNOWLEDGEMENTS

Abstract

The primary objective of this thesis was to develop a reliable finite element analysis procedure to model the complete fracture of ductile specimens using the progressive degradation of the material stiffness algorithm under tensile load. The ductile specimens in this study were three different aluminum 7075 alloys. Another objective was to establish the structure and property relationship of these alloys. The progressive failure algorithm used here was based on the assumption that the material behaves like a stable progressively fracturing solid. The stiffness reduction was carried out at the integration gauss points of the finite element mesh depending on the mode of failure. A number of material properties were necessary for such simulation to carry out and experimentation of the alloys were needed to evaluate these properties. The actual tensile tests data were applied to the finite element simulation. A renowned finite element analysis software Abaqus was used in this study. Besides, different tests were carried out to evaluate the structure-property relationship. It was found that the addition of alloying elements changed these alloys to obtain higher strength, hardness, and toughness. Effects of different mesh sizes on the mode of failure were also investigated. As the mesh sizes became smaller the time required for simulation increased but yielded results closer to the actual tensile test failure. Selected simulation results were verified by comparing true stress with von Mises stress in Abaqus. Computed stress triaxialities were also evaluated in various points on the modeled tensile test samples. Highest stress triaxialities was found near the failure zone of these modeled samples. The verified simulation method has a great importance in practical design of structures and materials.

Table of Contents

List of Figures

List of Tables

Abbreviations

FEA	Finite element analysis
SEM	Scanning electron microscope
DSC	Differential scanning calorimetry
XRD	X-ray powder diffraction
XRF	X-ray fluorescence
EDS	Energy dispersive x-ray spectroscopy
GP	Guinier-Preston
2D	Two dimensional
3D	Three dimensional
PFZ	Precipitation free zones
SSSS	Super saturated solid solutions
CRSS	Critical resolved shear stress
DAS	Dendrite arm spacing
FEM	Finite element method
DOF	Degree of freedom
MPa	Mega Pascal
GPa	Giga Pascal
C3D8	8-noded linear brick element
C3D8R	8-noded linear brick element with reduced integration
JC	Johnson-Cook
CAE	Computer aided engineering

Nomenclature

σ_y	Yield stress
τ_c	Shear stress
η phase	$MgZn_2$
S phase	Al_2CuMg
θ phase	Al_2Cu
T phase	$AlMg_4Zn_{11}$
E	Young's modulus
$\in^{plastic}$	Logarithmic plastic strain
$\bar{\epsilon}_f$	Equivalent plastic strain to fracture
δ	Engineering strain
σ_e	Engineering stress
P	Hydrostatic pressure
σ_m	Hydrostatic stress
S	Deviatoric stress
$\bar{\sigma}$	Equivalent von Mises stress
η	Stress triaxiality
D	Damage variable
Δt_{cr}	Critical time increment size
ω_{max}	Maximum natural frequency
ρ	Density
σ	Stress tensor

CHAPTER 1
Introduction

1.1 Background

Aluminum alloys are the key materials in aerospace and automobile industries [1, 2]. Aluminum gets attention because it is light weight and has adequate mechanical properties for many industrial applications. Among the common aluminum alloys, aluminium 7075 has the highest strength to weight ratio and is increasingly used in manufacturing of different automobile and aircraft components [3, 4]. Presence of alloying elements viz Zn, Er, Cr (zinc, erbium and chromium) and effective heat-treatment, result higher strength in these alloys [5-8]. Al 7075 alloy modified with nickel has excellent properties which are attractive for the strength related applications [9]. Farkoosh et al. [10], found that the addition of Ni (0.1-1 wt.%) in Al-Zn-Mg-Cu alloys influence the formation of Al-Ni-Cu phases which in turn increases the strength of these alloys. Addition of boron in Al 7075 increases the strength by acting as a grain refiner. Murty et al. [11], observed that the boron as borides does much better grain refinement against other grain refiners such as titanium when elements like Cr, Zr, Si, Li are present. Boron as nano carbides also increases the overall properties of Al 7075 [12]. These high strength alloys are of high importance and are selected by the weight of its performance, cost, reliability and reusability. And thus simulation comes into play its role. M

Being such a highly important alloy, for the evaluation of its properties, tensile test until fracture in different physical conditions are frequently performed. A properly developed tensile simulation of this material until fracture using failure model in finite element analysis will allow researchers to have an in depth understanding of this material [13-15]. Selecting proper alloy modifier, obtaining reliable experimental results and then performing appropriate simulation thus demand high attention.

Although, there are many damage models it is reported that the phenomenological damage models (i.e. Johnson cook, ductile damage models) are the best to employ when experimental data are at hand since the continuum damage mechanics shows

systematically the effects of damage on the mechanical properties of materials and structures as well as the influence of external conditions and damage itself and thus accurately representing the experimental situations [14, 16]. Many researchers tried to implement empirical and physical models to replicate experimental conditions [17, 18] but these models require tons of experimental data to find accurate representation of the real experiment [19]. On the other hand, phenomenological models such as Johnson-Cook, Zerilli–Armstrong, Cowper–Symonds showed somewhat realistic simulation results with very few variables [20-22]. K.K. Pathak et al. [23], modified Johnson-Cook model to accurately simulate hot deformation processing. Thus, phenomenological models have been successfully implemented in the simulations. As ductile damage model is a phenomenological model, it also being used in various simulations using finite element analysis software like Abaqus [24, 25]. Recently J. Ruzicka et al. [26] identified the ductile damage parameters required for a tensile test before progressive damage through stiffness reduction starts but a simulation with complete fracture model using ductile damage phenomenological model on Al 7075 alloys is yet to be attempted. In the following sections a fully developed uniaxial tensile test simulation using progressive failure algorithm through gradual material stiffness degradation by implementing ductile damage phenomenological model until failure was used to obtain an accurate realistic simulation model for different Al 7075 alloys.

The key challenges here were choosing the right damage criterion and the proper meshing of the specimen. Through the use of meshing in a planar tensile specimen it is evident that different size of meshing shows different results in the simulation [27]. Most of the time using finer mesh means that the result would converge to the real experiments but that also means higher computational power. So, a meshing should be such that it matches the realistic data but not too much fine that it consumes unnecessarily high amount of computational energy [27].

1.2 Aims and Objectives

The principle objective of the work was to make a proper tensile test simulation of Al 7075 alloys until failure using the experimental data with progressive failure algorithm. And to perform this simulation Al 7075 alloy, Ni added Al 7075 alloy and Ni and B added Al 7075 alloy were to be processed and characterized. Another objective in this study was to establish structure-property relationship of these alloys. In this context, the specific aims of the work were as follows.

i. Casting and hot rolling of three different variations of Al 7075 alloys.

ii. Establishment of a tensile simulation model until fracture by finite element analysis using progressive failure algorithm with the data accumulated from experiments and making a comparison with real world tensile fracture scenarios.

The anticipated outcome of this research was that a tensile simulation until fracture would be established using the properties of various Al 7075 alloys. Successful simulation mimicking the original test would allow researchers and engineers to model and analyze complex structural designs.

1.3 Thesis Outline

The present thesis is divided into eight chapters:

- Chapter 1 - Introduction - presentation of the thesis background, aims and objectives behind the work and a brief outline of this work.

- Chapter 2 – Review on Al 7075 alloys - introductory concepts and background theory about aluminium and aluminium alloys having special attention to aluminium 7075 alloys.

- Chapter 3 - Experimental Procedure - descriptions of the used methods, materials, equipment and techniques. Conditions for every test performed are presented. This chapter includes preparation of alloys and various tests such as hardness, tensile test, density calculation, Optical microscopy, SEM and EDS, DSC, XRF, and XRD.

- Chapter 4 - Experimental Results and Discussion - presentation of experimental results and analysis of results obtained in the experiments are included in chapter four.

- Chapter 5- A Brief Review on Progressive Damage- theory behind the tensile test simulation and how it fails focusing on the explicit analysis and the stiffness degradation by the ductile damage progressive failure algorithm in Abaqus.

- Chapter 6 - Finite Element Model Development - includes all the details of a tensile test simulation, on a test specimen, with the finite element method by using varying mesh types and sizes to develop a practical method of simulation using experimental data.

- Chapter 7- FEA Results- includes the results obtained from the simulation and matching the simulation with real results and a brief outline of how stress triaxiality plays roles on the failure process.

- Chapter 8 – Conclusions and Recommendations - summary of the important points of the analysis made on the results chapter, suggested improvements and follow-up work that can be made on this topic.

CHAPTER 2
Review on Aluminium 7075 Alloys

2.1 Overview on Aluminium Alloys:

The use of aluminum and its alloys has increased significantly over the past several years in numerous applications, successfully replacing iron and steel at some applications. The principal areas in which aluminum has increased in importance are the automotive and aerospace industries, where by means of the smelting of the metal and the carrying out of suitable heat treatments, the manufacturing of cylinder heads, engine blocks, pistons, intake manifolds, and other parts is made possible. In recent years, the development of diesel and direct fuel injection gasoline engines with high specific powers have resulted in a marked performance impact on piston materials due to increased combustion pressure and piston temperature [28-30]. The reduction in fuel consumption is considered to be not only a decisive economical factor but also a significant environmental advantage obtainable via the associated reduction in the production of exhaust gases [31].

With the intention of reducing vehicle weight in the automotive industry, and in aerospace industry many iron-based components are in the process of being replaced with parts made of aluminum-based alloys since the density of aluminum is one-third that of steel [32, 33]. The proposed benefits of using aluminum in auto body parts may be listed as: fuel economy improvement, as safe as steel, improved vehicle performance, cost-effective *vs.* other fuel saving technologies, lower life-cycle CO_2 than steel, and compatibility with existing stamping assets. Figure 2.1 indicates the growing trend of aluminum over steel. From 2005 to 2015 aluminum volume sales have grown twice as fast as those of steel — up 82 percent versus 41 percent. And it is expected that in the subsequent 10 years, aluminum sales will increase by another 50 percent [31].

Global growth of steel vs. aluminum

Steel market volume
(in million tons)

2005: 1,148 → +41% → 2015: 1,623 → +24% → 2025: 2,017

Aluminum market volume
(in million tons)

2005: 32 → +82% → 2015: 58 → +50% → 2025: 87
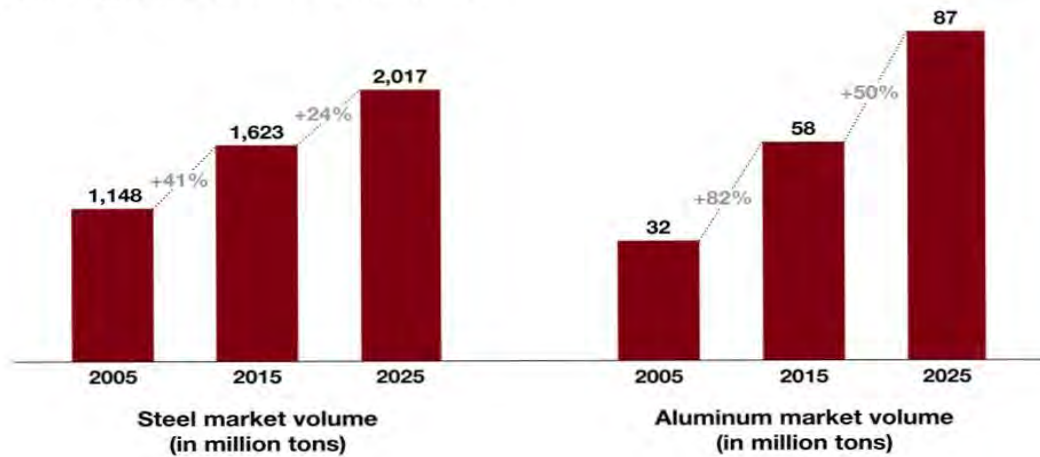
Figure 2.1 Global growth of steel versus aluminium.

2.1.1 Properties:

The low density and high strength-to-weight ratio are the best known properties which distinguish aluminum and its alloys from many other common engineering metals. Aluminum also has high corrosion resistance, ductility, thermal and electrical conductivity and an attractive surface finish. Pure aluminum has a relatively low yield stress and ultimate tensile stress. To increase its strength, aluminum is usually alloyed with other elements such as zinc, copper and magnesium [34].

2.1.2 Aluminium in Aerospace Application:

The high specific properties of some aluminium alloys, called "high strength" aluminium alloys make them perfectly suitable to be used in aircrafts. Figure 2.2 shows the location of aluminium alloy components in a commercial aircraft, showing that aluminium is mainly present in the fuselage and in the wings. Those parts are defined in Figure 2.2. Each component is subjected to different conditions (mechanical, physical) and requires specific material properties (specifications). The main aluminium alloys that are used in commercial aircrafts are age-hardened 2xxx (Al-Cu) and 7xxx (Al-Zn-Mg-Cu) series alloys (Fig. 2.2). For example, 2xxx alloys are used in the fuselage whereas, 7xxx alloys are mainly used in the upper wings [35].
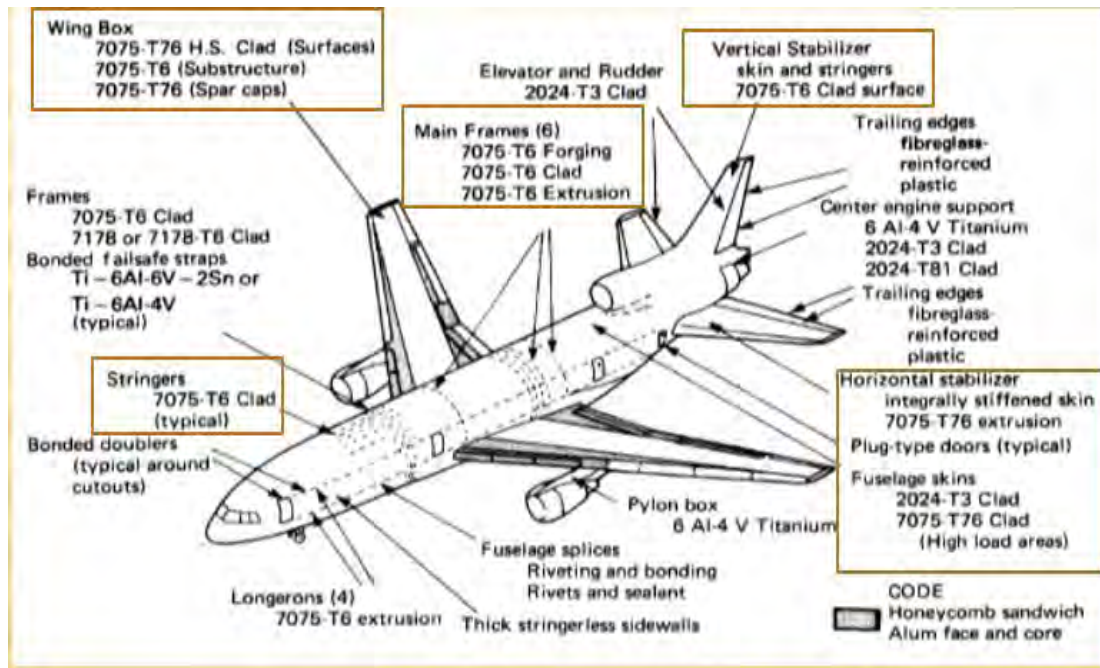
Figure 2.2 Aluminium alloy components in a commercial airplane.

2.1.3 Aluminium Alloy Categories

Aluminium alloys may be divided into two broad classes: cast and wrought products. Then these two classes can be further subdivided on alloys based on their chemical composition and on temper designation. The temper designations refer to the condition of the alloy i.e. amount of cold work that was applied to the alloy or the nature of its heat treatment [36]. The aluminum association (AA), maintains an internationally recognized designation system for each category, described in the American National Standard Institute (ANSI H35.1), Alloy and Temper Designation Systems for Aluminum [36-38]. In this system a four-digit number is assigned to each alloy [36-38]. After these digits a hyphen and the basic temper designation follows which indicates the mechanical and heat treatment to which the alloy has been subjected to [36-38]. For wrought alloys, a four-digit system is used to produce a list of wrought composition families as shown below:

➢ 1xxx: Controlled unalloyed (pure) composition.

➢ 2xxx: Alloys in which copper is the principal alloying element, although other elements, like magnesium, may be specified.

➢ 3xxx: Alloys in which manganese is the principal alloying element.

➢ 4xxx: Alloys in which silicon is the principal alloying element.

➢ 5xxx: Alloys in which magnesium is the principal alloying element.

➢ 6xxx: Alloys in which magnesium and silicon are the principal alloying elements.

- 7xxx: Alloys in which zinc is the principal alloying element (although other elements, such as copper, magnesium, chromium, and zirconium, may be specified).
- 8xxx: Alloys characterizing miscellaneous compositions. The 8xxx series alloys may contain appreciable amounts of tin, lithium, and/or iron.
- 9xxx: Reserved for future use.

Wrought alloys that are heat treatable aluminum alloys are the 2xxx, 6xxx, 7xxx, and some of the 8xxx alloys. Casting compositions are described by a three-digit system followed by a decimal value. The decimal .0 in all cases pertains to casting alloy limits. Decimals .1 and .2 refers to the ingot compositions [39]. Alloy families for casting compositions include the following:

- 1xx.x: Controlled unalloyed (pure) compositions.
- 2xx.x: Copper is the principal alloying element. Other alloying elements may be specified.
- 3xx.x: Alloys in which silicon is the principal alloying element. The other alloying elements such as copper and magnesium are specified.
- 4xx.x: Silicon is the principal alloying element.
- 5xx.x: Magnesium is the principal alloying element.
- 6xx.x: Unused.
- 7xx.x: Zinc is the principal alloying element. Other alloying elements such as copper and magnesium may be specified.
- 8xx.x: Tin is the principal alloying element.
- 9xx.x: Unused Heat-treatable casting alloys include the 2xx, 3xx, and 7xx series.

2.2 Heat Treatment of Aluminium Alloys

Heat treating process refers to the heating and cooling operations that are performed for the purpose of changing the mechanical properties, the metallurgical structure or the residual stress state of a metal product. But for aluminium alloys it is usually restricted to the operations employed to increase the mechanical properties of the precipitation-hardenable wrought and cast alloys [40]. One essential attribute of a precipitation-hardening alloy system is a temperature dependent equilibrium, solid solubility characterized by increasing solubility with increasing temperature [39].

The solubility-temperature relationship required for precipitation hardening of aluminum is illustrated by the Al-Zn system in Figure 2.3. The equilibrium solid solubility of zinc in aluminum increases as temperature increases. At temperatures above the lower curve the zinc is completely soluble, and when the alloy is held at such temperatures for sufficient time to allow diffusion, zinc will be dissolved completely into solid solution. When such an alloy is converted to all solid solution by holding above the solvus temperature and then the temperature is decreased to below the solvus, the solid solution becomes supersaturated and the second phase tends to form by solid-state precipitation at a proper temperature [41].
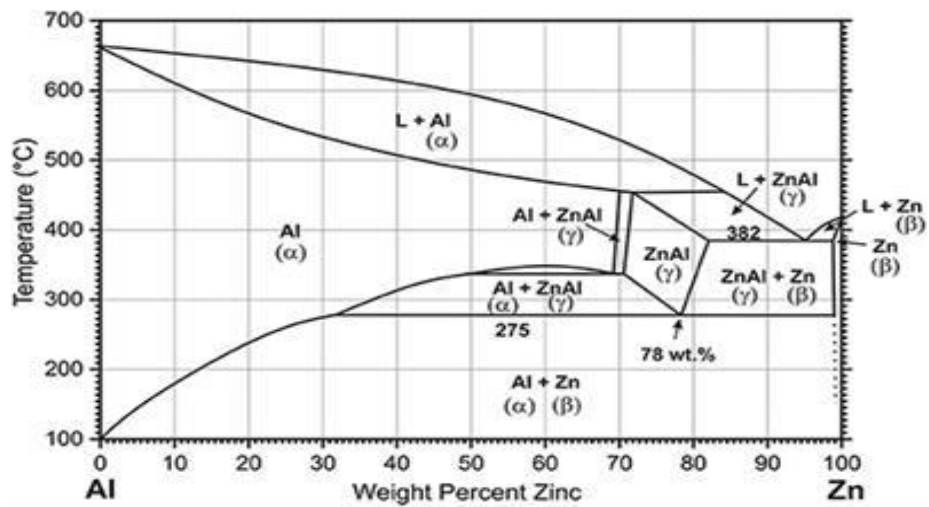
Figure 2.3 Aluminium-Zinc phase diagram.

In alloys of the Al-Zn-Mg system, a succession of precipitates is developed from a rapidly cooled supersaturated solid solution. These precipitates develop sequentially either with increasing temperature or with increasing time at temperatures between room temperature and the solvus. The several stages are listed in table 2.1 [40].

Table 2.1 Several stages of precipitate.

Precipitates	Actions
No precipitate	Super saturated solid solution
GP zones	Spherical GP zones
η	Hexagonal $MgZn_2$
Γ	Semi coherent hexagonal $Mg_{32}(AL, Zn)_{49}$
T	Incoherent cubic $Mg_{32}(AL, Zn)_{49}$

Commercial alloys whose strength and hardness can be significantly increased by heat treatment include 2xxx, 6xxx and 7xxx series wrought alloys and 2xx.O, 3xx.O and 7xx.0 series casting alloys. Some of these contain only copper, or copper and silicon, as the primary strengthening alloy addition(s). Most of the heat treatable alloys, however, contain combinations of magnesium with one or more of the elements copper, silicon and zinc. The addition of small amounts of magnesium in addition with any of these elements accelerates the strength changes in precipitation hardening [40]. Most of the heat treatable aluminum alloy systems exhibit multistage precipitation and undergo accompanying strength changes [40]. Precipitation heat treatments generally require a lot of time and must be done in relatively low temperature. On the other hand, larger particles of precipitate result from longer times and higher temperatures which detrimentally affect the overall strength. So, the objective here is to select a heat treatment cycle that produces optimum precipitate size and distribution pattern. [41].

To recap, heat treatment to increase strength of aluminum alloys is a three-step process:

1. Solution heat treatment: To dissolute the soluble phases in the solid solution.

2. Quenching: To create super saturation.

3. Ageing: precipitation of solute atoms either at room temperature or elevated temperature.

2.2.1 Solution Heat Treating

The objective of solution heat treatment is to take the maximum practical amounts of the soluble hardening elements into solid solution. The process consists of soaking the alloy at a temperature sufficiently high and for a time long enough to achieve a nearly homogeneous solid solution [40].

2.2.2 Solution Treating Time

The time required at solution heat-treating temperature to achieve a practical degree of homogeneous solution of the soluble phase constituents is a function of microstructure before heat treatment [39]. Time for solution heat treatment should be such to avoid overheating or under heating. Proper solution heat treatment of the

aluminium alloys requires an expert knowledge of the alloy being treated plus the correct heat treatment plan [40].

2.2.3 Quenching

To attain a proper precipitation, it is necessary to cool down the piece as fast as possible so that the microstructure remain super saturated. Most frequently, parts are quenched by immersion in cold water [41]. To obtain proper precipitation the time required for transfer of sample from the furnace to the quenching medium must be short and the heat-absorption capacity and rate of flow of the quenching medium be such that little or no precipitation occurs during cooling [41]. Table 2.2 shows the typical solution and precipitation heat treatments for aluminum 7075 alloy products.

Table 2.2 Typical solution and precipitation heat treatments for aluminum 7075 alloy products.

Alloy	Product Form	Solution Heat Treatment			Precipitation Heat Treatment			
		Metal Temperature		Temper Design.	Metal Temperature		Time (h)	Temper Design.
		C	F		C	F		
7075	Sheet	480	900	W	120	250	24	T6
					120	250	24	T62
	Plate	480	900	W	120	250	24	T62
				W51	120	250	24	T651
	Rolled or cold finished wire, rod and bar	490	915	W	120	250	24	T6
					120	250	24	T62
				W51	120	250	24	T651
	Extruded rod, bar, shapes and tube	465	870		120	250	24	T6
					120	250	24	T62
				W510	120	250	24	T6510
				W511	120	250	24	T6511
	Drawn tube	465	870	W	120	250	24	T6
					120	250	24	T62
	Die Forgings	470	880	W	120	250	24	T6
	Hand Forgings	470	880	W	120	250	24	T6
				W52	120	250	24	T652
	Rolled rings	470	880	W	120	250	24	T6

2.2.4 Removing Residual Stress

Immediately after being quenched, most aluminum alloys are nearly as ductile as they are in the annealed condition. Consequently, parts are formed and straightened in this temper. Moreover, in industries, controlled mechanical deformation is the most common method of reducing residual quenching stresses [41].

2.2.5 Natural Ageing

The highly alloyed members of the *6xxx* wrought series, the copper containing alloys of the 7*xxx* group, and all of the 2xxx alloys are almost always solution heat treated and quenched. Among these alloys natural ageing tempers (T3 and T4 types) that are characterized by high ratios of tensile to yield strength, high fracture toughness and high resistance to fatigue. In these tempers the relatively high super saturation of atoms and vacancies retained by rapid quenching causes rapid formation of GP zones and strength increases rapidly, attaining nearly maximum stable values in a short time [41].

2.2.6 Precipitation Heat Treatment

In aluminum alloys the mechanical properties and other characteristics change continuously with time and temperature; to produce a combination of properties corresponding to specific alloy-temper combination requires one or more coordinated combinations of time and temperature [41].

The T tempers for heat treatable alloys may have from one to five digits following the T. The first digit after the T always indicates the basic type of treatment, and the second to fifth, if they are used, indicate whether the product was stress relieved and, if so, how it was stress relieved, and whether any other special treatments were given [41]. The first digit after the T may be any of the following:

T1: Indicates that the alloy has been cooled directly from some high-temperature hot-working process such as rolling or extrusion and then naturally aged to a stable condition. As a result, it has received an "effective heat treatment," but it has not received any other processing.

T2: Indicates that the alloy has been cooled from some high temperature hot-working process such as rolling or extrusion and then cold worked before being naturally aged to a stable condition. Here again, the alloy has received an "effective heat treatment" as a result of the high-temperature treatment, but in this case, it has been cold worked sufficiently to increase its strength.

T3: Indicates the alloy has been given a solution heat treatment following hot working, quenching, cold working, and being naturally aged to a stable condition.

T4: Indicates the alloy has been given a solution heat treatment and, without any cold work, naturally aged to a stable condition.

T5: Indicates the alloy has been cooled from a high-temperature shaping process, usually extrusion, and then, without any intermediate cold work, is artificially aged. The artificial aging consists of holding at a sufficiently high temperature and sufficiently long time to permit precipitation.

T6: Indicates the alloy has been solution heat treated and, without any significant cold working, artificially aged to achieve precipitation hardening. If there is any straightening or flattening to meet dimensional tolerances, it is not sufficient to be recognized with higher mechanical property limits.

T7: Indicates the alloy has been solution heat treated and, without any significant cold working, aged in a furnace to an overaged (i.e., past peak strength) condition (also sometimes referred to as stabilized).

T8: Indicates the alloy has been solution heat treated, cold worked for strain hardening, and then artificially aged to achieve precipitation hardening.

T9: Indicates the alloy has been solution heat treated, artificially aged to achieve precipitation hardening, and then cold worked to improve its strength.

T10: Indicates the alloy has been cooled from a high-temperature shaping process such as extrusion, cold worked, and then artificially aged for precipitation hardening.

2.3 Effect of Alloying Element

The effect of the addition of alloying elements on the properties of materials is well documented in the literature. In the following subsections, the alloying elements normally used, their characteristics and their effects on aluminum alloys will be presented.

2.3.1 Boron

Boron is used in aluminum and its alloys mainly as a grain refiner. It may be used alone or with other elements such as titanium. It is also used to increase electrical conductivity of the aluminium alloys and in certain atomic energy application as boron has high-neutron-capture cross section [40-42].

2.3.2 Carbon

Carbon is commonly found in nature. In Al 7075 carbon usually tends to form compounds with aluminium by forming carbides Al_4C_3. But they also form carbides with other elements in Al 7075 alloys such as boron, oxygen and titanium. These carbides tend to decompose in the presence of water which may rise to surface pitting [40].

2.3.3 Nickel

The solid solubility of nickel in aluminum is very little (around 0.04%). After this nickel forms insoluble hard intermetallic, usually with iron, copper and aluminium. Nickel as an intermetallic increases the strength of high-purity aluminum up to 2 percent but reduces ductility. Nickel is also used in aluminium alloys due to its high temperature mechanical properties [42].

2.3.4 Chromium

Chromium is found as a minor impurity in commercially pure aluminum. It has a large effect on electrical resistivity. Chromium is a common addition in aluminum-magnesium-zinc groups, in which it is added in amounts generally not exceeding 0.35% [42]. Chromium has a slow diffusion rate and forms finely dispersed phases in wrought products. These dispersed phases inhibit nucleation and grain growth. Thus, chromium is used to control grain structure, to prevent grain growth in aluminum-magnesium-zinc alloys [42].

2.3.5 Copper

Copper in aluminum alloys are mainly added for the benefit of strength increases in aluminium alloys by precipitation strengthening. Addition of copper create some excellent heat treatable alloys such as 2xxx Al alloys. This strength increase sometimes come with reduced ductility and poor corrosion resistance [42, 43].

2.3.6 Zirconium

Zirconium (Zr) added to increase the strength of aluminum alloys. Zirconium is also used in a wide selection of aluminum alloys to control the microstructure and mechanical properties [44, 45]. The Al_3Zr particles are resistant to dissolution and

coarsening, so it controls the evolution of the grain and sub-grain structure, thus it is possible to enhance and maintain the alloy strength and ductility [46-48].

2.3.7 Silicon

Silicon is normally found as an impurity in aluminium alloys (except in 6xxx alloys where Si is used to produce Mg_2Si). It increases the strength in cast alloys, mainly by increasing the castability and fluidity of the molten alloy and thus the soundness of the castings, but with some loss of ductility [49-51].

2.4 Al-Zn-Mg-Cu Alloys

The Al-Zn-Mg-Cu (7000 series) alloys are age-hardenable. During age-hardening, also known as precipitation hardening strength increases proportional to the precipitate formation until a critical value is reached. After that, the alloy become over aged [52,53]. The 7000 series is made up of Al-Zn-Mg-Cu alloys where zinc is the strengthening component [54]. These alloys are primarily used in the aerospace and automotive industries because of their high strength and heat treatability. In these Al-Zn-Mg-Cu alloys, Zn is used greater than 3% and a Zn to Mg ratio greater than two is used. Precipitates in these alloys start as GP zones which become η´ coherent platelets and transform to η over time [55].

2.4.1 Heat Treatment of Al-Zn-Mg-Cu System

High strength 7xxx aluminum alloys (Al-Zn-Mg-Cu) in the wrought condition undergoes several combinations of heat treatments among annealing, solutionizing, quenching after solutionizing, precipitation hardening at room temperature, high temperature ageing and work hardening. Broadly, the homogenization of the solute elements in the primary Al matrix, dissolution of low melting secondary intermetallic phases, morphological and compositional modification of secondary intermetallic phases, and precipitation reactions for strengthening is typical microstructural modifications occurring during the various procedures of heat treatment in these alloys. In order to design an optimal process, it is vital to understand the origins of microstructural evolution appearing in the final product [53].

Typically, heat treatment of these alloys has several steps, which could be carried out in any preferred order to suite the end product requirement. Figure 2.4 presents a

schematic of the temperature ranges for the various typical heat treatment processes in an alloy from Al-Zn-Mg-Cu family [53].
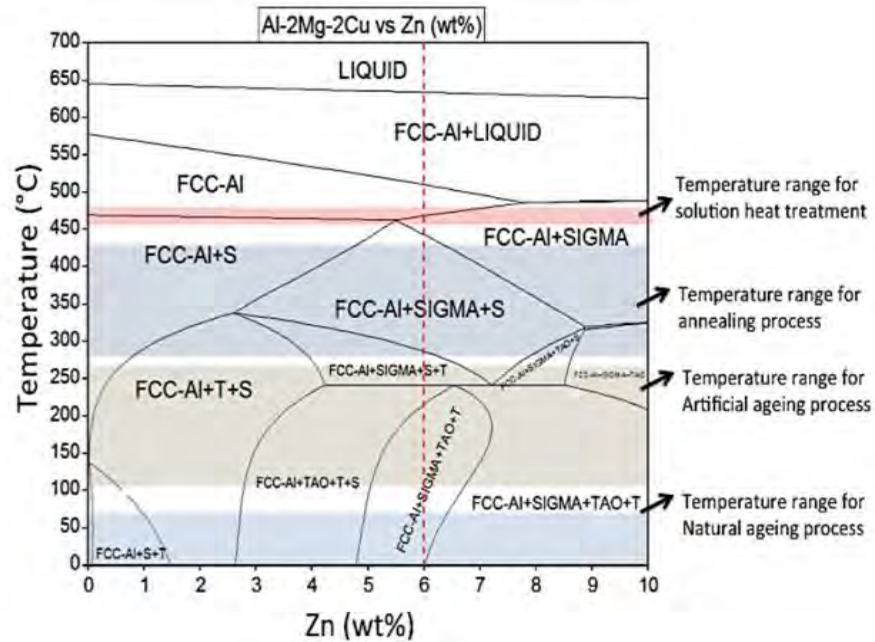
Figure 2.4 Simulated equilibrium phase diagram of the Al-Zn-Mg-Cu system showing Al-Mg-Cu alloy with varying composition of Zn in the alloy.

2.4.2 Solutionizing of Al-Zn-Mg-Cu Alloy

The solutionizing heat treatment of the Al 7xxx alloys at nominal temperatures are basically designed to dissolve the elemental micro-segregation in the primary Al phase of the as-cast microstructure. Several solute elements such as Zn, Mg, Cu, Si, Ni, and B completely dissolve and homogenize in the Al matrix due to their high diffusivity, whereas, there are certain heavier transition elements such as Fe and Cr which are quite sluggish in dissolving and could remain segregated in the matrix even after prolonged times of solutionizing processes at higher temperatures [54]. Table 2.3 presents diffusivity values of all elements participating in the Al-7xxx alloying system [54].

Table 2.3 Diffusion coefficient of common alloying elements in aluminium.

$$D = D_0 \exp(-Q/RT) \text{ cm}^2/\text{s}$$

Element	D_0, cm^2/s	Q, kcal/g atom
Ag	0·21–43	25–39
Cr	3×10^{-7}	15
Cu	0·084–0·29	30–35
Fe	$4·1 \times 10^{-9}$	14–38
Mg	0·12–1·05	28–38
Mn	0·22	29
Si	0·9	30–38
Zn	10^{-2}–1·1	20–46

The solutionizing treatment must be carried out at a safe temperature below the maximum solute solubility temperature of the alloying elements in Al to avoid undesirable consequences such as over-heating causing incipient melting [53]; alloys such as Al 7050 and Al 7075 exhibit significant incipient melting at temperatures much lower than their equilibrium solidus temperature because of evolution of non-equilibrium phases during solidification. Both the Al 7050 and Al 7075 alloys have two soluble phases that are referred to as Sigma (or M) {Mg (Zn, Al, Cu)$_2$} and S (Al$_2$CuMg). The latter is very slow to dissolve and thus rapid heating can produce local concentrations of Al$_2$CuMg. This concentrate Al$_2$CuMg may lead to a non-equilibrium melting point between 485 and 490°C. Figure 2.5 presents this incipient melting appearing on the thermal signature from a Differential Thermal Analysis (DTA) experiment on AA7075 alloy [53].
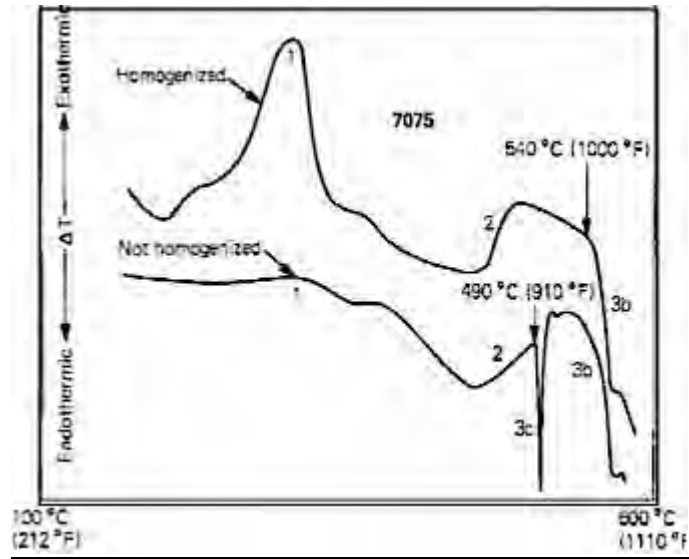
Figure 2.5 Typical thermal data from a DTA experiment of Al 7075 alloy carried out at a heating rate of 20° C/min. The arrows indicate the start of a melting process. Significant inflections on the cu.

In order to better understand the precipitation reactions that are more likely to occur on the subsequent heat treatment processes carried out after the solutionizing (T4), it is useful to first know how the equilibrium fraction of precipitation phases changes as a function of temperature, as shown in Figure 2.6 Robson [56] in his studies based on the thermodynamically calculated volume fractions of phases suggested that the homogenization temperature (~480°C) lies very close to the S-phase solvus so that it is likely that some S-phase constituents will remain undissolved especially in the solute enriched regions. Figure 2.6 presents the changes in the volume fraction (%) of the equilibrium phases during the thermal process of Al 7050, as simulated thermodynamically by Robson [56]. Figure 2.6 shows that the solvus temperature of the S-phase (Al_2CuMg) is almost the same as the preferred solutionizing (homogenization) temperature (H) for the alloy. This strongly suggests that the complete removal of the S-phase is seldom possible during solutionizing treatment.

18
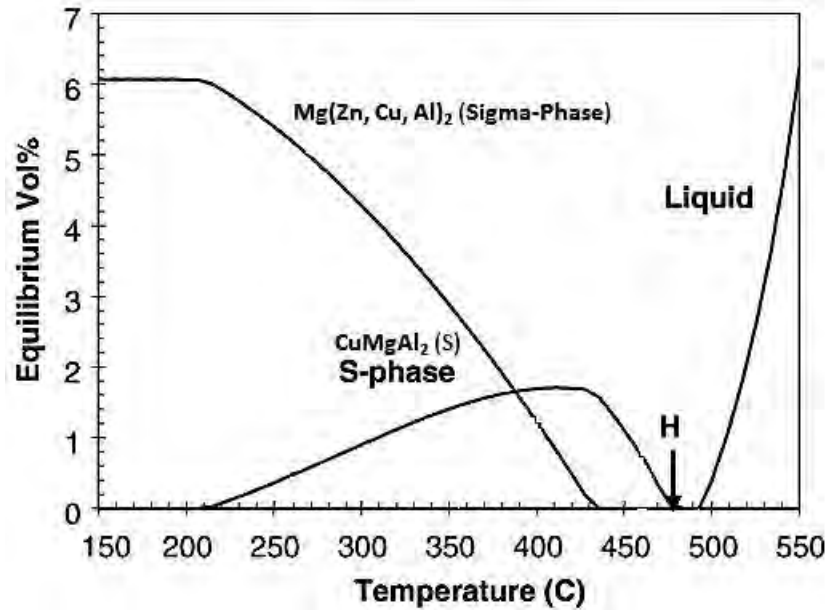
Figure 2.6 Calculated equilibrium phase fraction for Direct Chilled cast 7050 ingots; H corresponds to the solutionizing (homogenization) temperature (753K).

Table 2.4 presents number of vacancies per atom in a pure Al sample at various temperatures. The higher number of vacancies accelerates the kinetics of the precipitation reaction during natural and artificial ageing processes. Besides, the higher solutionizing temperature can provide a better super saturated solid solution (SSSS), which in turn can improve mechanical properties of the alloy part [54].

Table 2.4 Number of vacancies per atom in equilibrium condition in pure aluminum, as a function of temperature.

Temp., °C	Temp., K	Number of vacancies
661	934	$1\cdot6 \times 10^{-3}$
600	873	$4\cdot6 \times 10^{-4}$
400	673	$2\cdot2 \times 10^{-5}$
200	473	$8\cdot3 \times 10^{-9}$
20	293	10^{-12}

Additionally, the amount of quench-in vacancies can directly influence the volume and width size of precipitation-free zones (PFZ), which plays an important role on the corrosive response of the Al-Zn-Mg-Cu material [54].

PFZ are precipitation-free areas around the grain boundaries and sub grains; and they can even form around the precipitates and undissolved phases [55]. PFZ are very important because of their strong effect on the stressed corrosion susceptibility of the

Al-Zn-Mg-Cu alloys [54]. The PFZ was originally contributed to the solute depletion occurring around the grain boundaries due to the formation of precipitation at grain boundaries [57, 58]. Embury et al [46] found that the precipitation free areas around the grain boundaries are supersaturated with solute atom; therefore, he concluded that what makes PFZ's to be free of precipitation is not the depletion of solute but the shortage of enough vacancies required for the nucleation of precipitates. Therefore, quench rate and solutionizing temperature are the most important parameters controlling the size of PFZ areas because they have strong effect on the amount of quenched-in vacancies. This is shown in figure 2.7 by means of TEM micrographs of PFZ areas in the Al-5.9Zn-2.9Mg (wt. %) wherein the effect of different quenching rates on the width of PFZ areas are presented. As it can be seen in 2.7(b), in the samples quenched in oil, not only the PFZ areas are wider but also the precipitates forming within the grain interiors are larger in size; whereas in the water-quenched samples, as in figure 2.7(a), the PFZ areas become narrower and the grain precipitates are far smaller. This is mainly because in the water-quenching condition, the number of entrapped vacancies is larger than that in oil-quenched samples.
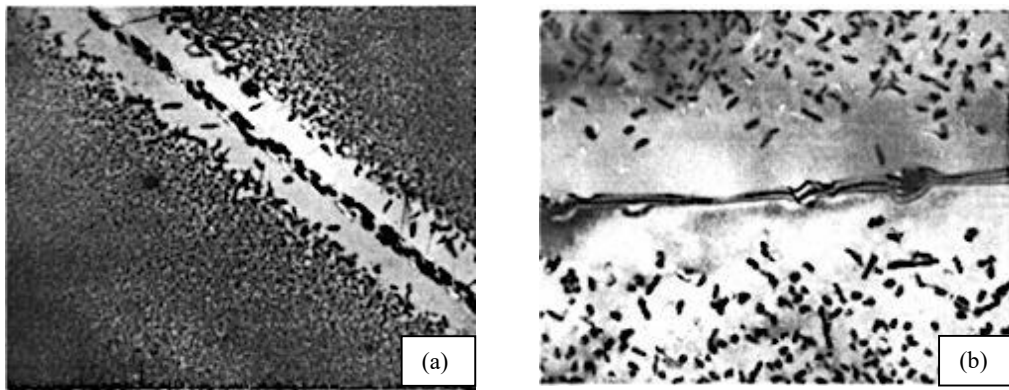
Figure 2.7 Typical precipitate free zones (PFZ) near grain boundaries in Al-5.9Zn-2.9Mg (wt.%) alloy: (a) Water quenched from 465°C and then aged for 12 hours at 180°C, and (b) Oil quenched from 465°C and then aged for 3 hours at 180°C. Magnification of both (a) and (b) is X27000.

2.5 Precipitation Strengthening Mechanisms

Strengthening in an age-hardened Al alloy is based on the interactions between moving dislocations and precipitates [59, 60]. The dislocations can interact with the precipitate itself, as well as the possible strain field associated with the precipitate. The combined effects increase the critical resolved shear stress (CRSS, τ_c), which results in increasing the yield stress of the alloy. The relations between the yield stress σ_y and shear stress

τ_c in polycrystalline materials can be correlated as follows in equation 2.1 using the Taylor factor M, whose value is influenced by crystal structure and orientation texture [59, 61]. For isotropic textures, M is around 3.1 in FCC and 2.75 for BCC metals.

$$\dot{\sigma} = M.\tau_c \qquad\qquad 2.1$$

The retardation of dislocation motion by precipitate particles can simultaneously involve several interaction mechanisms [59]. The mechanisms are divided into two general categories [59] based on the size of the precipitate particles: 1) particle shearing; 2) particle by-passing or Orowan looping. The CRSS increase with particle size is shown in figure 2.8 [59]. Particle shearing also depends on the modulus of the particle relative to the matrix. In aluminum alloys, however, it was shown by Nicholson et al. [62, 63] that dislocations tend to pass through coherent and semi-coherent particles, but not incoherent particles. If the precipitates are small and densely populated, the interparticle spacing is small, and the moving dislocations are most likely to break away from the precipitates by shearing. If the particles are large and more spread out, the dislocations are more likely to bypass the particles by bowing, as proposed by Orowan [64]. Obviously, the optimum strengthening from precipitate particles can be obtained at particle radius of τ_c.
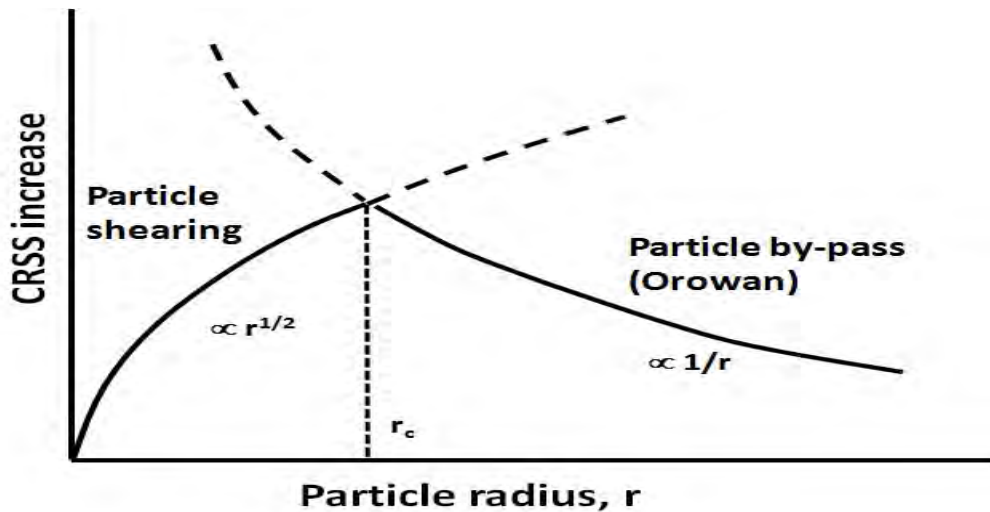
Figure 2.8 Increase in CRSS vs the precipitate particle radius r.

2.5.1 Strengthening through Penetrable Particles

Consider an array of particles is sheared by a moving dislocation, as shown in Figure 2.9 [59], where L is the interparticle spacing, T is the dislocation line tension and ϕ is

21

the dislocation breaking angle. The "resistance" of the particle to the shearing is F. Therefore, for a particle that is sheared at the illustrated condition, F can be expressed by T and ϕ, as shown in Equation 2.2.

$$F=2T\cos\frac{\phi}{2} \qquad\qquad 2.2$$
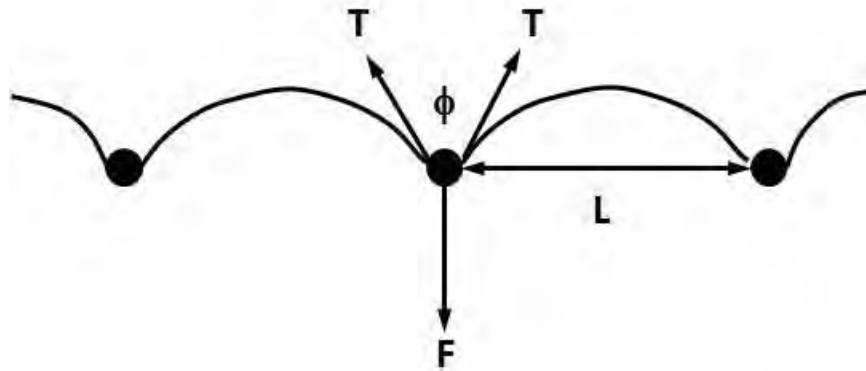
Figure 2.9 Schematic illustration of particle shearing by a moving dislocation.

There are generally five properties that affect the ease of particle shearing by the moving dislocation [65]: 1) Coherent strain; 2) Ordered structure; 3) Precipitate Modulus; 4) Surface or chemical; 5) Stacking fault energy.

1. Coherent strain strengthening

Coherent strain results from the misfit precipitates that distort the matrix. This causes a stress field in the region surrounding the precipitate. This additional stress can interact with the stress from a moving dislocation, and impede its motion. Therefore the force required to shear the precipitate particle rises and causes shear stress, τ_c to increase [65].

2. Order strengthening

If the precipitate has an ordered structure, the passing of a dislocation may create an anti-phase boundary, a region where the structural order is disrupted. The additional energy resulting from creating the anti-phase boundary will increase the resistance of the particle being sheared, and therefore will lead to an increase in τ_c.

3. Modulus strengthening

Because the energy of a dislocation depends linearly on the local modulus, particles which have a modulus different from the matrix will interact with the dislocation by locally raising or lowering its energy as it moves through [65].

4. Surface or chemical strengthening

When a precipitate particle is sheared, a step of one Burgers vector is created at the particle-matrix interface for every dislocation that passes. If the surface-to-volume ratio of the particle is relatively high, it increases in surface area becomes significant and can lead to a substantial increase in the surface energy.

5. Strengthening through stacking fault energy

If the precipitate has significantly different stacking fault energy than that of the matrix, the interaction between an extended dislocation and a precipitate may be dominated by the local variation in the fault width when the moving dislocation enters and is contained within the precipitate [65].

2.5.2 Strengthening through Particle Bypassing: Orowan Looping

As precipitate particles grow, they become increasingly difficult to shear. As a result, the moving dislocation will first 'bow" around the particles, as shown in Figure 2.10 (a) [59]. As dislocation motion continues, it may bypass the particles by looping and leave a "loop" of dislocations around them, as shown in Figure 2.10 (b) [59]. This mechanism was first proposed by Orowan [59, 64-66] and the change in shear stress, τ_c with the particle radius r, volume fraction f, and shear modulus of the matrix μ_m is shown in Equation 2.3 [59, 64-66].

$$\tau_c = \left(\frac{3}{2\pi}\right)^{\frac{1}{2}} . \frac{\mu_m b}{r} . f^{\frac{1}{2}} \qquad\qquad 2.3$$
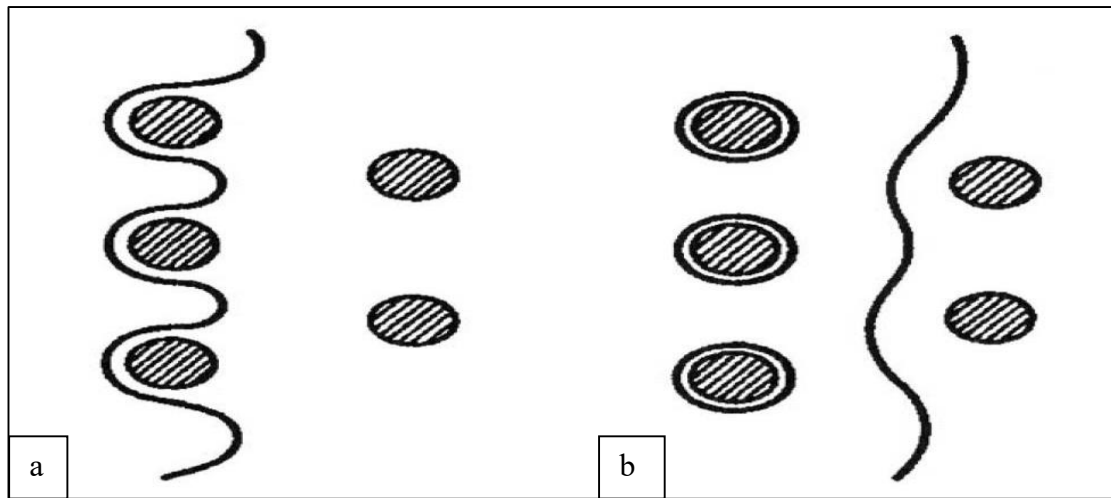
Figure 2.10 Schematic illustration of (a) Dislocation bowing around impenetrable precipitate particles; (b) Continuing motion of dislocation with loops of dislocations left around the particles
.

2.6 Precipitation Age-Hardening of Al-Zn-Mg-Cu Alloys

Precipitation hardening of 7xxx aluminum wrought alloys usually occurs during the non-isothermal condition wherein the precipitates are formed in the high strength Al-7xxx alloys during the cooling process from the solution treatment temperature. These non-isothermal precipitates that are industrially important have been carefully studied [67, 68]. These precipitates can remove solute elements from the supersaturated solid solution matrix to form coarse precipitates which in turn have a detrimental effect on the subsequent age-hardening response of the material [69]. In the complex system of the Al-Zn-Mg-Cu alloys, several precipitation phases could evolve during the heat treatment processes, namely, the η phase ($MgZn_2$), M/Sigma phase $Mg(Zn, Cu, Al)_2$, T phase $\{(Al_2Mg_3Zn_3)$ or $Al_{32}(Mg, Zn)_{49}\}$, S phase (Al_2CuMg), θ phase (Al_2Cu) [70,71].

The hexagonal phases of η or M are mostly observed in the as-cast microstructures whereas the orthorhombic phases of S and T are more common in solid solution states with the extended composition ranges containing all four elements, i.e., Al, Zn, Mg, and Cu [56]. During natural ageing process of the Al-Zn-Mg-Cu alloys occurring immediately after quenching from solution heat treatment temperature, precipitation process starts with the formation of solute clusters from the supersaturated solid

solution (SSSS). These unstable vacancy-rich solute clusters (VRC) are also known as Guinier-Preston (GP) zones. These early stage GP clusters are named after Guinier [72] and Preston [73]. A widely accepted sequence for the precipitation sequence of Al-Zn-Mg-Cu alloys is given in the below sequence which is also schematically is presented in 2.11.

Supper saturated solid solution → VRC or GP zones (type I & II) → Intermediate phases (η') → Stable phases (η or T)
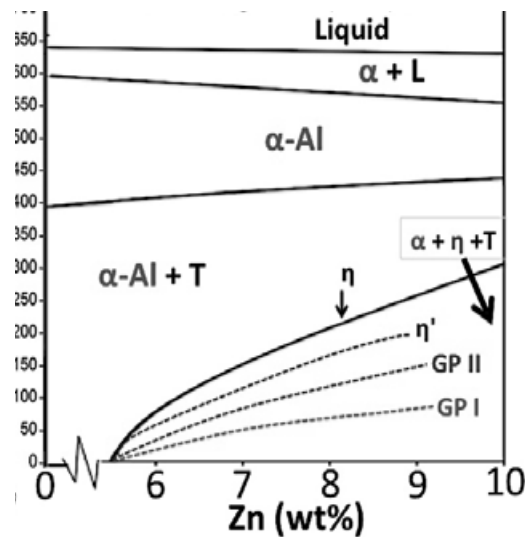
Figure 2.11 The Al-Mg-Zn phase diagram showing the schematic equilibrium solvus temperature lines for the metastable GP zones (GP-I and GP-II), η' and equilibrium η-MgZn$_2$.

Despite all the extensive investigations [70, 74], there still exists some uncertainty about the transient stage from GP zones to the intermediate phases: Evidently, there are two types of GP zones: type I is proposed to be spherical and the type II is observed to be with its internal ordered structure. Figure 2.12 [38], presents schematically the transitional reaction occurring during the ageing process of the Al-7xxx alloys.
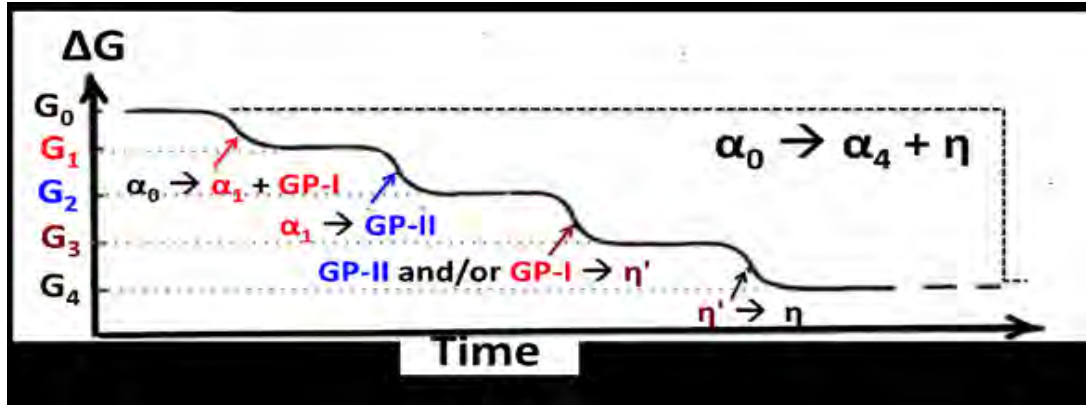
Figure 2.12 Schematic presentation of total free energy as a function of time.

At a temperature slightly higher than the formation temperature range for GP zones (as schematically shown in Figure 2.13), other metastable precipitate (or intermediate η'-phase) is formed either indirectly by nucleating on the GP zones (type I) as the preferred locations for the formation of these η'-phase or directly from larger GP zones (type II) as an ordering and transformation phenomena. Finally, at a relatively higher temperature range, the equilibrium η ($MgZn_2$) phases become stable as a solid state phase transformation or ordering phenomena from the intermediate η' (transient) phases. The precipitation sequence occurs because direct formation of stable η-phases from supersaturated solid solution matrix requires a large driving force to overcome the energy barrier for the nucleation of the equilibrium η ($MgZn_2$) phases.
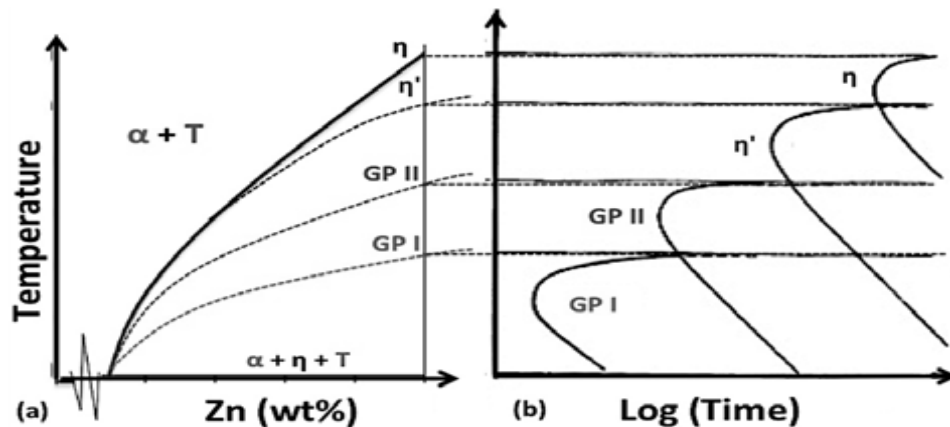
Figure 2.13 The schematic presentation of precipitation sequences in Al-Mg-XZn alloys: (a) The metastable solvus lines in the Al-Mg vs. Zn phase diagram; and (b) Relative time for the start of formation of each precipitation stage at different temperature for alloy with X composition.

Li et al. [75] and Berg et al [74], by means of HRTEM and SAED analyses, re-affirmed the existence of two types of GP-Zones, with distinct structures: GP (I) and GP (II). They found that the GP type (I) zones (solute-rich clusters) are coherent with the Al

matrix; with an internal ordering of Zn and Al/Mg on the {001} Al planes. On the other hand, they found that the GP type (II) zones are zinc-rich layers forming on {111} Al planes and they reported that the formation of the GP (II) depends on the quenching rate and ageing temperatures as they were only discernable in the samples quenched from a temperature above 450 °C and aged at a temperature above 60~70 °C [57,76]. Figure 2.14 presents the SAED patterns of the various zone axes of <001>, <111> and <112> of aluminum matrix.
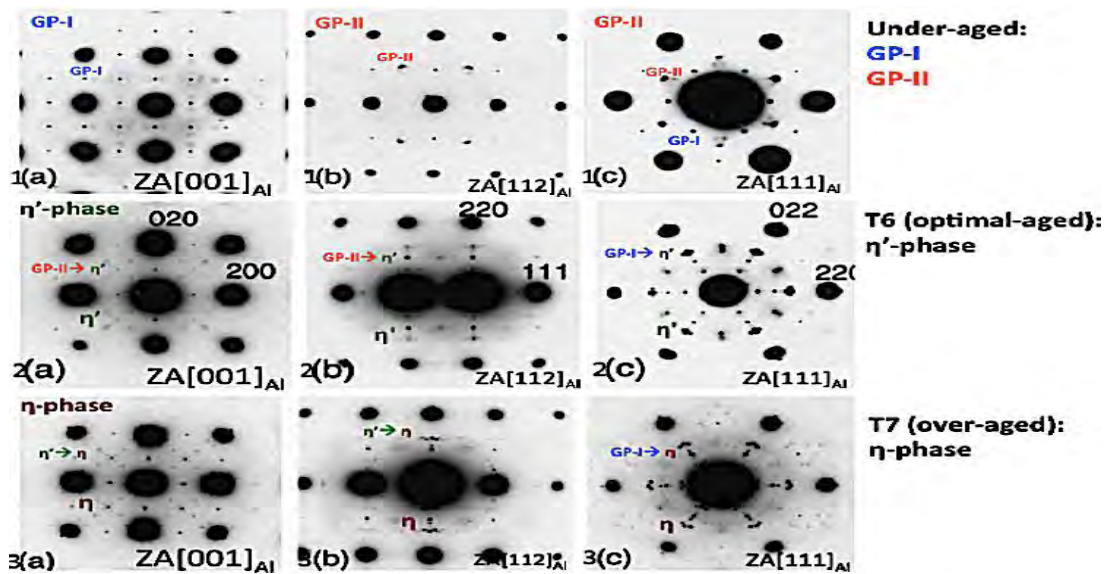
Figure 2.14 Selected area diffraction patterns (SAED) from samples aged to an (1) under-aged, (2) optimal age (T6) and (3) over-age (T7) conditions of Al7050 alloys are shown in (a) the [001] Al-projection, (b) [112] Al-projection, and (c) [111] Al-projection. Precipitate spots are from GP zones, η and η' phases. Sharp extra spots are from simple cubic positions.

Also, Engdahl et al [77], by means of transmission electron microscopy and atom probe field ion microscopy, studied three alloys of Al-Zn-Mg-(Cu) family aged at 150 °C. They found GP (I) zones in the copper sample; whereas in copper free samples, only GP (II) zones were detectable [77, 78].

2.6.1 Rate of Hardening during Ageing Process

The parameters controlling the precipitation hardening or growth rate in the ageing process of Al-Zn-Mg-(Cu) alloys are: (1) ageing time, (2) ageing temperature, and (3) solute element concentration. Ageing time has a direct effect on the size and the number density of the early stage clusters (GP zones), most of which subsequently transform to semi-coherent strengthening η' precipitates. This is presented in figure 2.15 (a) and (b), wherein the experimental data points, of the average size and the number of GP zones of a 7xxx alloy, are plotted against isothermal incubation time during the artificial ageing process at 121°C [77]. Similarly, ageing temperature can affect the GP zone formations during the early stage clustering of the ageing process in the Al-Zn-Mg-Cu alloys. Irrespective of mechanism, at higher ageing temperature, the early stage (GP) clusters transform to the strengthening η' precipitates in a shorter isothermal time [54].
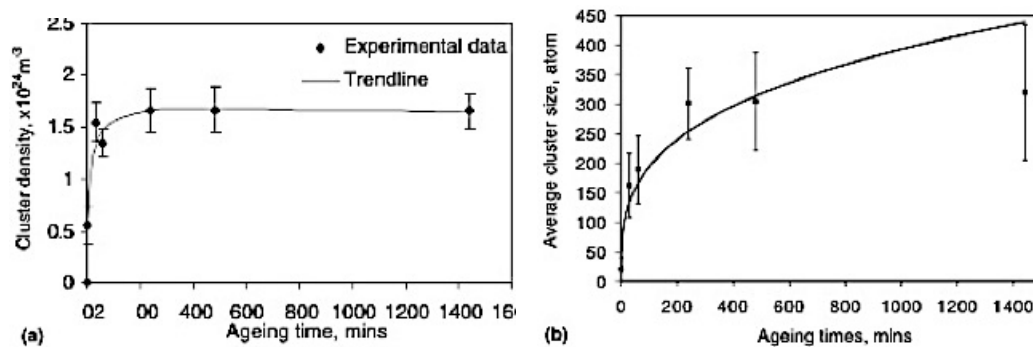
Figure 2.15 Typical experimental data of the number density and the size of the early stage clustering (GP zones), evolving during ageing process at 121 °C of Al 7050 alloy, which were measured by 3DAP for a duration of 1440 minutes time period .

2.7 Hot rolling of Aluminium Alloys

Aluminium alloys contain solute additions such as Zn, Mg, Cu, Cr, Ni. which can markedly affect grain structures within the grains; Figure 2.16. This in turn strongly influences the responses of alloys to working and heat treatment. Both crystal structure and microstructure influence mechanical properties.
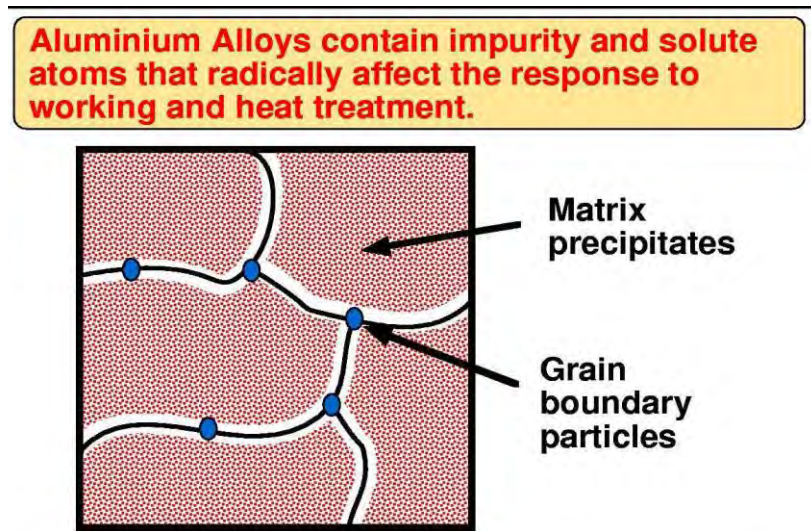
Figure 2.16 Heat treatment and working of aluminium alloys.

In the case of Al 7075 presence of solute phases poses additional challenges in the hot workability of the alloy. However, A. Abolhasan et al. [79] showed that it is possible to obtain good mechanical properties in Al 7075 alloys at a temperature range between 350°C to 450°C. Which is attributed to the dynamic recovery and recrystallization of η phase during the hot rolling.

CHAPTER 3
Experimental Procedure

The principle objective of the work was to process and characterize Al 7075 alloys, Ni added Al 7075 alloys and Ni and B added aluminum 7075 alloys, and with experimental data a proper simulation was to be made. In this context the alloys were cast, heat treated and later hot rolled. Samples were tested for its different properties such as tensile strength, thermal behavior, composition etc. Microstructures were also studied to understand the process behind the property change. A brief description of the experimental works starting from base material selection that were done described in this chapter.

3.1 Starting Materials

Al 7075 alloy contained a large amount of solute elements (nearly 12% in weight), which contributed to its high mechanical performance. The main alloying element was zinc. The second was magnesium, which was predominantly added to increase the wetting between matrix and reinforcement. Other elements that were added in the base alloy were copper, zirconium and chromium. Three different aluminum 7075 alloy castings with three different compositions were made. Each weighted 8 kg in total. So, in total 24 kg of casting were done.

To add alloying elements in Al 7075 master alloys and pure alloys were used. Zinc, Magnesium, copper was added in pure form. Aluminum was added both in pure form and in the form of master alloys with other alloying elements. The Master alloys that were used are given below:

- Al-Ni 20% master alloy.

- Al-Zr 10% master alloy.

- Al-Cr 5% master alloy.

- Al-B 8% master alloy.

The alloy compositions used in three different alloys are tabulated in table 3.1, 3.2 and in 3.3.

Table 3.1 Base aluminium 7075 alloy.

Elements	Percentage (%)	Grams for 8 Kg casting(gram)
Zinc	6.0	480
Magnesium	3.0	480
Copper	2.0	160
Chromium	0.3	24
Zirconium	0.02	16
Aluminum	Balance	Balance

Table 3.2 Aluminum 7075 alloy with nickel addition.

Elements	Percentage (%)	Grams for 8 Kg casting(gram)
Zinc	6.0	480
Magnesium	3.0	480
Copper	2.0	160
Chromium	0.3	24
Zirconium	0.02	16
Nickel	1.0	80
Aluminum	Balance	Balance

Table 3.3 Aluminum 7075 alloy with nickel and boron addition.

Elements	Percentage (%)	Grams for 8 Kg casting(gram)
Zinc	6.0	480
Magnesium	3.0	480
Copper	2.0	160
Chromium	0.3	24
Zirconium	0.02	16
Nickel	1.0	80
Boron	0.008	0.64
Aluminium	Balance	Balance

For the ease of presenting data these three alloys were named simply as follows:

➢ Aluminium 7075: Alloy 1.

➢ Ni added Aluminium 7075: Alloy 2.

➢ Ni and B added Aluminium 7075: Alloy 3.

3.2 Sample Preparation

At first the master alloys were taken and then they were cut with hand driven and automated hacksaws according to the metals. The amount of metals that were cut was in accordance with the calculation presented in table 3.1 to 3.3.

Then those metals were melted in a pit furnace. Commercially pure aluminum was melted first and when the temperature reached 850°C, chromium and zirconium and nickel alloys were added subsequently. After the addition of zirconium, chromium and nickel alloys magnesium, zinc and boron were added. After melting was done the melted alloys were allowed to cool down to 800°C. Ammonium chloride was also added as degasser. Then the furnace was allowed to cool down a bit until the temperature reached 700°C. Then, melted liquid were poured in rectangular permanent metal mold measuring $30 \times 40 \times 80$ mm^3. The temperature of the mold was maintained at 150°C. After the castings were prepared, section of the samples was cut from the casting for performing the experiments.

Figure 3.1 Molten alloy in the crucible.

3.3 Heat Treatment

Heat treatment was done according to the T6 heat treatment specification. Three different alloys were at first solution treated at 480˚C for 5 hours. Those samples were quenched in water and later they were kept at 450˚C for four hours before applying hot rolling to facilitate recovery and recrystallization. After the reduction of about 66 per cent in height the samples were quenched in cold water.
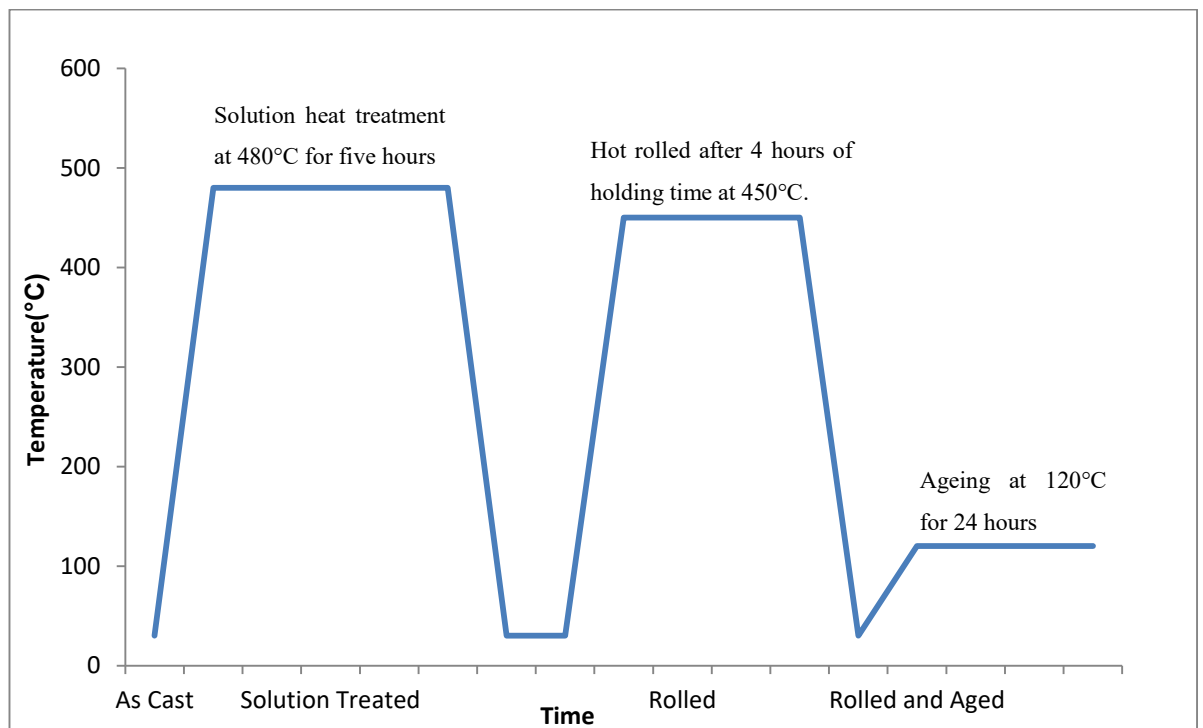
Figure 3.2 Heat Treatment cycle.

The specimen was aged at 120˚C for 24 hours to impart some precipitation strengthening. Heat treatment cycle is shown in the figure 3.2.

3.4 Characterization of Mechanical Properties

To characterize the three Al 7075 alloys several tests were carried out such as hardness and tensile test.

3.4.1 Hardness

Hardness has been used to measure the local mechanical properties of the material in a non-destructive way. It gives a good approximation of the mechanical response of the material, as hardness and yield stress are approximately linearly related [80]. The hardness was taken in HRB mode with minor load 98 N and dwell time was 30 seconds.

3.4.2 Tensile Test

Tensile tests have been performed to measure more accurately the mechanical properties of a wide range of materials. Tensile tests are frequently performed to obtain yield stress, ultimate tensile stress, elongation at fracture as well as the strain hardening behavior. Cross head speed was 0.25 mm/minute. Sample Dimension were tried to keep as close as the dimensions specified in the table 3.4.

Table 3.4 Prescribed dimensions for each sample.

Gauge length	Width	Thickness	Fillet radius	Overall length	Reduced section length	Length of grip section	Width of reduced section
25mm	15mm	4mm	6mm	80mm	32mm	22.5mm	7.5mm

After the tensile specimens were fractured the resultant data were in the form load-elongation. Then those data were converted to true stress- true strain by using the equations described in the following sections. The nominal measures of stress and strain, denoted in this module as σ_{nom} and ε_{nom} respectively, are determined from the measured the load and deflection using the original specimen cross-sectional area, A_0 and length, L_0 as

Engineering Stress,

$$\sigma_e = \frac{P}{A_0}$$

(3.1)

Engineering Strain,

$$\delta = \frac{d}{L_0} \tag{3.2}$$

Where, P and d are electronic reading of the load and the displacement respectively

True stress

$$\sigma_{true} = \sigma_e(1 + \delta) \tag{3.3}$$

And logarithmic plastic strain

$$\in^{plastic} = \ln(1 + \delta) - \frac{\sigma_{true}}{E} \tag{3.4}$$

Where, E is the Young's modulus

With the true stress and true strain data graphs were plotted to find various properties such as yield strength, tensile strength, ductility etc.

3.5 Characterization of Physical Properties

For the Purpose of simulation and to understand the nature of precipitates it was necessary to perform several tests such as DSC, calculation of density etc.

3.5.1 Differential Scanning Calorimetry (DSC)

Differential scanning calorimetry has been used in two ways:

• To identify the nature of the precipitate phases formed during different heat treatments and to reveal some information about their relative volume fractions.

• To study dissolution and precipitation kinetics.

The samples were less than 20 mg. The temperature range for range for DSC was from room temperature to 600°C with the heating rate 10°C/minute.

3.5.2 Density

The densities were calculated by the water displacement methods in 100 ml graduated cylinder. Water displacement method for measuring density is actually quite straightforward. When an object is submerged in water, it pushes water out of the way. If one measures the amount the water level increases, one can find the volume of the water pushed out of the way which equals the volume of the object placed in the water.

3.6 Microstructures

3.6.1 Optical Microscopy

The microstructures were examined to reveal primary α-Al grains, intermetallic particles and eutectic phases. Presence and identification of these phases allowed us to understand the mechanism behind the difference in strength and hardness, effect of the heat treatment on the alloy etc. Modified keller's reagent was used for the etching of aluminium 7075 [82].

3.6.2 SEM and EDS

The objective of doing SEM and EDS was to understand the morphologies of the intermetallics and precipitates that were found of the samples.

3.7 XRF

XRF was done on the aluminium alloys to identify the true chemical composition of these alloys. Since, during casting and in other process many impurities might get involved in the structure and thus those impurities might have various effects on the alloy. Also, during casting much of the elements that were added might get vaporized and thus lost. XRF is nearly accurate to evaluate the amount of materials present in the alloy and thus it is possible to have a clear idea about the alloy composition by doing a XRF experiment. The experiment was performed in a sequential wavelength dispersive X-Ray fluorescence spectrometer. Smooth samples with less than 15 mm thickness was used.

3.8 XRD

XRD (X-Ray diffraction) was carried out for the rapid identification of the various phases that may have formed in the rolled and aged Al 7075 alloys in a non-destructive way. Samples were the same ones used in the XRF. Cu-Kα irradiations were used in the XRD experiment and the wavelength was $\lambda = 0.15418nm$. In the results major and minor peaks were obtained in the 2θ form. From the 2θ angles one can easily deduce its lattice spacing d with the help of Bragg's law:

$$n\lambda = 2dsin\theta \tag{3.6}$$

Where, λ, n, d, θ are wavelength, order of the lattice plane, interplanar spacing and the angle of the peak positions respectively.

.

CHAPTER 4
Experimental Results

4.1 Chemical Composition of the Alloys

XRF was conducted to verify the compositions of the cast alloys.

Table 4.1 Element percentage obtained from XRF analysis.

Element	Alloy 1	Alloy 2	Alloy 3
Aluminium	87.51	86.15	86.18
Magnesium	3.110	3.142	3.227
Zinc	5.930	5.990	6.019
Copper	1.820	1.901	1.863
Chromium	0.204	0.193	0.203
Zirconium	0.035	0.030	0.033
Nickel	0.014	1.059	1.079
Calcium	0.060	0.099	0.022
Silicon	0.373	0.587	0.218
Iron	0.145	0.142	0.155

From the XRF analysis presented in table 4.1 it is evident that there were some impurities in the alloy like silicon, iron, and calcium etc. These impurities might found its way into the alloy during casting. It is very common that some impurities like SiO_2 get into the casting. Elements like zinc, magnesium, copper, zirconium, chromium were found nearly as same as it were added in the alloy. As boron was added in trace elements it was not found in the XRF analysis.

4.2 Hardness

The average hardness values obtained in the experiment are presented in the table 4.2.

Table 4.2 Hardness of the samples (HRB).

Alloy	As cast	Solution treated	Rolled	Rolled and Aged
Alloy 1	64.0	39.67	46.0	76.67
Alloy 2	61.4	47.30	47.5	83.50
Alloy 3	55.0	46.37	57.0	86.47

From the table 4.2 a graph is plotted to present the data in figure 4.1 showing standard deviation.
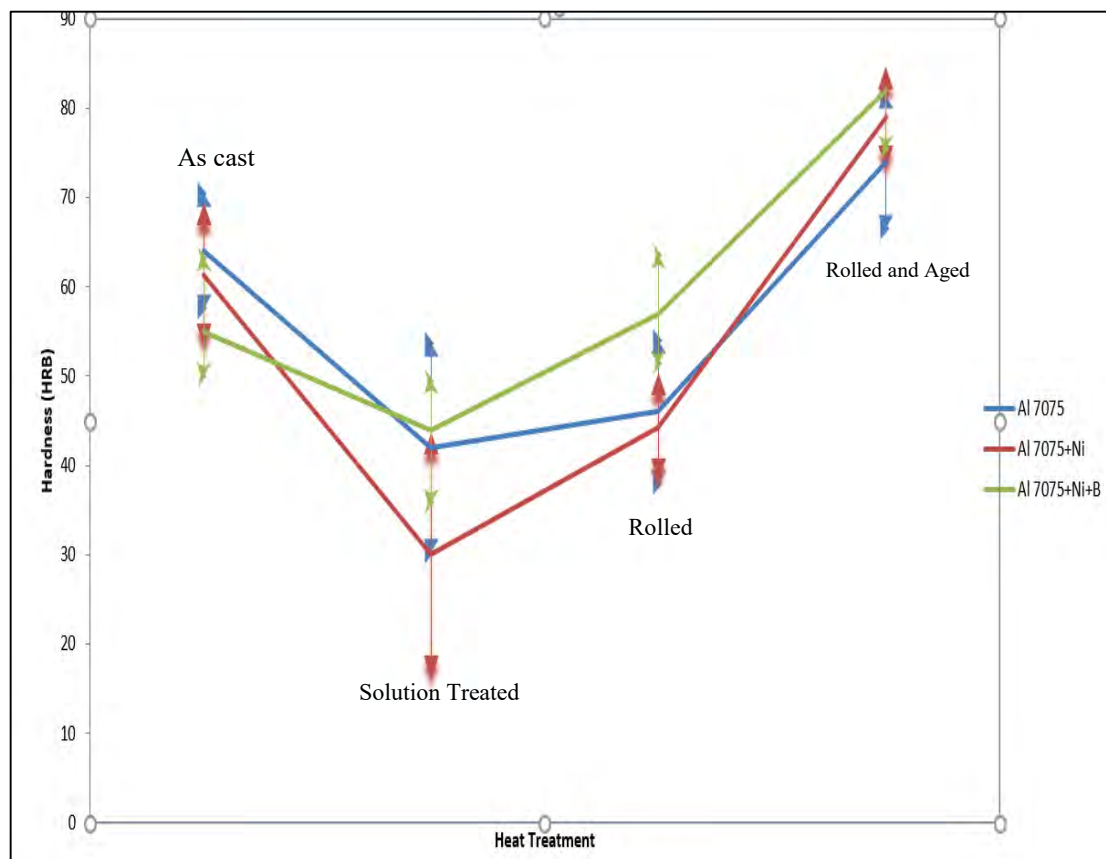
Figure 4.1 Hardness values of three alloys and vertical arrows represents standard deviation of the average hardness .

In figure 4.1 it is observed that as-cast (gradually cooled) sample had high hardness while solution treated samples had the lowest hardness. Hardness was increased a bit with the rolled samples and the highest hardness value was obtained in the rolled and aged samples. The low hardness value obtained in the solution treated samples was mainly due to the dissolution of various precipitates in the super saturated solid solutions (SSSS) that were already there after casting. Precipitates is the main strengthening mechanism in the Al 7075 alloys so, although some solid solution strengthening may had happened due to the dissolution of the precipitates, it could not offset the hardness decrease due to the dissolution of the precipitates [40]. The highest hardness values developed by age hardening samples can be attributed to precipitation of coherent and finely dispersed semi coherent precipitates that are discussed in the section 2.4 to 2.7. The precipitate particles act as obstacles to dislocation movement and thereby strengthen the heat-treated alloys. Also, samples became harder during hot rolling because hot rolling facilitated creation and substitution of these precipitates in the process of dynamic recrystallization. Thus, aged and rolled samples had the highest hardness among all the samples. Another observation from the data was that the Ni and B added aluminium 7075 had retained highest hardness among all the sample in rolled and aged conditions. This high hardness can be attributed to harder intermetallics and their even distribution, and also due to the finely dispersed η' precipitates. Harder intermetallics as discussed in section 2.4 to 2.7 increased hardness by the process called Orowan looping where change in shear stress, τ_c with the particle radius r, volume fraction f, and shear modulus of the matrix μ_m is shown in Equation 4.1 [59, 64-66].

$$\tau_c = \left(\frac{3}{2\pi}\right)^{\frac{1}{2}} . \frac{\mu_m b}{r} . f^{\frac{1}{2}} \qquad\qquad 4.1$$

4.3 Tensile Strength

In the uniaxial tensile testing mode, three different samples were tested for the purpose of obtaining tensile stress-strain curves. Here, physical properties are given in table 4.3. Every data tabulated here are solution treated, rolled and aged at 120°C for 24 hours. Also, elongation here was calculated in a gauge length of 25 mm. Engineering stress –strain graphs are presented in figure 4.3. In table 4.3 properties of aluminium 7075 (Alloy 1), Ni added aluminium 7075 (Alloy 2) and Ni and B added aluminium 7075 (alloy 3) are listed. The change in these properties are plotted in figure 4.2.

Table 4.3 UTS, elongation, max true stress, max true strain and ductility.

Properties	Alloy 1	Alloy 2	Alloy 3
Ultimate tensile strength (MPa)	179.49	193.65	205.06
%Elongation (Gauge length 25 mm)	5.36	6.40	6.24
Maximum true stress (MPa)	929.46	1403.6	1466
Maximum true strain	1.85	2.002	1.99
Toughness (Nm^{-2})	385.9	619.68	639.79

From figure 4.3 it was apparent that the alloy addition had enhanced the mechanical properties of original aluminium 7075 alloy. Elongation was increased up to 6.4% (alloy 2) from 5.36% (alloy 1) and ultimate tensile strength was increased up to 205.06 MPa (alloy 3) from 179.49 MPa (alloy 1). Also, toughness was calculated by calculating the area under the curve using the equation 4.2.

$$Toughness = \int_0^{\varepsilon_f} \sigma d\varepsilon \qquad (4.2)$$

Where, σ is the engineering stress, ε is the strain and ε_f is the strain up to failure

According to equation 4.2 the toughness of alloy 1, alloy 2 and alloy 3 was 385.9 Nm^{-2}, 619.68 Nm^{-2} and 639.79 Nm^{-2} respectively.
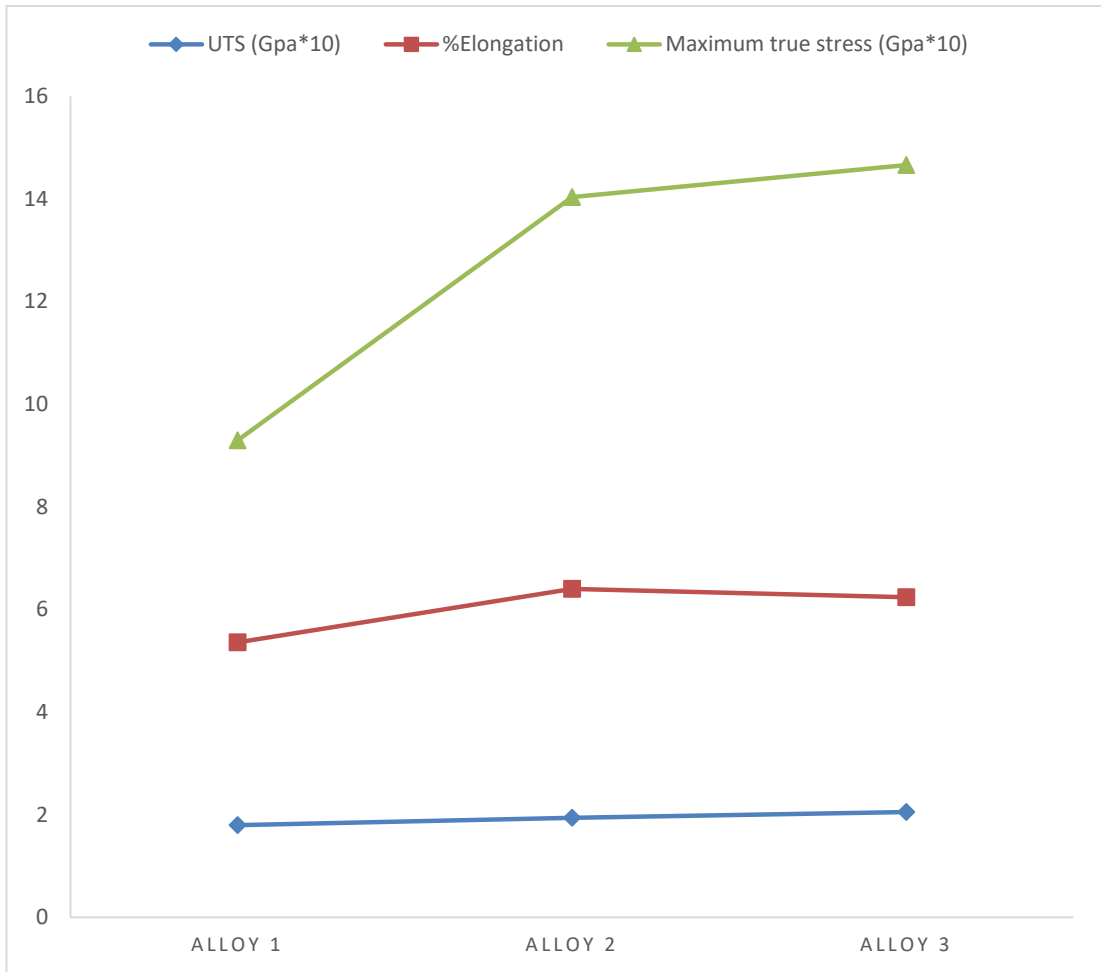
Figure 4.2 Change of mechanical properties in the three different alloys.

(a)

(b)

(c)
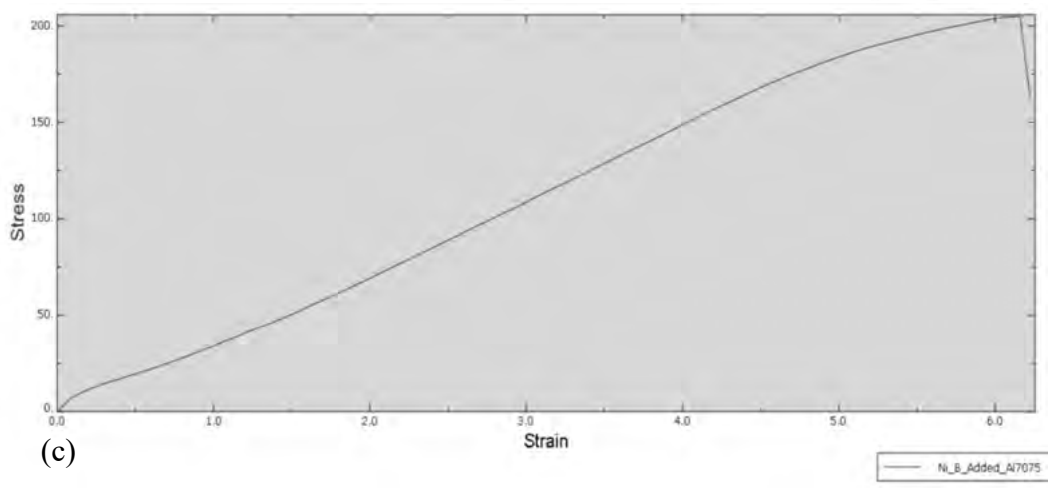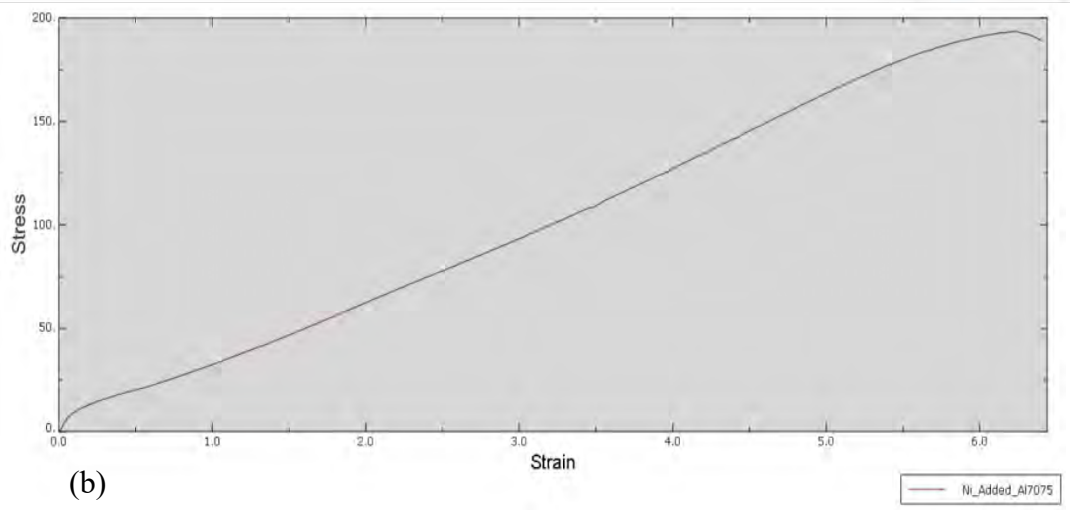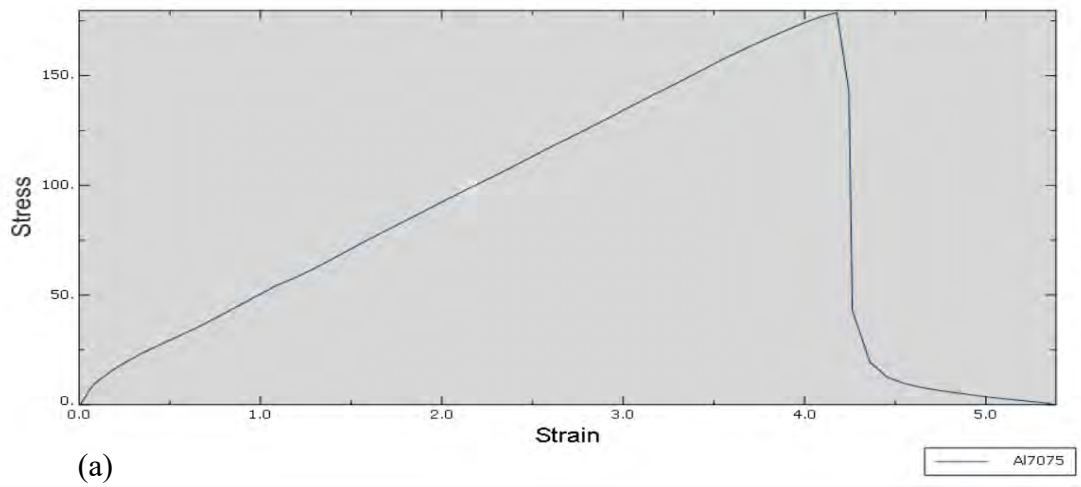
Figure 4.3 Engineering Stress- Strain data plotted. (a) Al 7075 (b) Ni added Al 7075 and (c) Ni and B added Al 7075.

43

4.4 Optical Microscopy

4.4.1 As Cast Structure

As cast structures that were observed are shown in figure 4.4. The differences between the DAS in the three different samples were apparent. Dendrite arm spacing is called the distance between the dendrites secondary arms. To determine the dendrite arm spacing, the total spacing from the first to the last arm needs to be determined, and then DAS will be:

$$DAS = \frac{L}{n*V} \qquad (4.2)$$

Where L, n, and V are length of the first secondary dendrite to last secondary dendrite, number of dendrites and magnification respectively. Several lines were drawn by hand on the printed image and later those results were averaged to calculate DAS.

According to equation 4.2 aluminum 7075 had the average SDAS of 22 μm, Nickel added aluminium 7075 showed 14 μm and nickel and boron added Al 7075 had 6.25 μm. These results showed that the distance between the arms of the dendrites decreased as the alloying element increased. Dendritic solidification frequently occurs under conditions which are far from equilibrium. Given these circumstances, regions of solute-rich liquid can be trapped between the dendrite arms, and solidify eventually to solute-rich solid regions. This in turn led to the development of a "banded" microstructure when the material was subsequently processed by rolling or other mechanical fabrication methods. From figure 4.4 and the DAS calculations it was observed that adding boron made the DAS structure significantly much finer than the other two alloys which also were reflected in the mechanical properties.
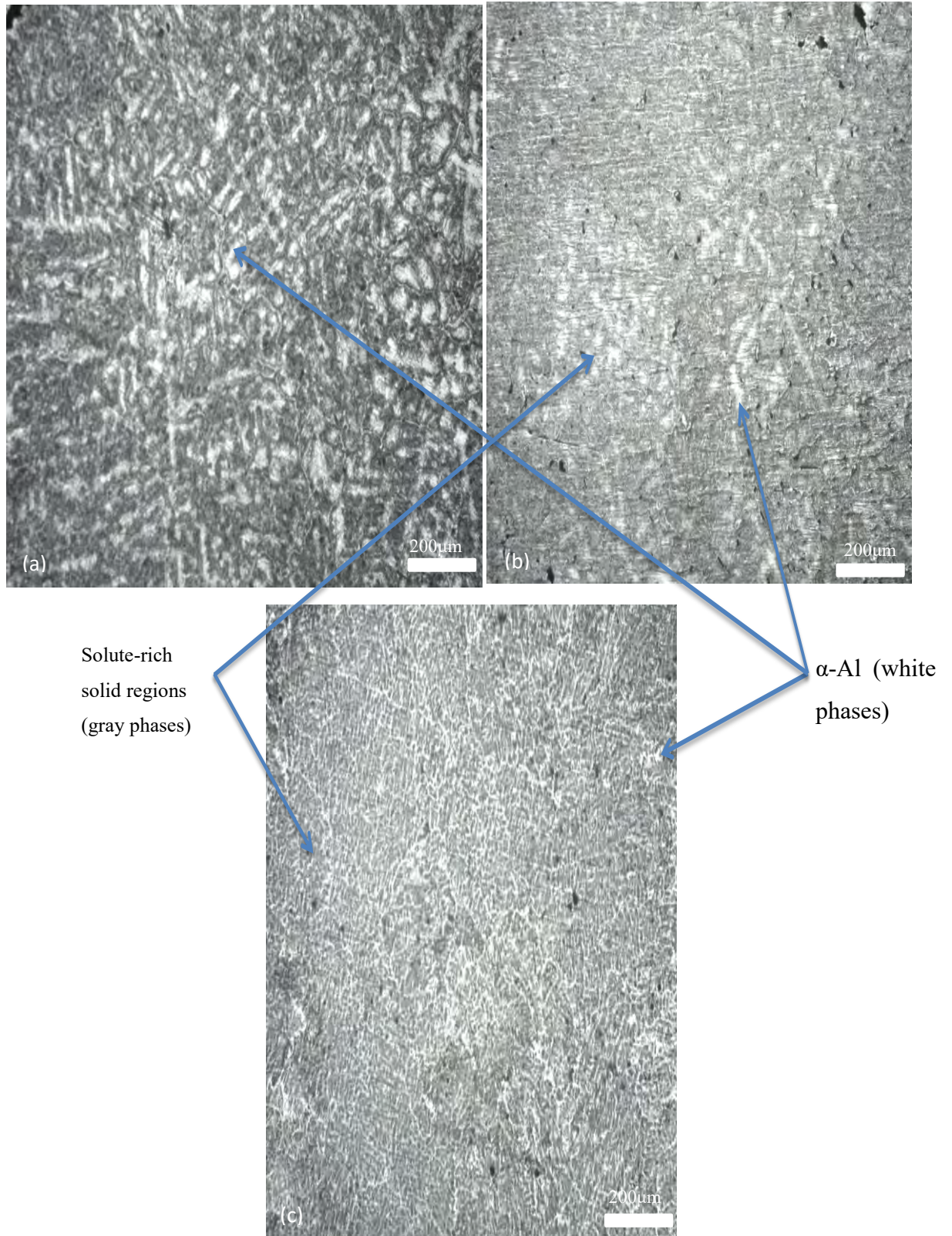
Figure 4.4 Cast Structure of (a) Al 7075 (b) Ni added Al 7075 and (c) Ni and B added Al 7075.

4.4.2 Rolled and Aged Microstructure

The aluminium alloys were solution treated and subsequently hot rolled to impart some recovery and recrystallization. Later precipitation treatment at 120°C for 24 hours was carried out on these samples. Figure 4.5 showed the microstructures of rolled and aged micrographs taken at 200x magnifications. Here, these microstructures showed elongated grain structure at the rolling direction. These elongated grains make the alloys stronger in the rolling direction [83]. A lot of intermetallics were observed in these micrographs (dark phases in figure 4.5). The composition and morphology of these intermetallics were to be characterized in the SEM and EDS segment. However, in figure 4.5 it was observed that the size of the intermetallics became smaller and they were uniformly distributed in Ni and B added Al 7075. Numerous fine porosities were also found in all of these alloys. So, it can be concluded from these optical micrographs that the intermetallics amply formed in all of these alloys which consequently imparted additional strength in these alloys. Addition of Ni apparently did not change much of the grain morphologies of the alloy 2. Addition of B on the other hand, decreased the size of the intermetallics and made them better distributed.
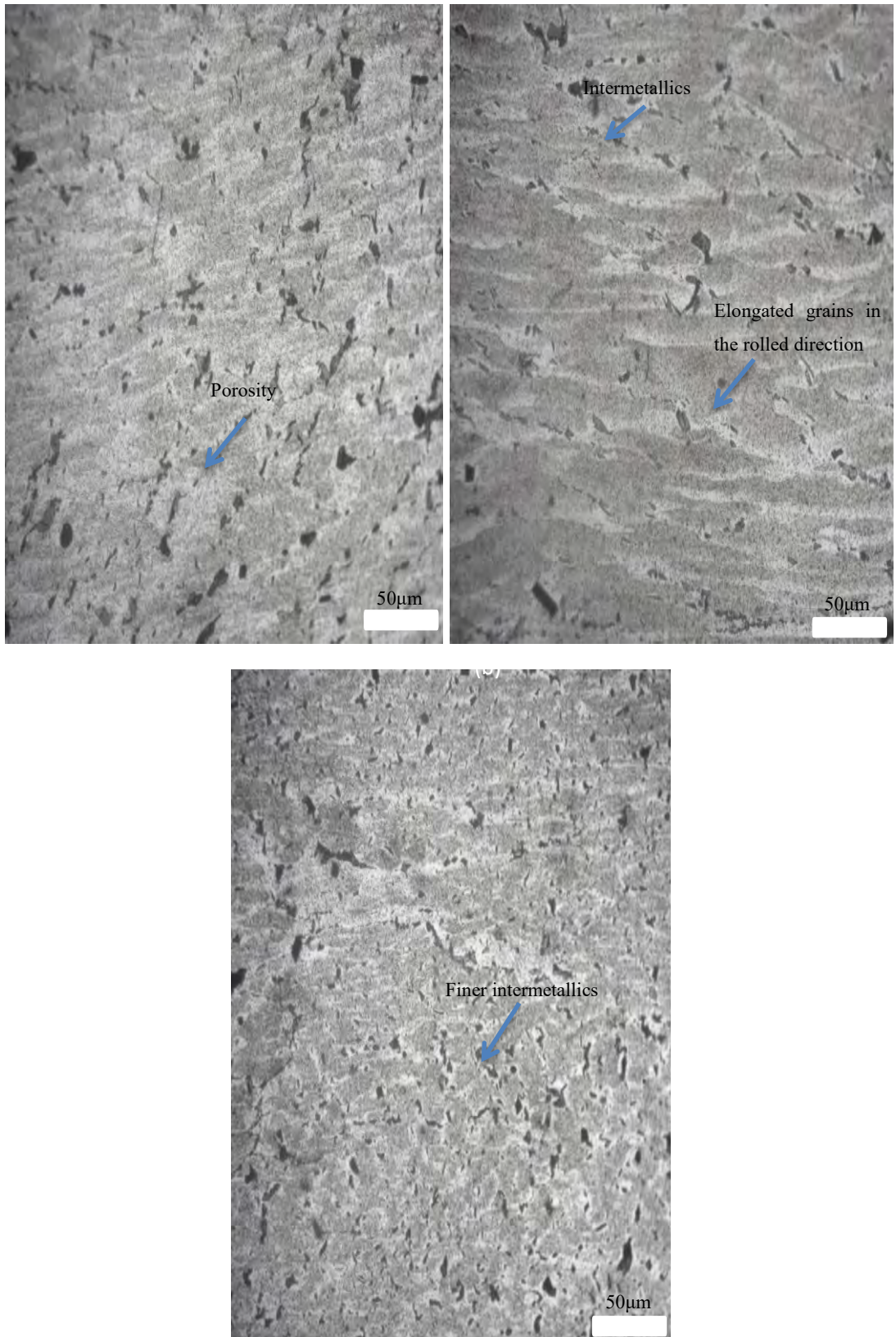
Figure 4.5 Rolled Microstructure (a) Al 7075 (b) Ni added Al 7075 and (c) Ni and B added Al 7075.

4.5 SEM and EDS

It was found in the optical microscopy that there were intermetallics present in the alloy. To understand the morphologies of these intermetallic and possible precipitates SEM and EDS investigation were conducted.

4.5.1 Alloy 1: Al 7075

Figure 4.6(a) is a SEM image of sample 1 in 1000x magnification. In the SEM image it was observed that there were various intermetallics and fine precipitates. To identify the composition of these phases EDS was performed on the sample 1 (point b and c in figure 4.6). In EDS image Figure 4.6 (b) the composition of the fine precipitates taken from point b in figure 4.6 (a) were tried to identify. The mass percentage of the phase was 4% Mg and 11% Zn and the rest were mainly aluminium. The aluminium portion came from the matrix α-Al phase. According to the composition of Mg and Zn obtained in figure 4.6 (b) it is probably either η phase ($MgZn_2$) or T phase ($AlMg_4Zn_{11}$). These types of precipitates are the most commonly observed second phases in the alloy [39]. In the EDS image of figure 4.6 (c) taken from point c in figure 4.6 (a), the composition of the intermetallics was found to be of 74.29% Al, 24.84% Cu and 0.67% Mg. Thus according to the mass percentage obtained in figure 4.6 (c) they were probably Al_2CuMg (S phase) intermetallics which are pretty common in the 7xxx alloys and are essentially ternary alloys of Copper (Cu) [54, 84].
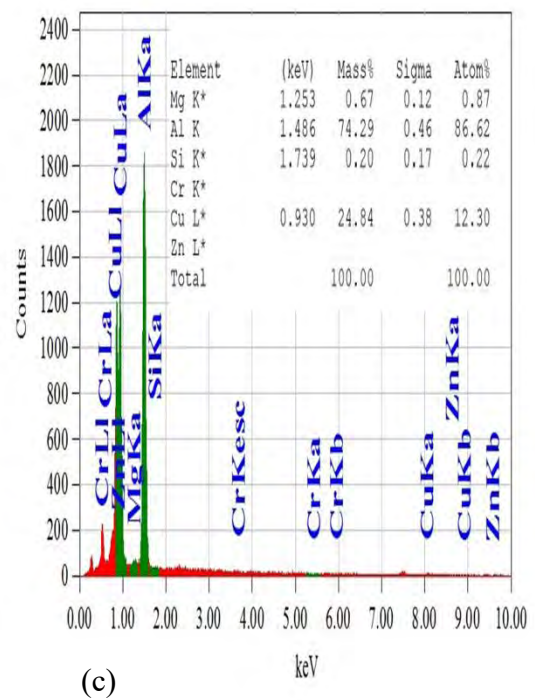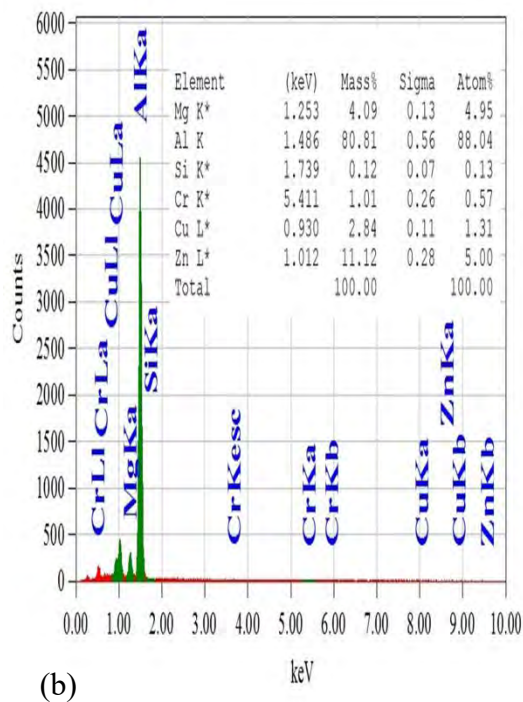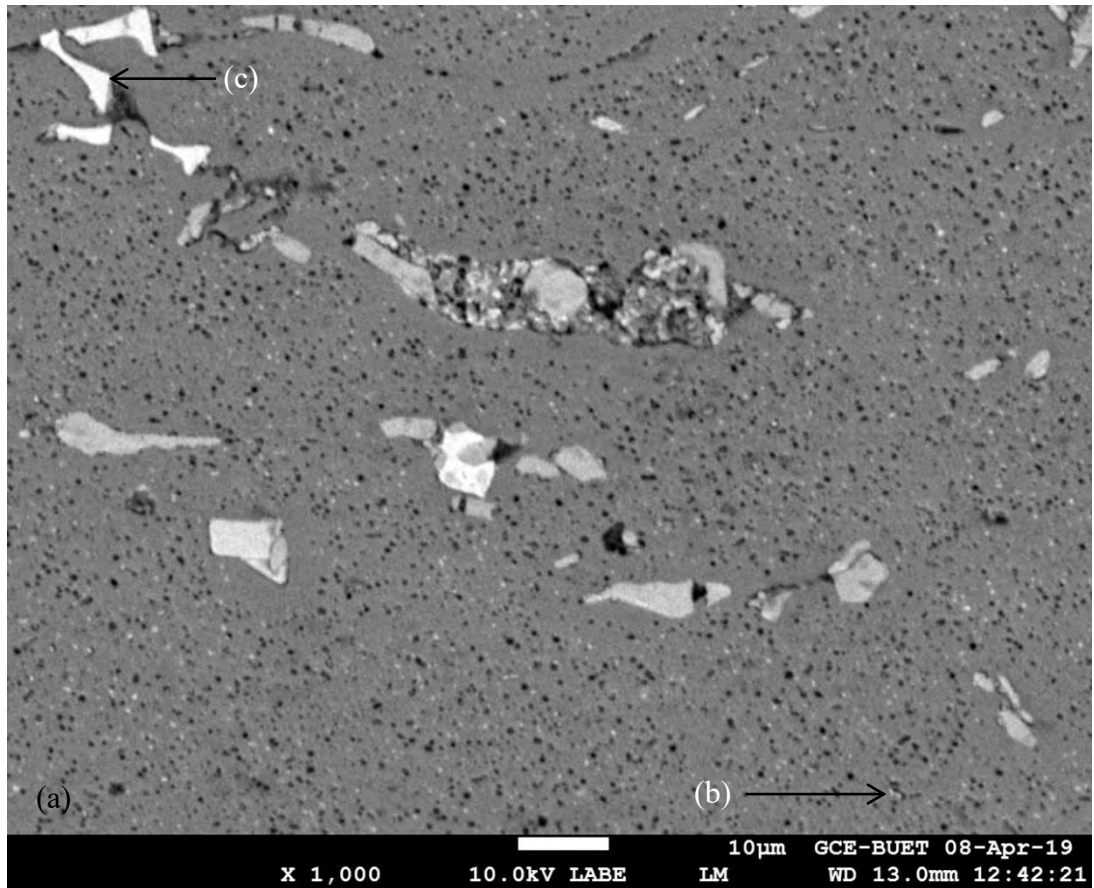
Figure 4.6 (a) SEM image of alloy 1 (b) EDS of the precipitates and (c) EDS of the intermetallics.

4.5.2 Alloy 2: Ni Added Al 7075

SEM image in figure 4.7 (a) was taken on sample 2 at 1000x magnification. In this image precipitates and intermetallics were also found like alloy 1. To understand the composition of these phases EDS investigation was performed.

The EDS image of figure 4.7 (b) was taken from point b in figure 4.7 (a). It was observed that the precipitates in alloy 2 had the similar composition like alloy 1 (1.84% Mg and 4.71% Zn). But investigation on the intermetallics obtained different results. EDS image in figure 4.7 (c) which was taken from point c in figure 4.7 (a) showed that they were Al-Cu-Ni intermetallics having the mass% of Al 37.65%, Cu 15.59% and Ni 46.65%. Al-Cu-Ni Intermetallics with these composition may refer to Al_7Cu_4Ni, Al_4Ni_3, and Al_3Ni_2 [85]. Thus EDS in figure 4.7 (c) indicates that the precipitate composition remained same but the composition of intermetallics changed in alloy 2.
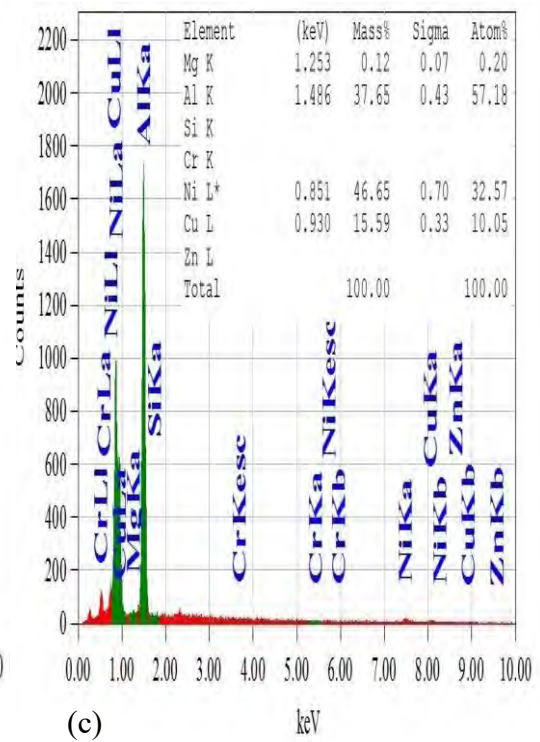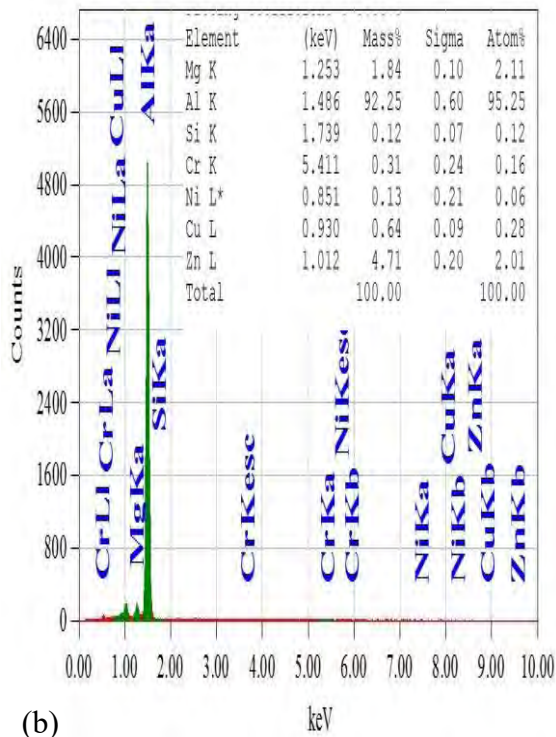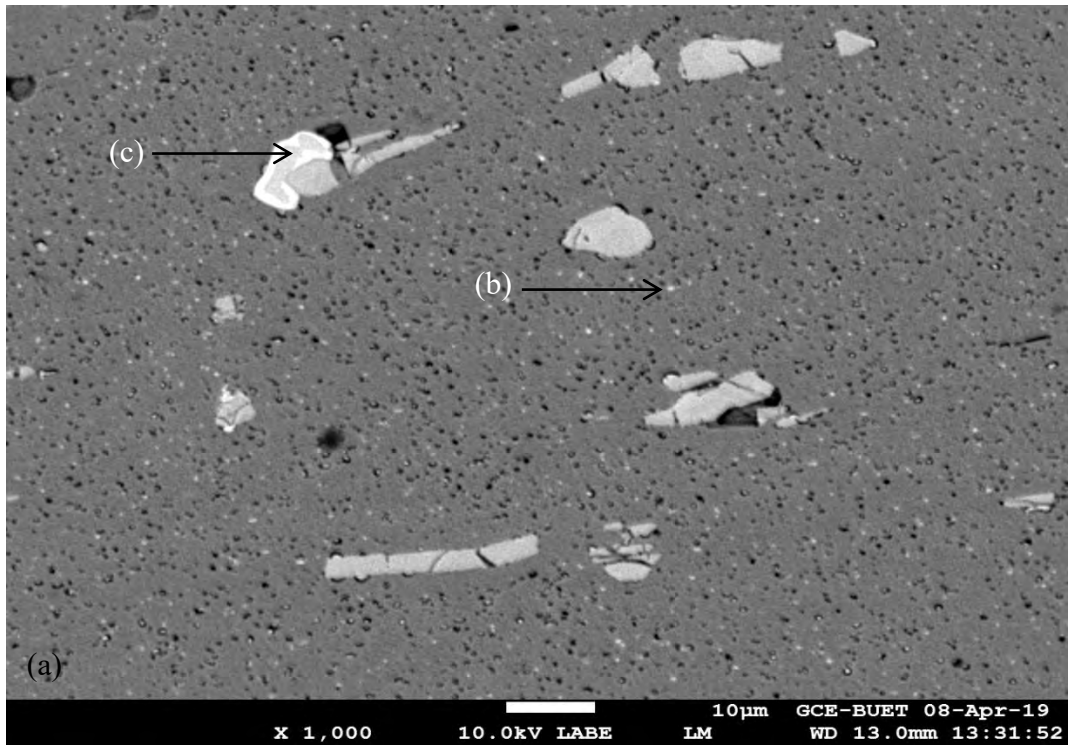
Figure 4.7 (a) SEM image of alloy 2 (b) EDS of the precipitates and (c) EDS of the intermetallics.

51

4.5.3 Alloy 3: Ni and B added Al 7075

From EDS image 4.8 (b) (referred as point b in figure 4.8 a) it was observed that the mass% of precipitates was 1.62% Mg and 5.3% Zn and in figure 4.8 (c) pointed as point c in figure 4.8 (a) the intermetallics mass% was found as 32.91% Al, 19.75% Cu and 47.19% Ni. Thus it can be concluded that the overall composition of intermetallics or precipitates did not change by the addition of B. Nevertheless, if the figure 4.6(a), 4.7(a) and 4.8(a) are compared than it is easily visible that the size of the intermetallics in alloy 3 significantly decreased in alloy 3.
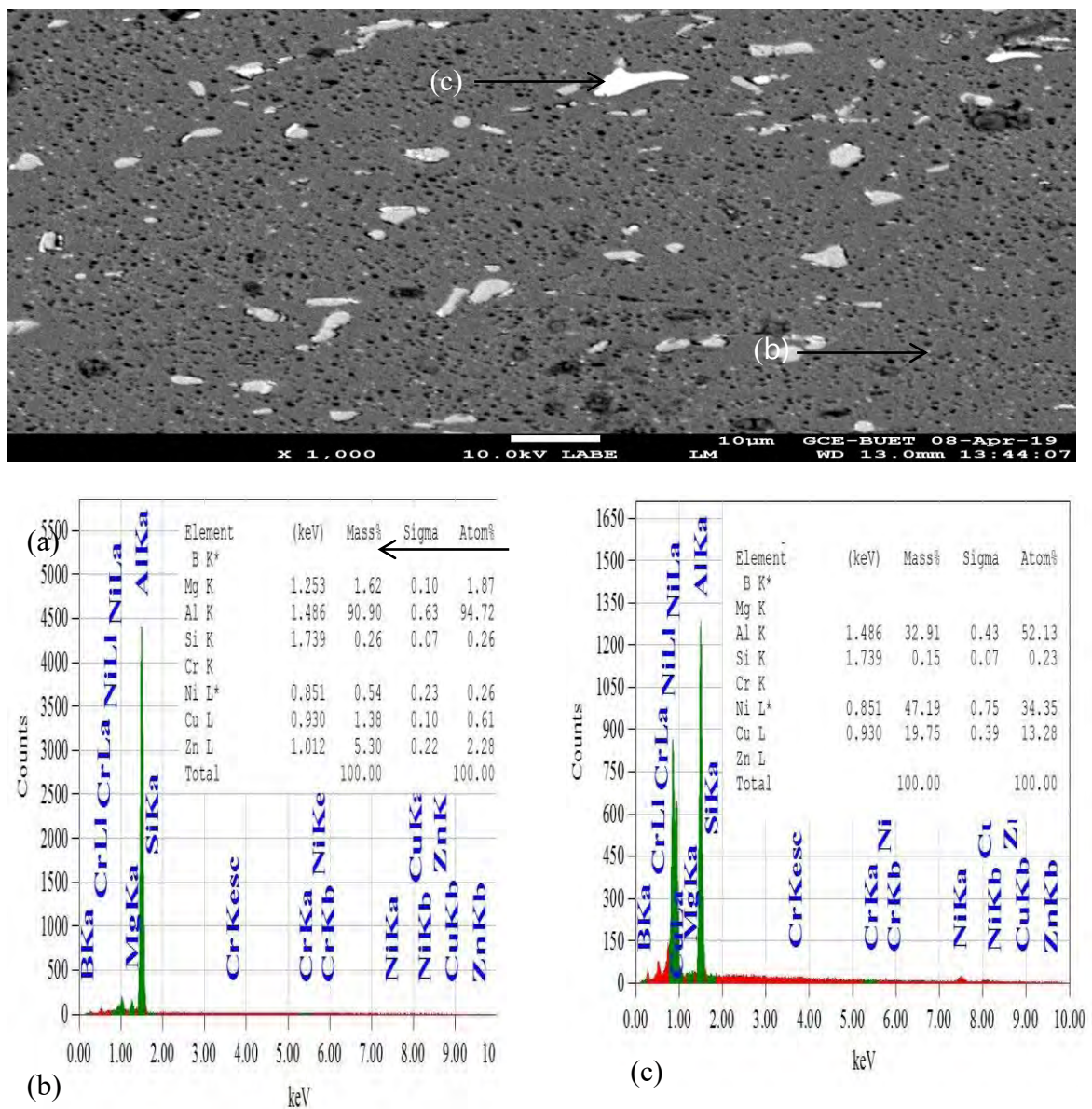
Figure 4.8 (a) SEM image of alloy 3 (b) EDS of the precipitates and (c) EDS of the intermetallics.

To summarize, in all the alloys, precipitates had nearly the same composition. Precipitates in these alloys were identified as either η phase ($MgZn_2$) or T phase ($AlMg_4Zn_{11}$). These precipitates were primarily the reason for the increase in strength in these alloys [54, 57, 77, 78]. The intermetallic composition showed that the intermetallics formed in alloy 1 was probably Al_2CuMg (S phase). These are hard intermetallics and are also known to increase the hardness but detrimental to the strength of the alloy [84]. On the other hand, in alloy 2 and 3 the intermetallics probably had Al-Ni-Cu intermetallics. They mostly substituted the intermetallics found in alloy 1 thus eliminating the detrimental effect of intermetallics in alloy 1 [85]. Also, these intermetallics increased strength by orowan strengthening [59, 64-66]. Addition of B did not change any composition of these alloys but it was also observed that the alloy 3 had much finer intermetallics. And finer intermetallics are known to be far more effective to increase the strength of the alloys [84]. Also, B decreased the distance between the intermetallics and thus by Orowan strengthening mechanism it further increased the strength and toughness of alloy 3 [59, 64-66].

4.6 XRD

XRD results were analyzed by a software called Match 3!. It used search and match method to analyze the raw data to identify the phases from COD (Crystallography Open Database). In figure 4.9 identified phases are showed. Main peaks in figure 4.9 came from α-aluminium (triangles). In figure 4.9(a) There were some minor peaks which corresponded to $MgZn_2$. Although the identification of minor peaks in XRD were not definitive since these phases were present in the alloys at very low percentage (around 1%). And with these low percentage of phases XRD do not obtain definitive results due to the noise from background sources (i.e. scattering by air, elastic scattering by the sample, and scattering by the substrate or sample support) [86, 87]. But these findings do match with the EDS results in section 4.5 so, these XRD minor peaks can also be taken as valid results.

Sample	Major peaks	Minor peaks
Alloy 1	38.3(α- Al 111), 44.45 (α- Al 200), 64.79 (α- Al 220),77.83 (α- Al 311).	41.35 (1122 MgZn₂)
Alloy 2	38.25(α- Al 111), 44.5 (α- Al 200), 64.93 (α- Al 220), 77.76 (α- Al 311)	41.4 (1122 MgZn₂)
Alloy 3	38.31(α- Al 111), 44.5(α- Al 200), 64.79(α- Al 220),77.83 (α- Al 311)	41.54 (1122 MgZn₂)
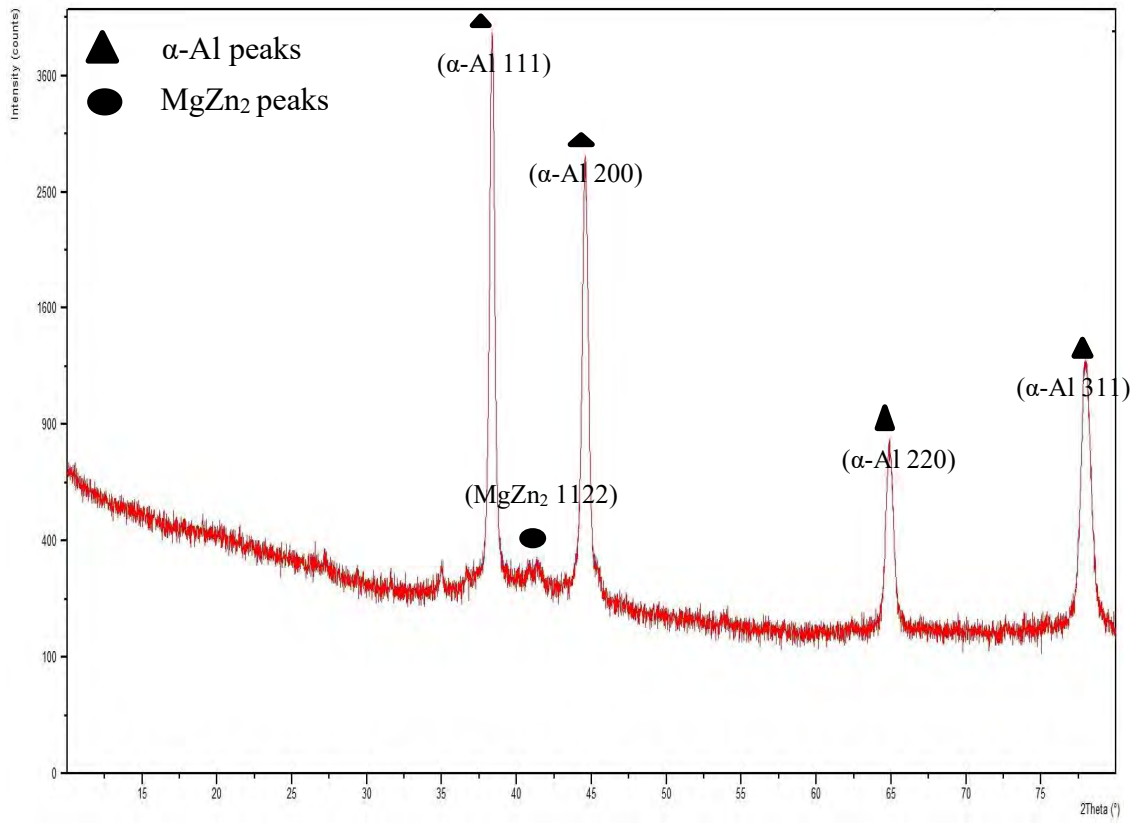
Figure 4.9 XRD of aluminium 7075 showing α aluminium and Mgzn₂ peaks.
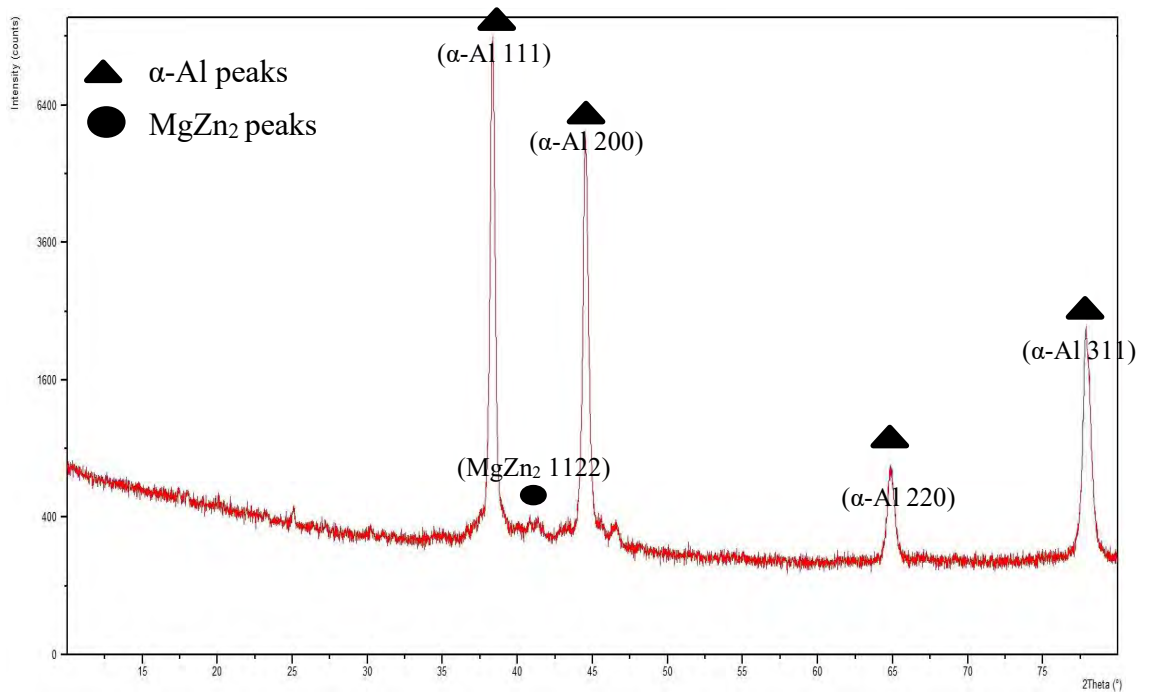
Figure 4.10 XRD of Nickel added aluminium 7075 showing α aluminium and Mgzn₂ peaks.

55
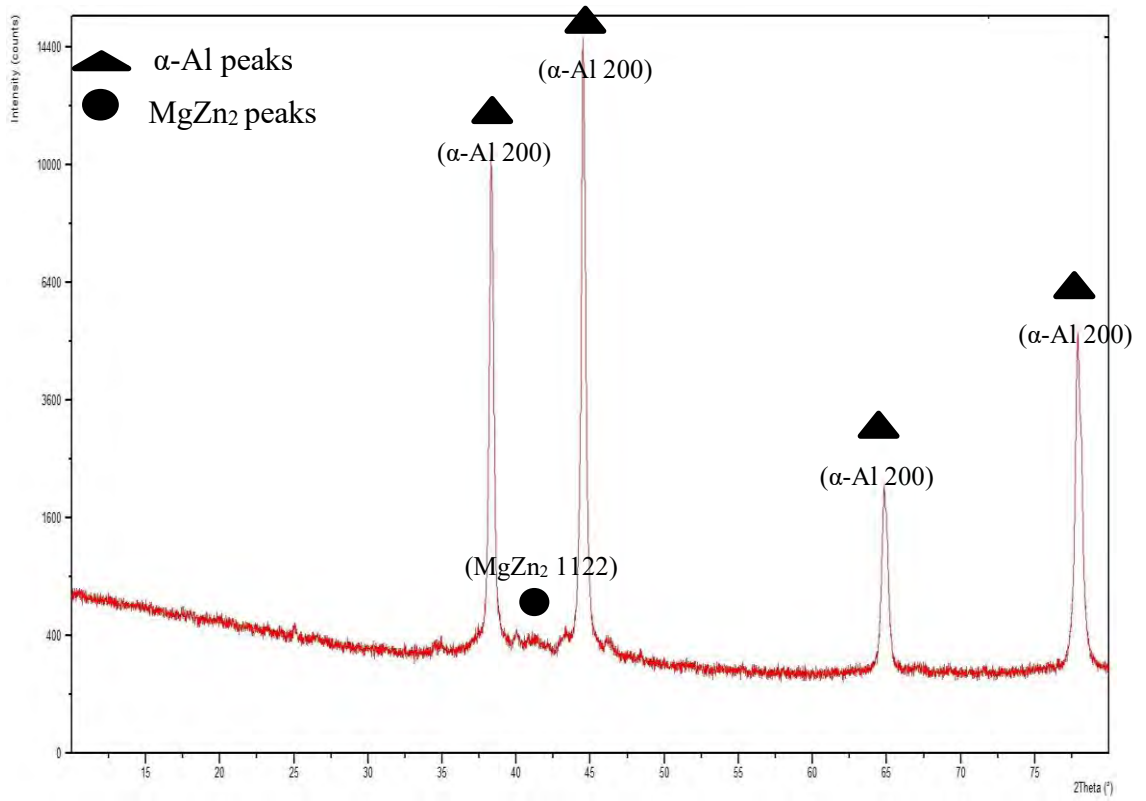
Figure 4.11 XRD of Nickel and Boron added aluminium 7075 showing α aluminium and Mgzn₂ peaks.

4.7 DSC

In the experiment three DSC (digital scanning calorimetry) curves of three different solution treated samples were observed. The temperature range was from room temperature to 600°C. They had some endothermic and exothermic peaks. Consequently, it was observed that the curves could be divided into five or six distinctive categories.

The peaks between 60°C -160°C (a steep endothermic and a broad exothermic peak) were due to the dissolution of GP (guinier-preston) zone and the formation of metastable η' precipitates [90, 91]. Broad exothermic peak is normally selected for hardening this alloy targeting to have the fine precipitates of η' in the alloy to achieve age hardening. Endothermic peaks near 220°C-250°C signify the dissolution of η' and formation of two different types of stable η phases [92]. Until 360 °C the formation of stable η continued. One type of η phase dissolute after that temperature. Another type dissolute at temperature near the point 5 [90, 91]. Finally, the alloy started to melt showing solidus and liquidus double peak portion at point number 6.

In this thesis the precipitation heat treatment was carried at 120°C. In the earlier experiments of SEM and XRD suggested that the three alloys either had stable or metastable $MgZn_2$. Here, in the DSC experiment it is established that the ageing treatment carried out in the experiment produced mostly metastable $MgZn_2$(dashed lines in figure 4.10 between point 1 and 2). Thus, one of the major sources of strengthening of these alloys was due to the precipitation strengthening of metastable $MgZn_2$ that occurred during the precipitation heat treatment at 120°C.
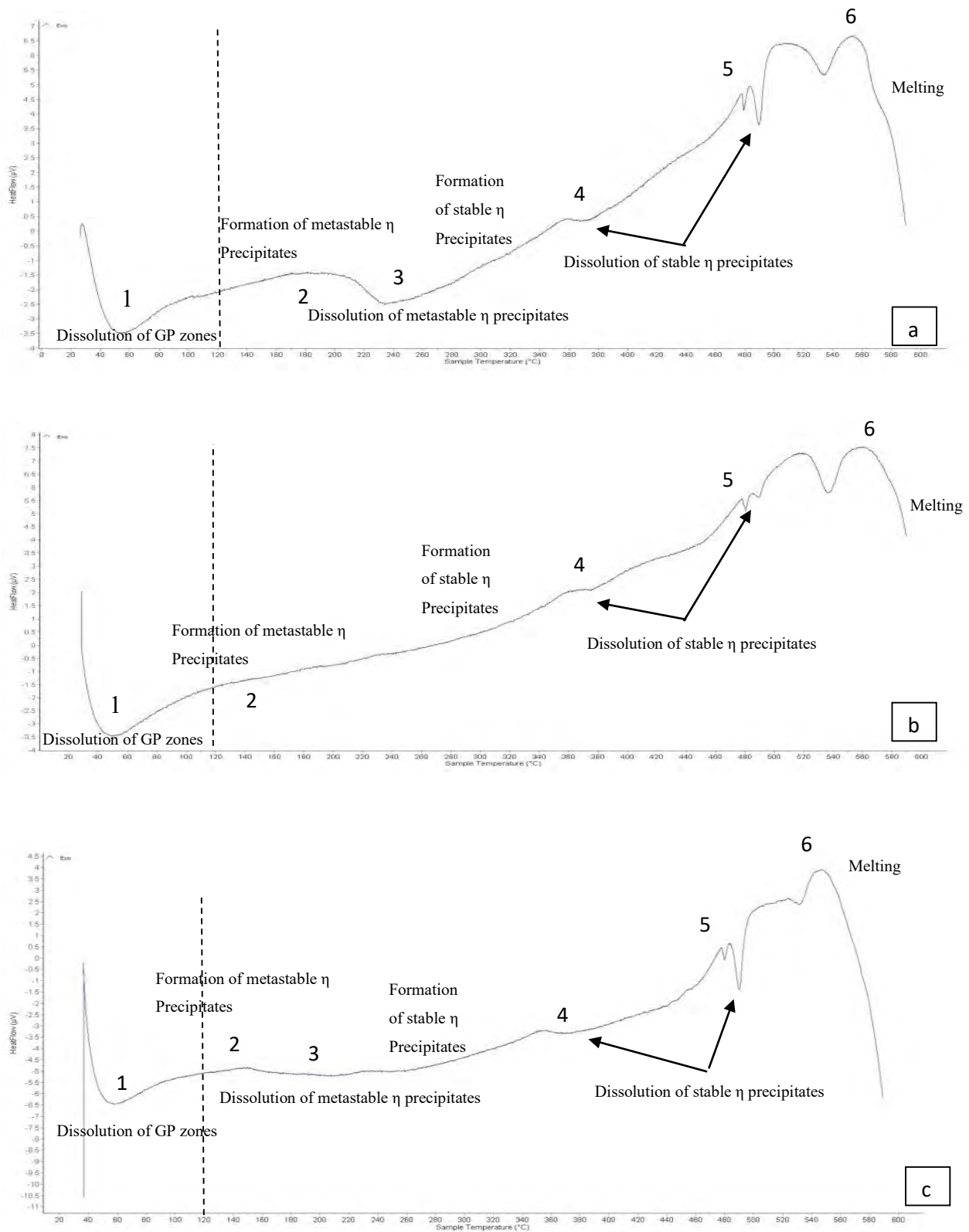
Figure 4.12 DSC Peaks of (a) Al 7075 (b) Ni added Al 7075 and (c) Ni and B added Al 7075.

4.8 Summary

Strength and toughness of all the three alloys were found much greater than the base aluminium metal. It is evident from the SEM, XRD and DSC results that the metastable, semi coherent η precipitates were produced during the ageing treatment. These η′ precipitates were responsible for higher strength through precipitation hardening [57 ,64, 66].

The results of the tensile tests had shown that the alloy 3 (Ni and B added Aluminium 7075) had the highest strength and toughness followed by alloy 2 (Ni added Aluminium 7075). Results from SEM and EDS had shown that the primary difference between the alloy 1 with the other two alloys was in the intermetallics. In alloy 2 and alloy 3 Al_2CuMg intermetallics was replaced by the less detrimental Al-Cu-Ni intermetallics [84]. In essence, although strength and toughness normally do not increase together but the formation of this Al-Cu-Ni intermetallics in alloy 2 and alloy 3 got rid of detrimental effects of Al_2CuMg which increased ductility and Al-Cu-Ni intermetallics itself are harder intermetallic which acted to increase the strength of the alloy. Thus strength and toughness both increased in alloy 2 and in alloy 3 [84, 85].

Addition of Boron although in the trace amount significantly affected the alloys, casting became better as the DAS became finer with the addition of boron. Another important effect of boron addition evident from the SEM images was that the average size and the distance between the intermetallics decreased and their distribution became fairly homogeneous in the nickel and boron added alloy thus increasing further strength and toughness [59,64-66].

CHAPTER 5
A Brief Review on Progressive Damage

5.1 Background Theory

According to Anderson [93], there are four common mechanisms in metals and metal alloys that may impose failure in a material. Three of them are cleavage fracture, intergranular fracture and fatigue. The relevant works focus on the fourth mechanism, ductile fracture.
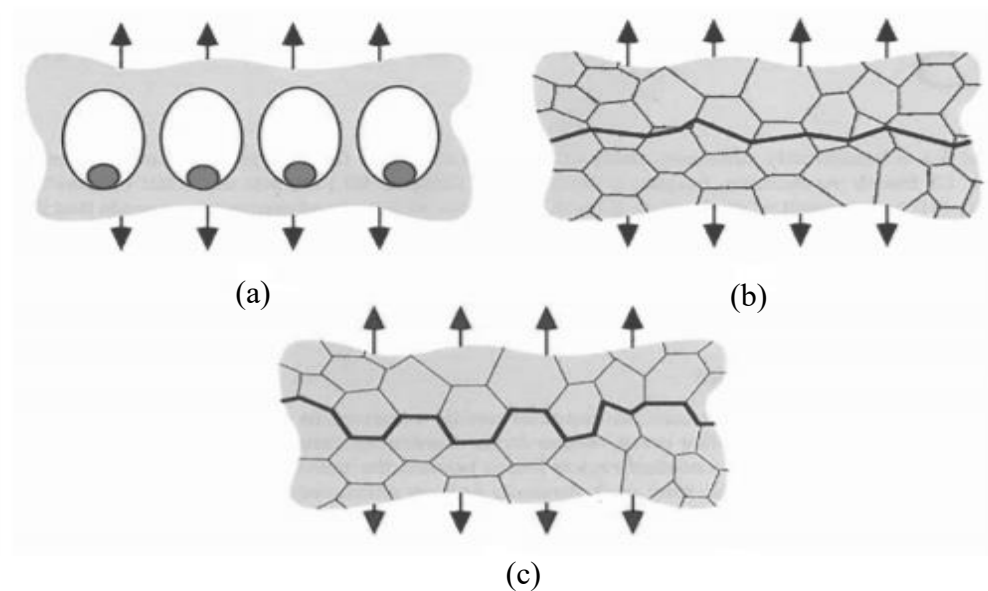
Figure 5.1 Three of the most common fracture mechanisms in metals and alloys (a) Ductile fracture (b) Cleavage (c) Intergranular fracture.

The mechanisms related to ductile fracture can generally be summed up into three stages [93]:

1. The formation of free surfaces around a particle inside the material, either by interfacial de-cohesion or fractures in the particle itself.
2. Growth of the voids created around particles, due to plastic straining and hydrostatic stress.
3. Coalescence of the growing voids that eventually leads to failure of the material.
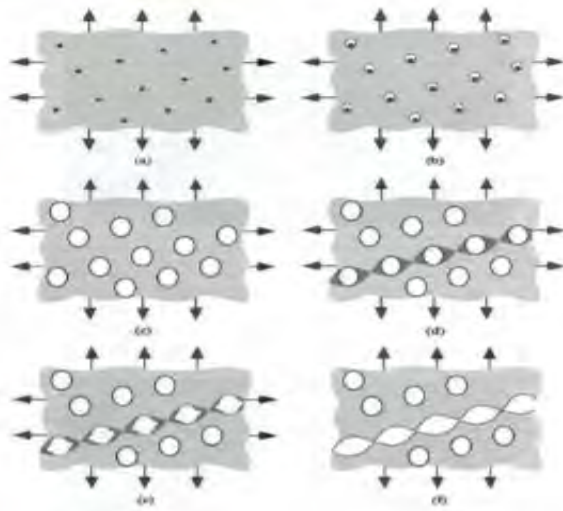
Figure 5.2 Growth of voids during ductile failure.

The growth of voids is for the most part concentrated around the larger particles in the material. A state of high stress triaxiality caused by high values of hydrostatic stress encourages the growth of voids around the larger particles. A state of lower stress triaxiality will in addition give void growth around the medium sized particles, giving a higher number of small voids evenly spread in the material [94].

5.2 Derivation of Failure Parameters in Ductile Damage:

5.2.1 Stress Triaxiality

Stress triaxiality, η is defined as the ratio of the mean stress and equivalent von Mises stress.

$$\eta = \frac{\sigma_m}{\bar{\sigma}} \tag{5.1}$$

Where, σ_m is the mean stress and $\bar{\sigma}$ is the equivalent von Mises stress.

According to von Mises [95, 96] If a material is isotropic then the mean stress can be written in terms of principal stresses as,

$$\sigma_m = \frac{1}{3}(\sigma_1 + \sigma_2 + \sigma_3) \tag{5.2}$$

Where, σ_m is known as mean stress or hydrostatic stress. Also, it is assumed that $\sigma_1 \geq \sigma_2 \geq \sigma_3$.

And in terms of principal stresses the von Mises stress is defined as,

$$\bar{\sigma} = \frac{1}{\sqrt{2}} \sqrt{(\sigma_1 - \sigma_2)^2 + (\sigma_2 - \sigma_3)^2 + (\sigma_3 - \sigma_1)^2} \qquad (5.3)$$

Stress triaxiality is used as a parameter to determine the state of stress in a body based on the hydrostatic stress and the von Mises equivalent stress. In materials that are subjected to ductile fracture, the stress triaxiality is an important parameter. The equivalent strain at which a material starts to fail (damage initiation) is highly dependent on the stress state of the material, hence the stress triaxiality [104].

5.2.2 Ductile Fracture Models and Calibration

Equivalent plastic strain to fracture $\bar{\epsilon}_f$ is widely used to characterize material ductility in engineering applications. One of the simplest fracture models is the constant fracture strain model, but it is generally accepted that $\bar{\epsilon}_f$ is not constant under different loading conditions. The stress triaxiality is an important parameter controlling material ductility. McClintock [97] and Rice and Tracey [98] analyzed the void growth under hydrostatic loading, derived a simple exponential expression for the function. In a two dimensional fracture locus

$$\bar{\epsilon}_f \propto e^{-C\eta} \qquad (5.4)$$

C is the material constant and typically $C = 1.5$. The models of void growth and their more recent extensions have become the foundation of the modern ductile fracture mechanics [97, 98, 99]. Johnson and Cook [20] integrated the effect of stress triaxiality, strain rate, and temperature into a simple equation of a separable form. Bao and co-worker [100, 101] designed and performed tests on several types of specimens to calibrate the fracture locus in a wide range of stress triaxiality. He showed that the fracture strain does not have to be a monotonically decreasing function of stress triaxiality [102, 103].

5.2.3 Stress Triaxiality of a Flat Plate

Experiments have shown that ductile fracture due to growth and coalescence of voids is initiated in the center of the volume. When a material is necking, a volume inside the necking zone is strained in tension in the direction of the main principle stress σ_1, and compressed in the two transverse directions because the thickness and width of the specimen is reduced by the necking phenomenon. This creates a state of high

hydrostatic stress leading to a higher state of tri-axial stress in the volume. A volume which is located nearer the edge of the specimen will not have the same amount of hydrostatic stress because the straining of this element is more of a shape altering strain than a volume changing one. The fracture of ductile metals is strongly dependent on hydrostatic stress, and therefore stress triaxiality. However, after necking the situation changes according to Bridgman equation of the stress triaxiality [104] at the center of the neck of a round specimen can be shown by equation 5.5.

$$\eta = \frac{1}{3} + \ln\left(1 + \frac{a}{2R}\right) \tag{5.5}$$

Where, R is the local radius of a neck in the round bar specimen, and a is the radius of the necking cross section.

But a flat specimen follows a modified version of this equation. Besides the analysis on necked round specimens in his famous book, Bridgman [104] also gave the approximate solutions for a necked plane strain specimen: Considering the stress state of the central point (x=0, z= 0) of the specimen, the mean stress, and the stress triaxiality are given, respectively, by the following equations:

$$\eta = \frac{\sqrt{3}}{3}\left[1 + 2\ln\left(1 + \frac{a}{2R}\right)\right] = \frac{\sqrt{3}}{3}\left[1 + 2\ln\left(1 + \frac{t}{4R}\right)\right] \tag{5.6}$$

Where, t is the ligament thickness of the flat specimen. Equation 5.6 implies that the range of stress triaxiality at the center of a plane strain specimen is $\eta \geq \frac{1}{3}$. It should be noted that the above analytical solution assumes the rigid-perfect plastic condition, but the difference of stress triaxiality between rigid-perfect plastic and elastic-plastic hardening is much small. The reason is due to the definition of stress triaxiality, which is the ratio of mean stress and equivalent von Mises stress the effect of strain hardening of material is partially removed and thus can be ignored.
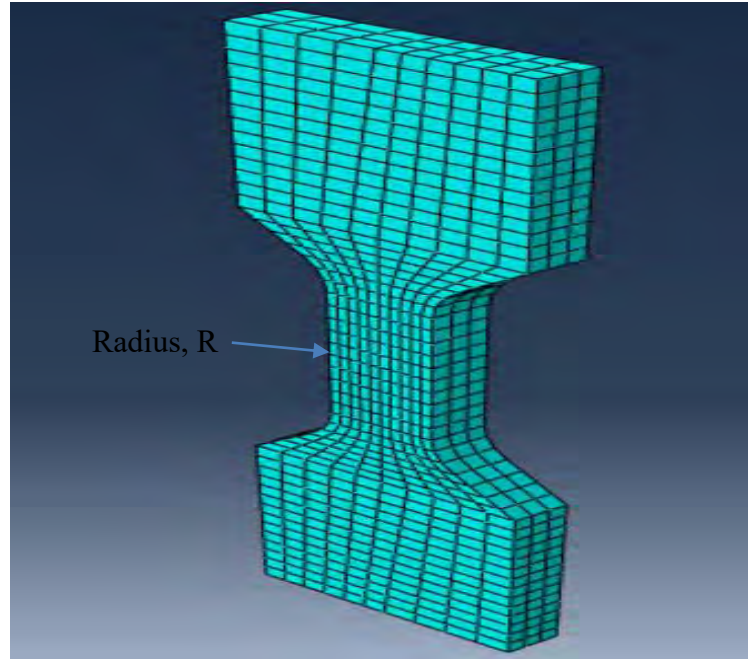
Figure 5.3 No notch were cut which made the radius of notch, R infinity.

5.3 Finite Element Method

Finite Element Method, FEM, is a numerical calculation method which solves various differential equations with the aid of computers. FEM divide a continuum into a finite number of elements. The characteristic feature of FEM is that instead of solving the differential equation for the whole continuum, they are solved approximately for the finite elements. The elements are connected at nodes holding the elements together. The nodal points are the ends of each element, each node has a number of degrees of freedom, DOF, such as translation and rotation in x and y for a 2D analysis and x, y and z-direction for a 3D analysis. From the values of the nodal DOF's the element behavior can be determined in a controlled manner with the aid of predefined equations, and since the mechanical behavior of the material is known, the corresponding mechanical behavior of each element is determined. This is performed for every single element forming the continuum allowing the possibility to obtain an approximate solution for the entire continuum [105].

5.4 ABAQUS

Abaqus is a finite element program consists of wide range of elements which make it possible to model any type of geometry. In a nonlinear analysis Abaqus automatically chooses and adjust the load increment and convergence tolerance during the analysis to ensure that an accurate solution is obtained. Abaqus consists of three main analysis products each one of them suitable for different physical problems. These analysis products are Abaqus/Standard, Abaqus/Explicit and Abaqus/CFD. Abaqus/Standard is a general-purpose analysis that can solve linear and nonlinear problems involving static, dynamic and other type of engineering problems; the standard uses the implicit method to solve the problems. Abaqus/Explicit is an analysis product used in special-purpose; this product uses an explicit dynamic finite element formulation. It is suitable for brief, transient dynamic events, such as impact problems. It is also preferred for problems involving large deformations, i.e. highly nonlinear problems. Abaqus/CFD is used to study fluid dynamics [105].

5.4.1 Progressive Damage in Abaqus

In Abaqus, the specification of a failure mechanism consists of four parts, represented in Figure 5.3. The undamaged material behavior is that represented by the point a-b-c-d'. In the initial section, a-b, the material response is linear elastic. The following sections are plastic, with plastic yielding and strain hardening sections are b-c. At point c, the damage initiation portion is started, after which the deformation is localized in a neck region of the test specimen. Due to damage, the material follows the curve of c-d instead of the undamaged response of c-d'. After the point c, there is an evolution of the degradation of the stiffness in the region of strain localization. Consequently, the failure mechanism is specified by defining the undamaged material response, the damage initiation criterion and the damage evolution law. And also, elements should be deleted after the material stiffness is fully degraded (point d).
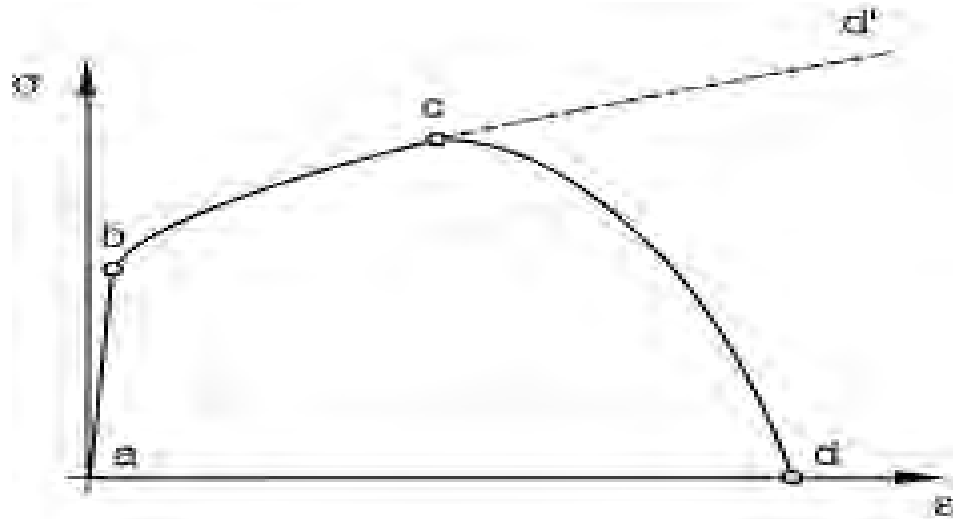
Figure 5.4 Typical stress-strain curves for a uniaxial test of a metal specimen, with regions for specifying failure mechanism indicated.

There are many theories that predict progressive damage and failure. Among them three theories are mainly relevant for practical applications these are:

- Progressive damage and failure for ductile metals.
- Progressive damage and failure for fiber-reinforced materials.
- Progressive damage and failure for ductile materials in low-cycle fatigue analysis.

In Abaqus, ductile damage initiation criterion is a model for predicting the onset of damage due to nucleation, growth, and coalescence of voids in ductile metals. The model assumes that the equivalent plastic strain at the onset of damage is a function of stress triaxiality and strain rate. The ductile criterion can be used in conjunction with the Mises, Johnson-Cook, Hill, and Drucker-Prager plasticity models, including equation of state. The ductile criterion assumes the equivalent plastic strain at the onset of damage to be a function of triaxiality, strain rate and equivalent plastic strain [105].

5.4.2 Damage Initiation and Evolution

Regarding the damage evolution, it is based on the damage being characterized by the progressive degradation of the material stiffness, which leads to material failure. The characteristic stress-strain curve with progressive damage degradation is presented in figure 5.4. In the figure 5.4, σ_{y0} and $\bar{\varepsilon}_0^{pl}$ is the yield stress and the equivalent plastic strain at the onset of damage respectively. The damage variable D reaches 1 at failure,

with the corresponding equivalent plastic strain at failure, $\bar{\varepsilon}_f^{pl}$. The undamaged stress is presented as $\bar{\sigma}$ for an elastic-plastic material with isotropic hardening, the damage results in softening of the yield stress and degradation of elasticity [105].
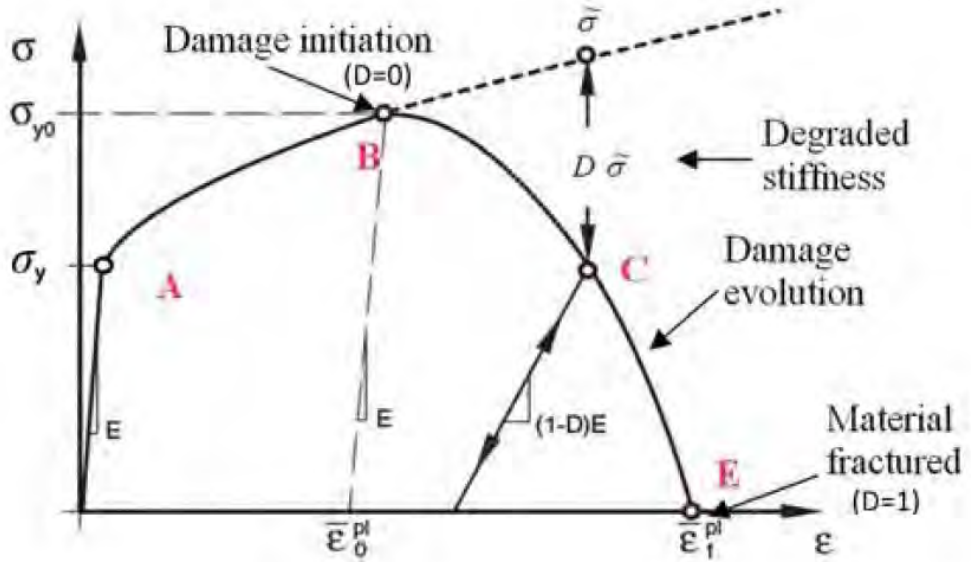
Figure 5.5 Stress-strain curve with progressive damage degradation.

The damage evolution is driven by mesh-independent measures; either plastic displacement, $\bar{\epsilon}^{pl}$ or physical energy dissipation,G_f. However, when material damage occurs, the stress-strain relationship cannot accurately represent the material behavior, otherwise leading to strong mesh dependency. Therefore, the damage evolution law is in Abaqus specified in terms of equivalent plastic displacement or as fracture energy dissipation, [105]. Before the damage initiation, $\bar{\epsilon}^{pl}$=0. Once a particular initiation criterion is satisfied, the material stiffness is degraded according to the specified damage evolution law, and the equivalent plastic displacement $\epsilon^{pl} = L\bar{\varepsilon}$. Here L is the characteristic length of the mesh element near necking zone. This damage evolution law describes the degradation rate of the material stiffness once the corresponding initiation criterion has been reached. The damage parameter is expressed as,

$$D = \frac{L\bar{\varepsilon}}{\bar{\epsilon}f} \tag{5.7}$$

Here, $\bar{\epsilon}^f$ is the equivalent plastic displacement at failure

When D=1, the mesh gets fully degraded and eliminated from the model and calculation [105].

5.4.3 Fracture Simulation in Abaqus

The tensile testing simulation of this thesis was conducted in Abaqus. In this section, a description of the material and damage models in Abaqus is presented. Only the models used in this thesis are presented here.

5.4.3.1 Material Model in Abaqus

In Abaqus, the material library consists of several material behaviors, including general properties (such as density and material damping), elastic mechanical properties, inelastic (plastic) material properties, thermal properties and more. The material behavior consisting general behavior and in this section, the material behavior used in this thesis will be presented, which include general properties along with elastic and plastic mechanical behavior.

The only general property used in this simulation was density, which can be defined as a fixed value or a function of temperature and field variables. Density is only required in explicit analysis. In an implicit analysis density would not be required. Regarding the elastic mechanical properties, there are several models in Abaqus, out of which the simplest one is linear elasticity. The linear elastic material model is only valid for small elastic strains and can be specified to be isotropic, orthotropic or anisotropic.

Similarly, to the elastic mechanical properties, the inelastic behavior also has several models. Many of the plasticity models have been developed for modeling metals, but are also applied to other materials. Even though different materials can behave in very different ways, the fundamental concepts of plasticity theories are sufficiently general to be applicable to a wide range of materials. In Abaqus, most of the plasticity models are "incremental" theories, in which the mechanical strain rate is divided into elastic and a plastic part. As most materials exhibit large plastic strains, the input to Abaqus should be given in true stress.

$$\sigma_{true} = \sigma_e(1 + \delta) \qquad (5.8)$$

And logarithmic plastic strain

$$\varepsilon_{ln}^{pl} = \ln(1 + \delta) - \frac{\sigma_{true}}{E} \qquad (5.9)$$

Where, σ_e and δ are the nominal stress and strain, receptively, gained from the uniaxial test and E is the Young's modulus.

Out of the possible plasticity models to use, in this thesis the one used is the classical metal plasticity model. It uses von Mises yield surface with associated plastic flow, perfect plasticity or isotropic hardening behavior and can be used in combination with models of progressive damage and failure. Mises surfaces assume the yielding of the material is independent of the equivalent pressure stress. The Mises yield surface is used to define isotropic yielding, by entering the uniaxial yield stress as a function of uniaxial equivalent strain, temperature and other field variables. Other properties that can be defined include heat generation by plastic work, strain rate dependence, hardening and more. No hardening is not needed to be defined if stress triaxiality is used in the simulation and the material is set to be a perfect plastic material, meaning the stress does not change with plastic strain. Furthermore, for Abaqus/Explicit an error tolerance is used to regularize the input data. This regularization value can be defined or is otherwise set to the default value of 0.03 [105].

5.4.4 Various Features in Abaqus

5.4.4.1 Implicit and Explicit Analysis in Abaqus

The characteristics of implicit and explicit methods make them suitable for different types of problems. Explicit methods demand less disk space and memory usage than the implicit solver, which is partly due to that no iteration is performed within each time step and partly due to the usage of the diagonal, lumped mass matrix, the system to be solved is uncoupled. The convergence problem that may be present in implicit methods can be avoided with an explicit method [106]. The greatest feature of the explicit method is the absence of a global tangent stiffness matrix, which is required with implicit methods. Since the state of the model is advanced explicitly, iterations are not required [107]. Another advantage of explicit method is the cost of calculations

due to increase number of DOFs. The difference is shown schematically in Figure 5.5. It is necessary to choice between explicit or implicit analysis during running an analysis in Abaqus. In dynamic analysis, the explicit time integration is favorable as solving problems containing high speed deformations within a short amount of time, because the method can calculate a high number of incremental points close together in time, at a low computational cost. It is preferred in cases where contact definitions between different part of a structure model are present [108, 109]. The element size and the time used to run an explicit analysis are directly linked together through the critical time increment size Δt_{cr}, as defined in section 5.4.4.6.
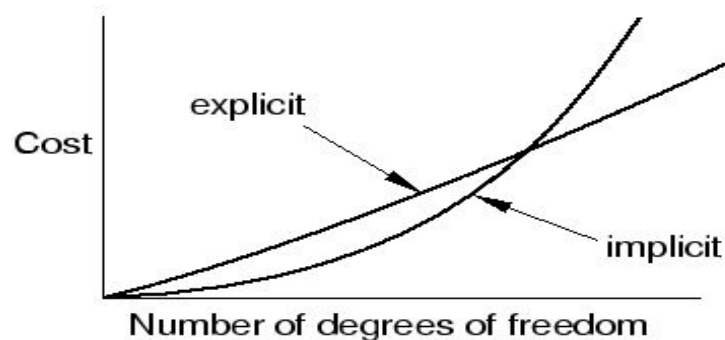
Figure 5.6 The difference in calculation cost between implicit and explicit solver.

5.4.4.2 Dynamic Analysis using Direct Integration Method

When performing a FE-analysis there are many different methods offered to perform dynamic analysis, each of them with advantages and disadvantages depending on the problems. One method that is often used for dynamic nonlinear analysis is the "explicit dynamic analysis method". For linear dynamic analysis, it will in most cases be more effective to use analysis methods based on nodal methods. They depend on calculating the eigenvalues of the system and then calculating the response of the model using these eigenvalues. The calculations performed in order to find the eigenvalue are costly, particularly since the number of eigenvalues that is needed for complicated structures is not known before starting the analysis. The explicit dynamic analysis method uses direct integration and integrates the global equation of motion through time. For linear analysis this is not very effective, but for non-linear analysis this direct-integration method is often more effective. Direct integration is used to calculate the response history step-by-step in time. Each data point is calculated as a time Δt increment after the previous calculations.

5.4.4.3 Explicit Analysis

In the explicit analysis, the displacement and the velocity at the beginning of each increment are known. This means that the global mass and stiffness matrix need not be formed and inverted for each increment, saving much computational work. The sizes of the time increments however, have to be smaller than a critical time increment Δt_{cr}. This makes the method conditionally stable, and the increments must be kept small enough to preserve the stability of the result. Since the incremental steps are small, the incremental result will never greatly deviate from the exact solution, and any inaccuracy will most likely be corrected when calculating the next increment. Because of this there is often no need to control the accuracy as with the implicit method.

The explicit procedure is well suited for high-speed dynamic events, and slower quasi-static analysis. In the case of high speed events, the small increments mean that more detailed calculations are made and large deformation occurring over a short time can be captured. For quasi-static analysis, the deformation is assumed to be too slow to cause dynamic response in the structure. The dynamic effect can be neglected. The treatment of contact is also simplified, making it a good choice for dynamic or quasi-static analysis containing contact between surfaces. The total time needed to run the analysis is linearly dependent on the size of the model and the total time simulated, assumed that the mesh size is kept constant. An increase of any of the two factors will result in an equal increase in calculation time.

The explicit method is preferred before the implicit method because of the ability to convert the mass matrix to a diagonal matrix, often referred to as lumped mass. This reduces the number of calculation needed for each time increment with up to 4000 times for a three dimensional FE-analysis [110]. Also the amount of data storage needed for each increment calculation is much smaller for the explicit method [111].

Equation of motion can be a proper example of such explicit calculation using direct integration method. For non-linear problem the equation of motion can be generalized as [110].

$$[M]\ddot{u}_n + [C]\dot{u}_n + R^{int}{}_n = R^{ext}{}_n \tag{5.10}$$

Where, [M] is the lumped mass matrix of the system, [C] is the systems dampening matrix, R^{int} is the internal load vector and R^{ext} is the external load vector. The equation is calculated at the time increment n. The time factor is discretized using a finite difference approximation of the time derivatives. This can be done in many ways, but for application to dynamic events, the explicit time integration is best suited.

5.4.4.4 Central Difference Method

The explicit analysis method makes use of the central difference method to calculate the state of the next increment. The equilibrium equations are satisfied at the beginning of each increment (t_i). The acceleration at t_i is used to find the velocity at $t_{i+\frac{1}{2}}$ and the displacement t_{i+1}. Each calculation is relatively inexpensive, and is done using "lumped" element mass matrices. The velocity $\dot{u}^N_{i+\frac{1}{2}}$ and the displacement u^N_{i+1} is calculated as

$$\dot{u}^N_{i+\frac{1}{2}} = \dot{u}^N_{i-\frac{1}{2}} + \frac{\Delta t_{i+1}+\Delta t_i}{2}\ddot{u}^N_i \qquad (5.11)$$

$$u^N_{i+1} = u^N_i + \Delta t_{i+1}\dot{u}^N_{i+\frac{1}{2}} \qquad (5.12)$$

Where u^N is a degree of freedom, and the subscript i is the increment number in the analysis [112].

The efficiency of the procedure comes from the use of lumped stiffness matrices, which are diagonal. This makes it easier to calculate the acceleration at the beginning of each increment of Equation 5.13, as the matrices are easy to invert and the vector multiplication only demands one operation for each degree of freedom. The acceleration is the calculated as

$$\ddot{u}^N_i = ([M]^{NJ})^{-1}R^{ext J}_i - R^{int J}_i \qquad (5.13)$$

Where, $[M]^{NJ}$ is the mass matrix, $R^{ext J}_i$ is the applied load vector and $R^{int J}_i$ is the internal force vector. The internal force vector is assembled with contributions from individual elements in such a way that a global stiffness matrix is not needed [112].

5.4.4.5 Stability

The stability of the procedure is dependent on the highest frequency of the system. Equation 5.14 shows the limit for a system with and without damping in the system, respectively.

$$\Delta t \leq \frac{2}{\omega_{max}} \left(\sqrt{1 + \xi_{max}^2} \right) - \xi_{max} \tag{5.14}$$

$$\Delta t \leq \frac{2}{\omega_{max}} \tag{5.15}$$

Here ω_{max} is the maximum natural frequency, and ξ_{max} is the corresponding dampening ratio. In Abaqus, a small amount of dampening in the form of bulk viscosity is introduced to the system in order to control the high frequency oscillations that can occur during an analysis. This effect is by default applied as a linear effect, but for solid continuum elements it can also be a quadratic effect that is used in compression state in order to prevent elements experiencing high velocity gradients when collapsing, and the volume is suddenly reduced to zero [105].

5.4.4.6 Estimation of the Stable Time Increment Size

The size of the stable time increment Δt is often estimated as being smaller than a critical time increment size Δt_c, [113], that is

$$\Delta t \leq \Delta t_c = \frac{l_{min}^e}{c_d} \tag{5.16}$$

Where, l_{min}^e is the smallest element dimension on the model, and c_d is the speed of sound in the material [110] over the element. This is just an estimated value of the maximum stable time increment. In most cases, it is wise to use a shorter time increment for the analysis. For two-dimensional models Abaqus uses a reduction factor between $1/\sqrt{2}$ and 1, and for three-dimensional models $1/\sqrt{3}$ and 1. The speed of which the stress wave travels through a material is dependent on the Young-modulus E and the density ρ of the material.

$$c_d = \sqrt{\frac{E}{\rho}} \tag{5.17}$$

From this it is clear that the critical time increment is increased if the material is softer (low Young-modulus) or has a high density. This can be used to manipulate the time needed to run the explicit analysis on a computer.

5.4.4.7 Energy Monitoring

In an explicit dynamic analysis, the energy in the model is important to monitor. The total energy in the model should be close to constant, and the artificial energies should be negligibly small compared to "real" energies as strain energy and kinetic energy. For quasi-static analysis, the amount of kinetic energy should not exceed a certain fraction of the strain energy. For cases involving contact or constraints, it is wise to monitor the energy dissipated by constraint penalty and contact penalty. They should be close to zero in all cases [105].

5.4.4.8 Energy Balance

Energy output comprises of several components, comparison between these various energy components is used to evaluate whether the analysis is having appropriate response. The energy balance for the entire model can be written as

$$E_I + E_V + E_{FDI} + E_{KE} + E_{IHE} - E_W - E_{PW} - E_{CW} - E_{MW} - E_{HF} = E_{Total} \qquad (5.18)$$

where E_I is the internal energy, E_V is the viscous energy dissipated, E_{FDI} is the frictional dissipated energy, E_{KE} is the kinetic energy, E_{IHE} is the internal heat energy, E_W is the work done by the external applied loads and E_{PW}, E_{CW} and E_{MW} are the work done by contact penalties, constraint penalties and propelling added mass respectively. E_{HF} is the external energy through external fluxes. The sum of these components is E_{Total}, which should be constant. However, for numerical models this is seldom the case, E_{Total}, is only approximately constant, generally with an error of 1%.

The internal energy component, E_I, in equation 5.19 is in turn composed of several other components. The expression for the internal energy is [114].

$$E_I = E_E + E_P + E_{CD} + E_A + E_{DMD} + E_{DC} + E_{FC} \qquad (5.19)$$

Where, E_E is the recoverable elastic strain energy, E_P is the dissipated energy through inelastic processes such as plasticity, E_{CD} is the dissipated energy through viscoelasticity or creep, E_A is the artificial strain energy, E_{DMD} is the dissipated energy through damage, E_{DC} is the dissipated energy through distortion control, E_{FC} is the fluid cavity energy [105].

5.4.4.9 Element Type

In Abaqus, for each type of analysis, a wide range of elements is available to the user for a 3D model. Figure 5.6 shows the element families that are used most commonly in a stress analysis; in addition, continuum (fluid) elements are used in a fluid analysis. One of the major distinctions between different element families is the geometry type that each family assumes. The first letter or letters of an element's name indicate to which family the element belongs. For example, S4R is a shell element; CINPE4 is an infinite element [105].
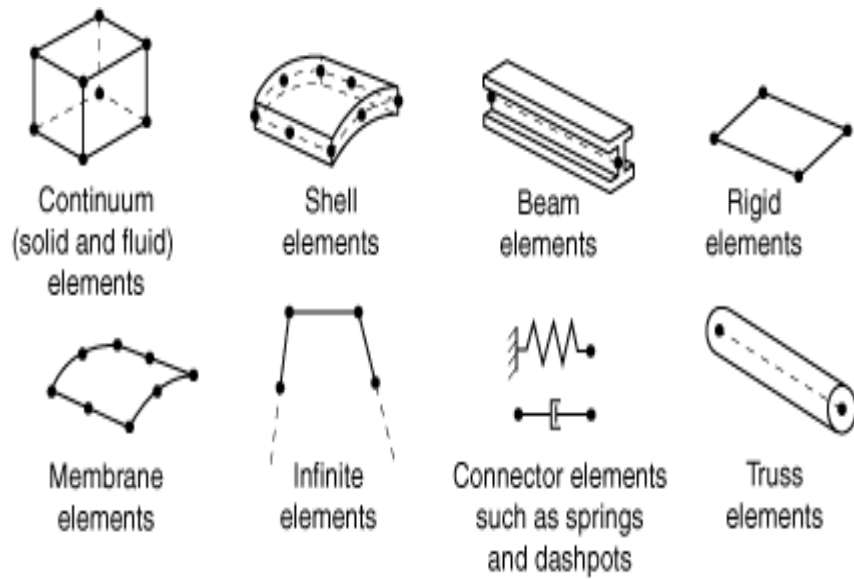
Figure 5.7 Various element families.

5.4.4.10 C3D8 and C3D8R mesh types

In Abaqus C3D8 elements are continuum solid brick elements with 2*2*2 fully integrated integration points as shown in figure 5.7 [111].
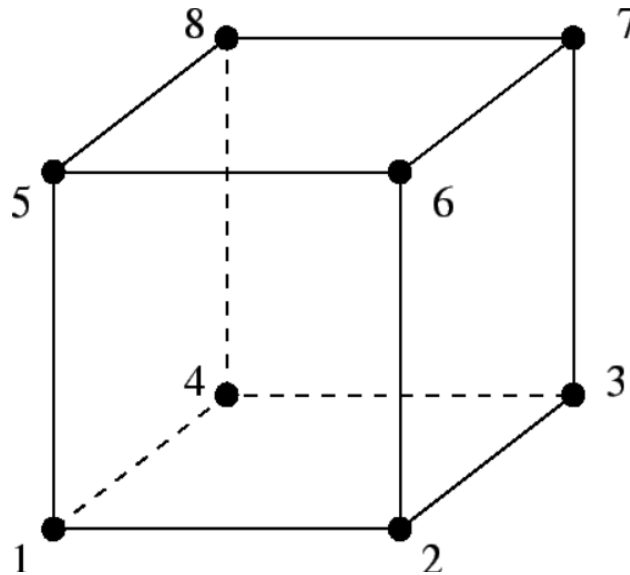
Figure 5.8 Eight node brick elements.

The C3D8R is also a general purpose brick element but it has only one integration point in each element as shown in figure 5.8 [111].
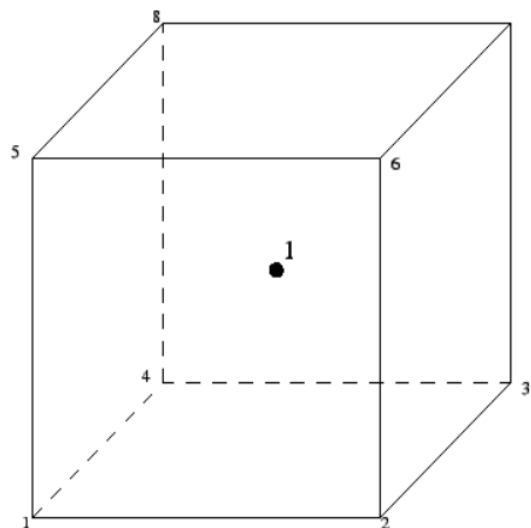
Figure 5.9 Eight node brick element with reduced integration point.

CHAPTER 6
Finite Element Model Development

Knowing when and how a material will fail leads to a more efficient design and use of material. There are many software that helps analyze material failure by incorporating progressive failure element option by allowing to reduce material stiffness gradually into their software. In order to explore the progressive failure feature, tests with accepted results was modeled.

6.1 Finite Element Analysis

In this thesis the finite element simulation was carried out using commercial software Abaqus/CAE. Figure 6.1 shows the welcome screen of Abaqus/CAE 6.14 which is an engineering tool that is used to solve various complex engineering problems ranging from linear to non-linear problems. The software is used all over the world in industries and also in academic purpose. Abaqus/CAE enables models to be solved as quickly as possible by simply creating the geometry under investigation with the right material properties associated to it, loading and also by applying the boundary conditions to the material to be modeled.
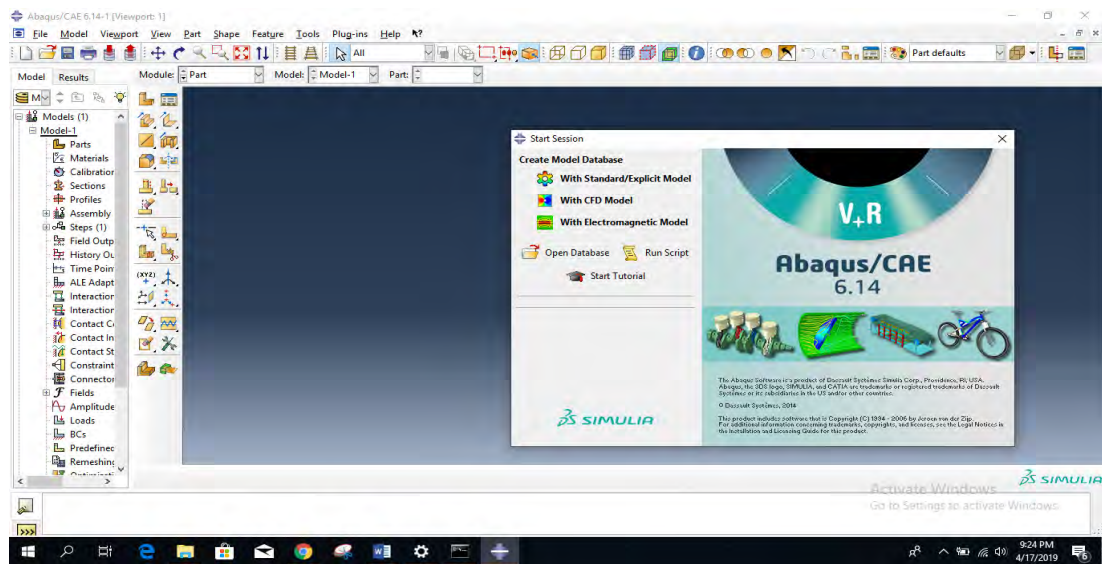
Figure 6.1 Welcome screen of Abaqus/CAE 6.14.

6.2 Finite Element Model and Geometry of Tensile Test

The finite element models were created using the Abaqus/CAE preprocessor, the test specimens were modeled on Abaqus in accordance with the tensile sample dimension mentioned in table 6.1. Figure 6.2 shows the two dimensional model of the samples from the experiments.

Table 6.1 Dimension used in the CAE model.

Gauge length	Width	Thickness	Fillet radius	Overall length	Length of reduced section	Length of grip section	Width of grip section
25mm	15mm	4mm	6mm	80mm	32mm	22.5mm	7.5mm
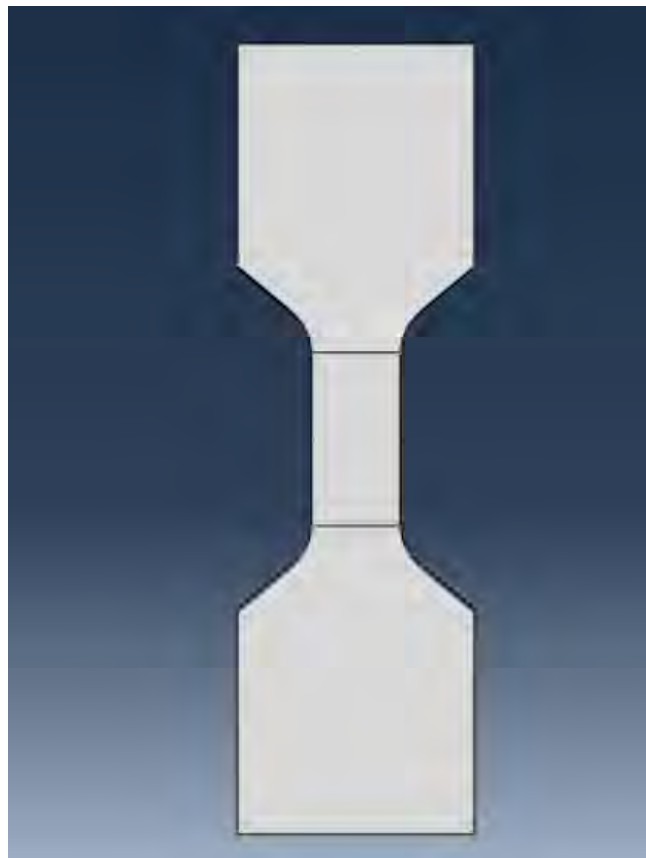
Figure 6.2 2-D model of the sample.

6.3 Material Properties

Three different alloys were selected to do the tensile simulation. Simulations were carried out until fracture. To run these simulations many material properties were used. These properties are listed in this section.

6.3.1 Density

Density data were taken from the experimental section 3.5.2. They are listed here again for convenience.

- Aluminium 7075= 2.87 g/cm^3.

- Nickel added Aluminium 7075=2.75 g/cm^3.

- Nickel and Boron added Aluminium 7075=2.8158 g/cm^3.

6.3.2 Plastic and Elastic Parameters

To simulate tensile damage and failure, tensile data in the load-elongation form were collected. This data later converted into stress-strain form. But to use these data in finite element software we needed true stress-plastic strain data because Abaqus only accepts true stress- plastic strain data. True stress and true strain data were calculated with equation 6.1 and 6.2.

$$\sigma = \sigma_e(1+\delta) \tag{6.1}$$

$$\in = \ln(1+\delta) \tag{6.2}$$

- σ = True stress.

- $\in$ = True strain.

- σ_e = Engineering stress.

- δ = Engineering strain.

In Abaqus, required variable Young's modulus is the slope of true stress-true strain curve so that Abaqus can rebuild the curve by using as little number points as possible. From the true stress true strain curve Young's modulus is calculated with the equation 6.3.

$$\text{Young's modulus} = \text{True stress at yield} / \text{True strain at yield} \tag{6.3}$$

In order to include plasticity within Abaqus, the stress-strain points must be converted into the form of true stress and logarithmic plastic strain. The logarithmic plastic strain can be calculated with the equation 6.4

$$\epsilon^{\text{plastic}} = \ln(1+\delta) - \frac{\sigma}{E} \tag{6.4}$$

6.3.3 Ductile Damage Properties

In the ductile damage feature Abaqus/CAE take plastic strain at damage initiation. Due to nucleation, growth, and coalescence of voids ductile damage is a function of stress triaxiality and strain rate. In the damage parameters strain rate can readily be obtained from the experiment itself. In our case the strain rate was 0.25 mm/min. For stress triaxiality as a practical approach, the stress triaxiality is used to identify the state of stress and is defined by the ratio of mean stress σ_m and von Mises equivalent stress $\bar{\sigma}$ [95, 96].

$$\text{Stress triaxiality, } \eta = \frac{\sigma_m}{\bar{\sigma}} \tag{6.5}$$

$$\text{Where, } \sigma_m = \frac{\sigma_1 + \sigma_2 + \sigma_3}{3} \tag{6.6}$$

In the case of uniaxial tension

$$\sigma_m = \frac{\sigma}{3} \tag{6.7}$$

$$\bar{\sigma} = \frac{1}{\sqrt{2}} \sqrt{(\sigma_1 - \sigma_2)^2 + (\sigma_2 - \sigma_3)^2 + (\sigma_3 - \sigma_1)^2} \tag{6.8}$$

In the case of uniaxial tension

$$\bar{\sigma} = \sigma \tag{6.9}$$

where, $\sigma_1, \sigma_2, \sigma_3$ = stresses in three directions. Using the equation 6.5 to 6.9 the value of stress triaxiality leads to 0.33 [110]. So, it can be assumed that the stress triaxiality value remains 0.33 up to necking. But during the necking phenomenon the stress ratio changes as shown in section 5.2.3 [99].

$$\eta = \frac{\sigma_m}{\bar{\sigma}} = \frac{\sqrt{3}}{3} \left[1 + 2\ln\left(1 + \frac{a}{2R}\right) \right] = \frac{\sqrt{3}}{3} \left[1 + 2\ln\left(1 + \frac{t}{4R}\right) \right] \tag{6.10}$$

So, stress ratio for the whole simulation can be described as

$$f(\eta) = \begin{cases} \frac{1}{3}, & t = t_0 \\ \frac{\sqrt{3}}{3}\left[1 + 2\ln\left(1 + \frac{t}{4R}\right)\right], & t < t_0 \end{cases} \qquad (6.11)$$

Since, our specimen is a flat plate the radius R is equals to the infinity and hence the equation 6.11 is reduced into 6.12.

$$f(\eta) = \begin{cases} \frac{1}{3}, & t = t_0 \\ \frac{\sqrt{3}}{3} & t < t_0 \end{cases} \qquad (6.12)$$

Albeit R did not remain infinity in the whole time of the experiment as the specimen showed some necking but the amount of necking is so small that the equation 6.12 remains a close approximation.

And the required fracture strain variable in Abaqus ductile damage module refers to the equivalent plastic strain to fracture from the uniaxial tensile test experiment. This equivalent plastic strain to fracture can be calculated from the stress-strain diagram as the total plastic strain at rupture.

The Abaqus/CAE ductile fracture material model is based on phenomenological criterion for predicting the onset of damage due to nucleation, growth, and coalescence of voids. The criterion for fracture/damage initiation is met when the condition in equation 6.13 is satisfied [105].

$$\int \bar{\omega}_D = \int \frac{d\epsilon^{pl}}{\epsilon_D^{pl}(\eta)} = 1 \qquad (6.13)$$

Damage parameter $\bar{\omega}_D$ is a state variable increasing monotonically with plastic deformation. It is zero for undamaged material, and equal to one for totally damaged material. The model assumes that the equivalent plastic strain at the onset of fracture $\epsilon_D^{pl}(\eta)$ is a function of triaxiality η. An overall change of stress triaxiality that is possible during failure is given in figure 6.3 [102].
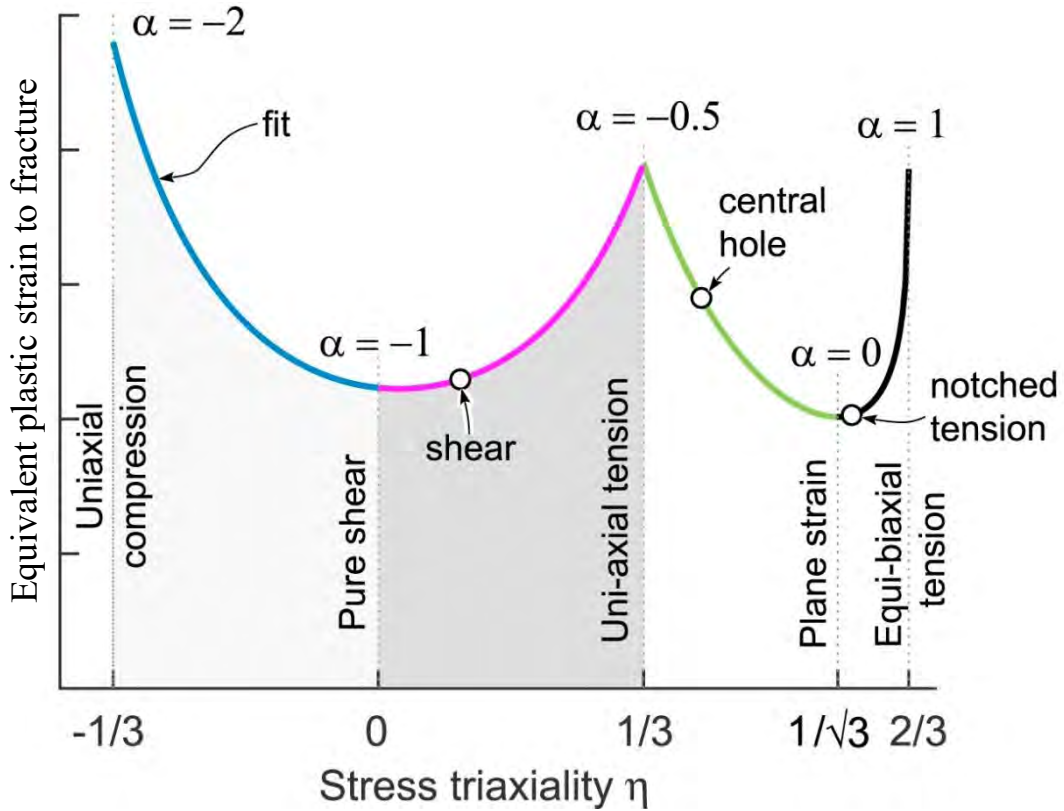
Figure 6.3 Stress triaxiality in various possible scenario.

6.4 Steps

In Abaqus steps involve two different sections. First one is called initial step. Abaqus/CAE creates a special initial step at the beginning of the model's step sequence. Abaqus/CAE creates only one initial step for the model and it cannot be renamed, edited, replaced, copied, or deleted [105].

Another one is called analysis step. It can involve one or more steps. In this model it had only one step called dynamic and explicit step. In this step non-linear geometry effects were kept on allowing for geometric non-linear effects to be included. Time increment was kept automatic so that Abaqus could automatically decide how much the increments should be by maintaining the stability following the equation 6.14.

$$\Delta t \leq \Delta t_c = \frac{l^e_{min}}{c_d} \tag{6.14}$$

Where, l^e_{min} is the smallest element dimension on the model, and c_d is the speed of sound in the material, Δt_c is the critical time increment size [110]. Mass scaling as shown in figure 6.4 was done about a factor of 2000 as a way of reducing

computational cost by scaling the mass of the smallest elements without altering the results [105].
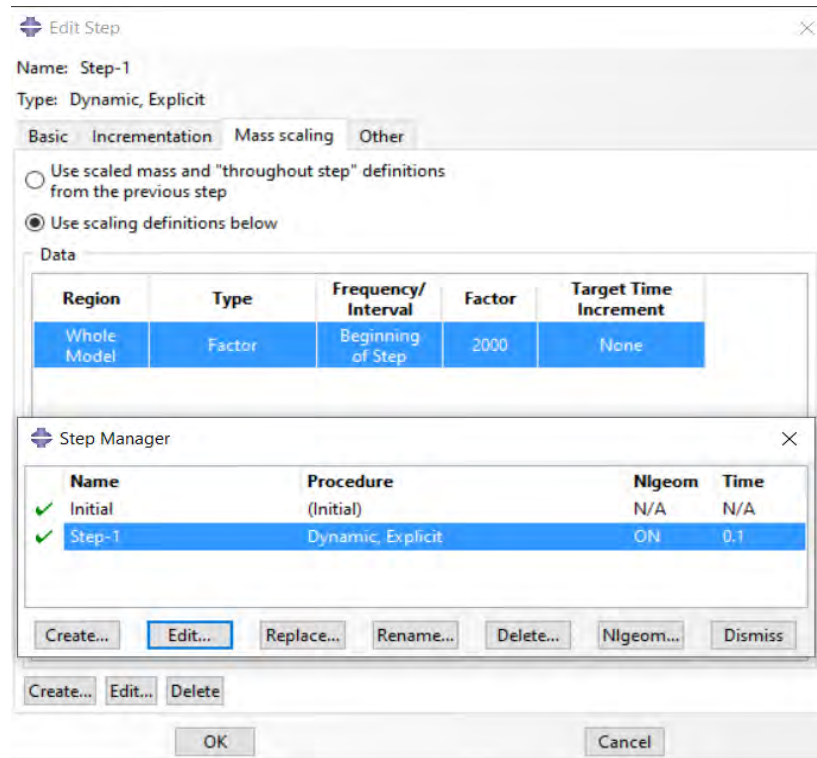
Figure 6.4 Mass scaling of the job.

6.5 Load

The boundary conditions in figure 6.5 were chosen to best simulate the clamped ends on the tensile test piece when it was stretched. In one end (lower end) applied boundary conditions restrained all degrees of freedom, on all the nodes along the edge. In the other end (upper end) all the nodes along the edge were restrained against all translation and rotations, except the translation in the y-direction. This was kept free to be able to strain the model. The elongation of the model was controlled by applying a constant strain having the same strain rate as in the experiment. The specimen was strained up to 150% of the total plastic strain (i.e. if the total plastic strain was 2 then it was stretched up to plastic strain value of 3). All of the boundary conditions were applied to the geometry of the model, and not directly to the nodes. This made it possible to change the mesh of the model without having to redefine the regions of the boundary conditions.
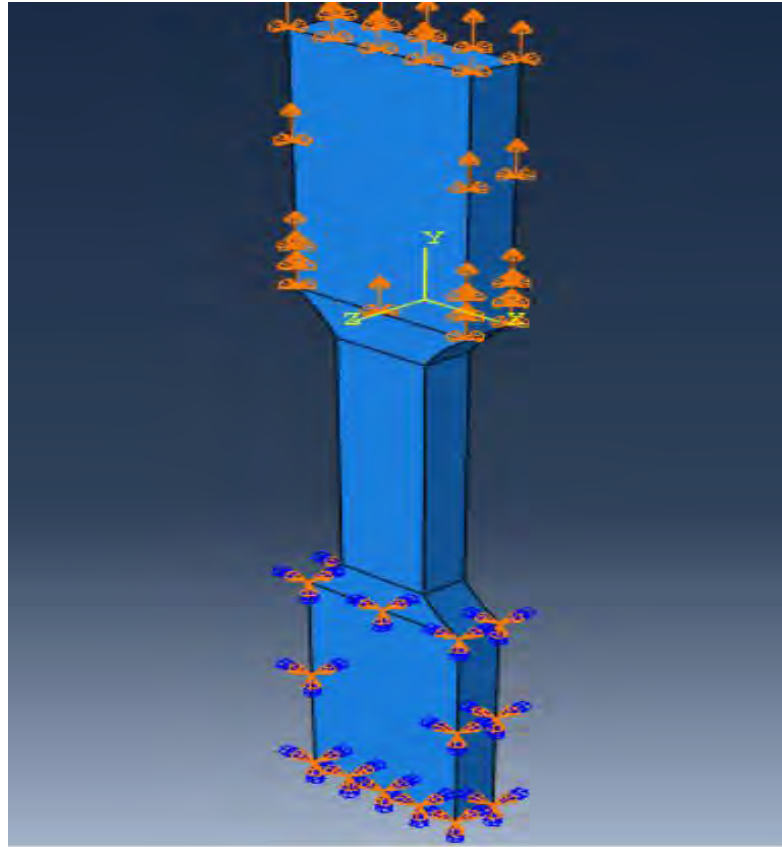
Figure 6.5 Boundary conditions.

6.6 Mesh

Meshing was done in four different ways with C3D8 and C3D8R 8-node linear brick, hourglass control mesh elements for each sample. They both had the same shape functions [114]. C3D8R follows reduced integration method so that they can avoid locking phenomenon. Also, another great advantage of C3D8R over C3D8 is it saves a lot of computational power. Still these C3D8R elements have several disadvantages against C3D8.

- Without proper hourglass control C3D8R mesh shows deviated results as in these situations there are 12 false zero energy modes.
- The integration of stresses and strains are accurate in points but in C3D8R integration is done in the middle of the cubes thus the model requires smaller elements to give accurate results.
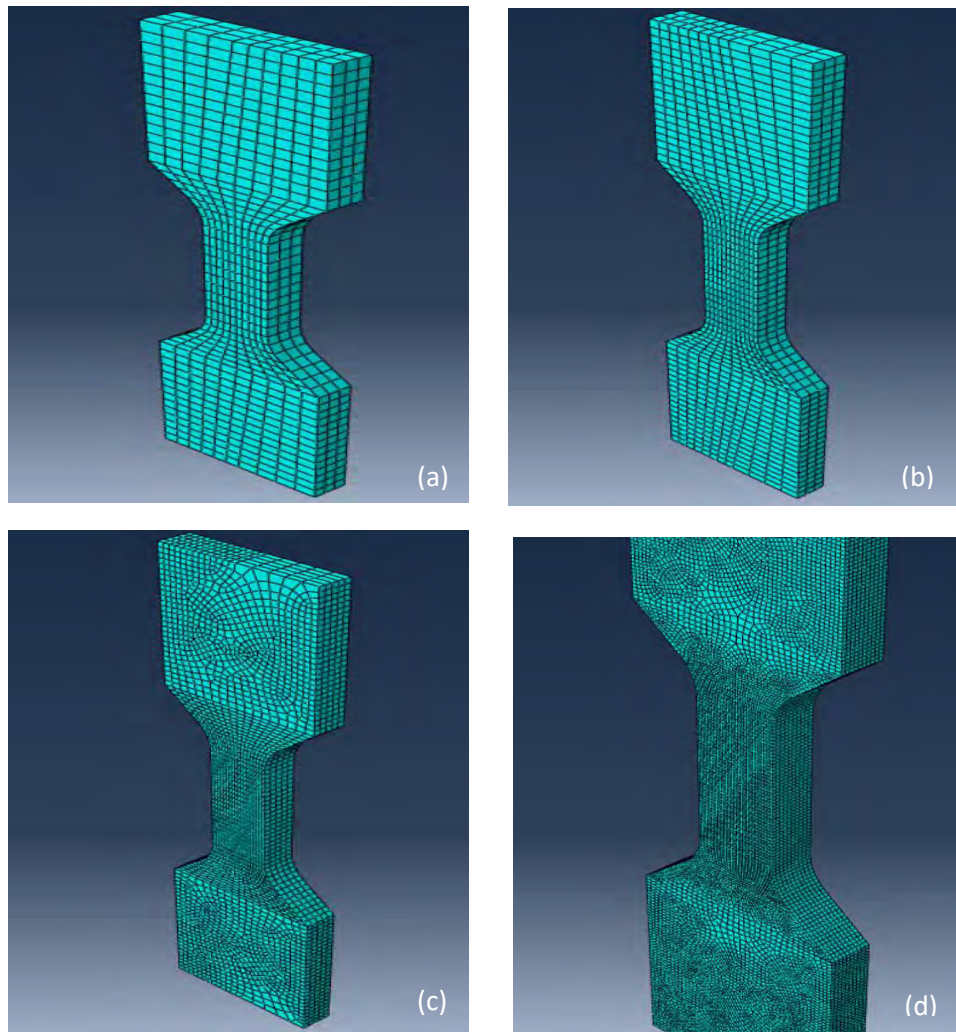
Figure 6.6 Mesh sizes (a) 1.6 mm (b) 1.2mm (c) 0.8mm and (d) 0.4mm.

So, there are advantages and disadvantages in both sides. In this thesis both mesh types were used to simulate the experiment. Also, among the three types of technique that were available for meshing (i.e. structured, sweep and bottom-up meshing technique) sweep mesh technique was used in this thesis for better mesh element quality although higher number of nodes were created in sweep mesh technique.

6.7 Job

For each simulation an explicit analysis was used with single precision method. Job was monitored to tabulate the data of total increment, element number, and nodal number for comparing the result in chapter 7.

6.8 Progressive Damage Failure Simulation of Alloys

6.8.1 Al 7075 Progressive Damage Failure Simulation

According to the discussion in section 6.3 the properties required for the simulation are presented for the alloy 1 (Al 7075).

- Elastic modulus: 1816.42 GPa.
- Density: 2.87g/cm^3.
- Poisons ratio: 0.33.
- Stress Triaxiality:

$$f(\eta) = \begin{cases} \dfrac{1}{3}, & t = t_0 \\ \dfrac{\sqrt{3}}{3} & t < t_0 \end{cases}$$

- Strain rate: 0.25 mm/min

To obtain stress-strain values, data were taken from the experiment as load-displacement data and then used in Abaqus graph generator to create stress-strain data and true stress- true strain data. Figure 6.7 and figure 6.8 shows engineering stress-strain data and converted true stress-strain data respectively.
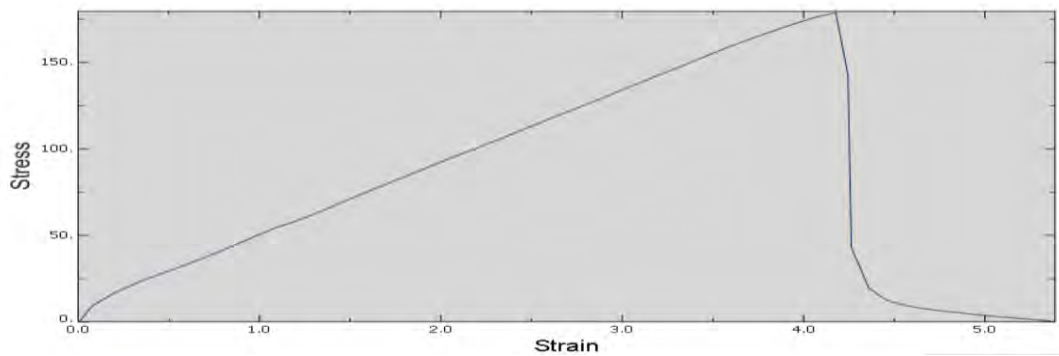
Figure 6.7 Engineering stress - Engineering strain data of Al 7075.
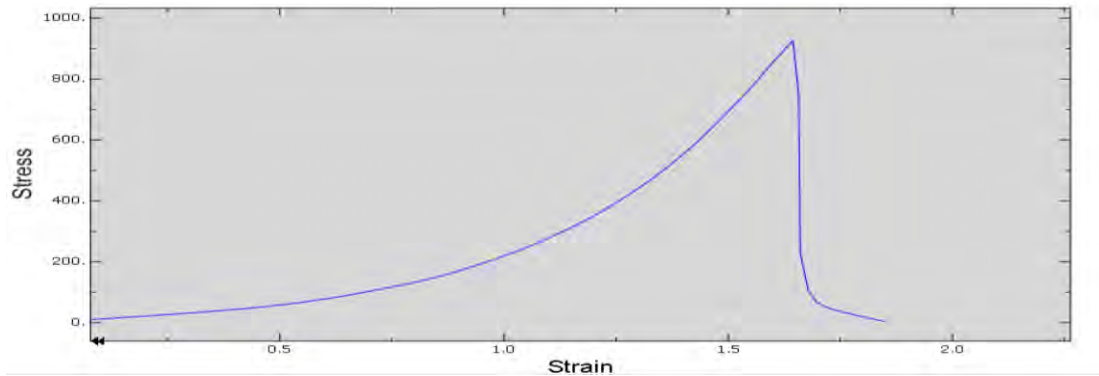
Figure 6.8 True stress-True strain data of Al 7075.

6.8.2 Ni Added Al 7075 Progressive Damage Failure Simulation

The properties of nickel added aluminium 7075 alloy are the following:

- Elastic Modulus = 2117 GPa.

- Density = 2.75 g/cm^3.

- Poisson's Ratio =0.33.

- Strain rate = 0.25 mm/min

- Stress triaxiality =

$$f(\eta) = \begin{cases} \dfrac{1}{3}, & t = t_0 \\ \dfrac{\sqrt{3}}{3} & t < t_0 \end{cases}$$

For stress strain values, data were taken from the experiment as load-displacement data and then used Abaqus graph generator to create stress-strain data and true stress- true strain data. Figure 6.9 shows engineering stress-strain data generated from the load-displacement data. Using the curve in figure 6.9 true stress-true strain data were generated in calibration mode of Abaqus as shown in figure 6.10.
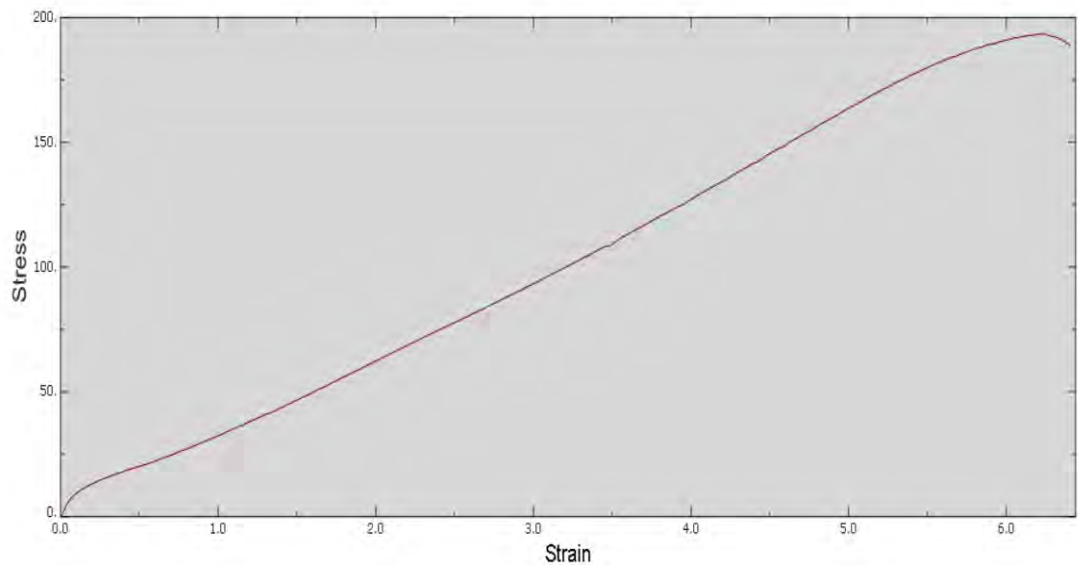
Figure 6.9 Engineering stress - Engineering strain data of Ni added Al 7075.
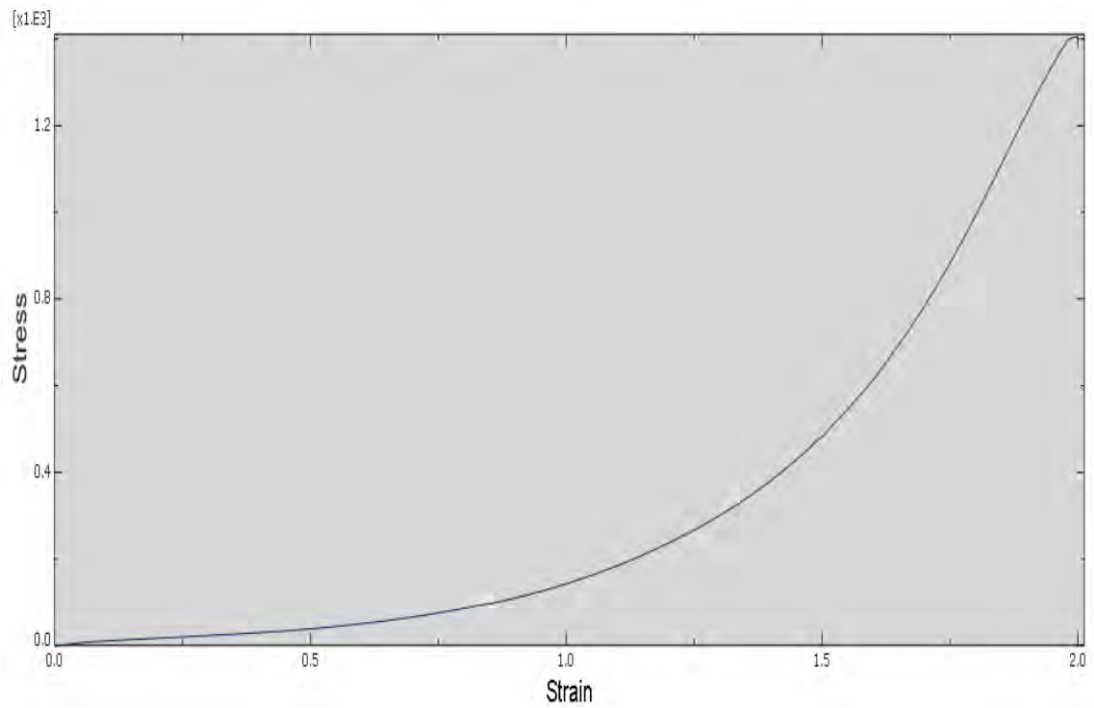
Figure 6.10 True stress-True strain data of Ni added Al 7075.

88

6.8.3 Ni and B Added Al 7075 Progressive Damage Failure Simulation

The properties of nickel and boron added aluminium 7075 alloy are the following.

- Elastic Modulus = 1848.2 GPa.

- Density = 2.8158 g/cm^3.

- Poisson's Ratio =0.33.

- Strain rate = 0.25 mm/min

- Stress triaxiality =

$$f(\eta) = \begin{cases} \dfrac{1}{3}, & t = t_0 \\ \dfrac{\sqrt{3}}{3} & t < t_0 \end{cases}$$

Engineering stress- engineering strain data generated in Abaqus as shown in figure 6.11 and figure 6.12 shows the true stress-true strain data generated in Abaqus with calibration mode.
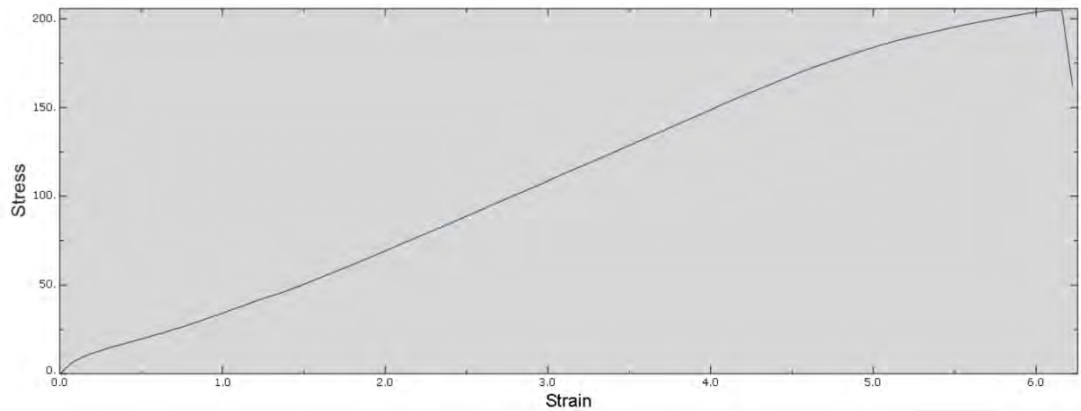
Figure 6.11 Engineering stress - strain data of Ni and B added Al 7075.
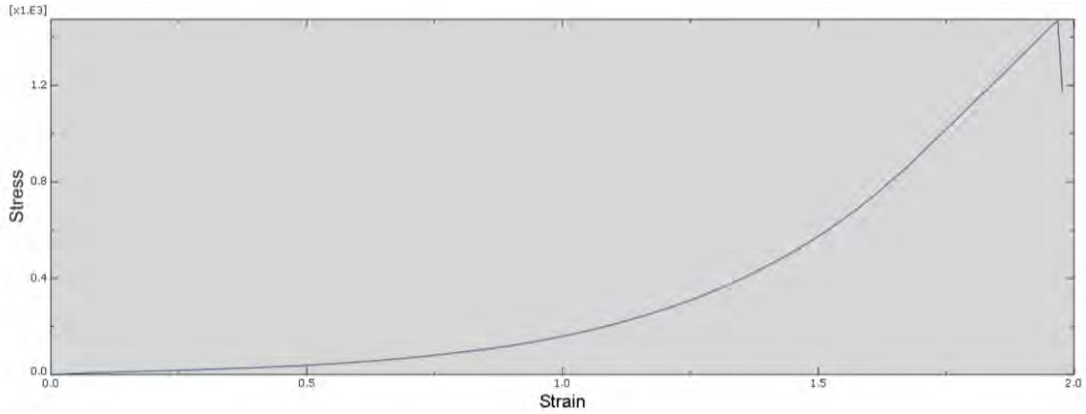
Figure 6.12 True stress - strain data of Ni and B added Al 7075

6.9 Data Input Methodology

To input data in Abaqus, a property module was at first selected as shown in figure 6.13. For each alloy a profile was created in the material manager section. In each profile the experimental data listed in section 6.8 for each alloy was added to perform the simulation.
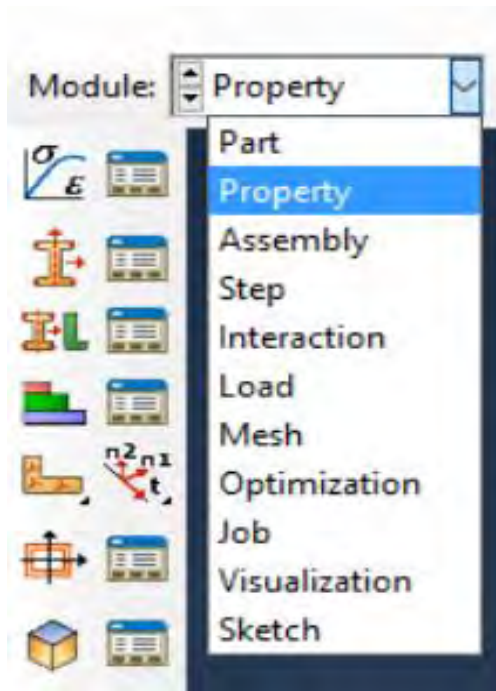
Figure 6.13 Property module selection in Abaqus 6.14.

Figure 6.14-6.19 shows how these data were given as input in Abaqus property module for different alloys. A consistent unit system was maintained during the input of the data since Abaqus do not have any own unit convention. In Abaqus, slope as young's modulus was given as input along with the selected experimental true stress-plastic strain data to replicate the actual test. The fracture strain and displacement at failure had to be calculated by trial and error until the simulation failure matches the experiment.

Figure 6.14 shows the elastic and plastic data input method for alloy 1 and figure 6.15 shows the ductile damage and density data for the same alloy.
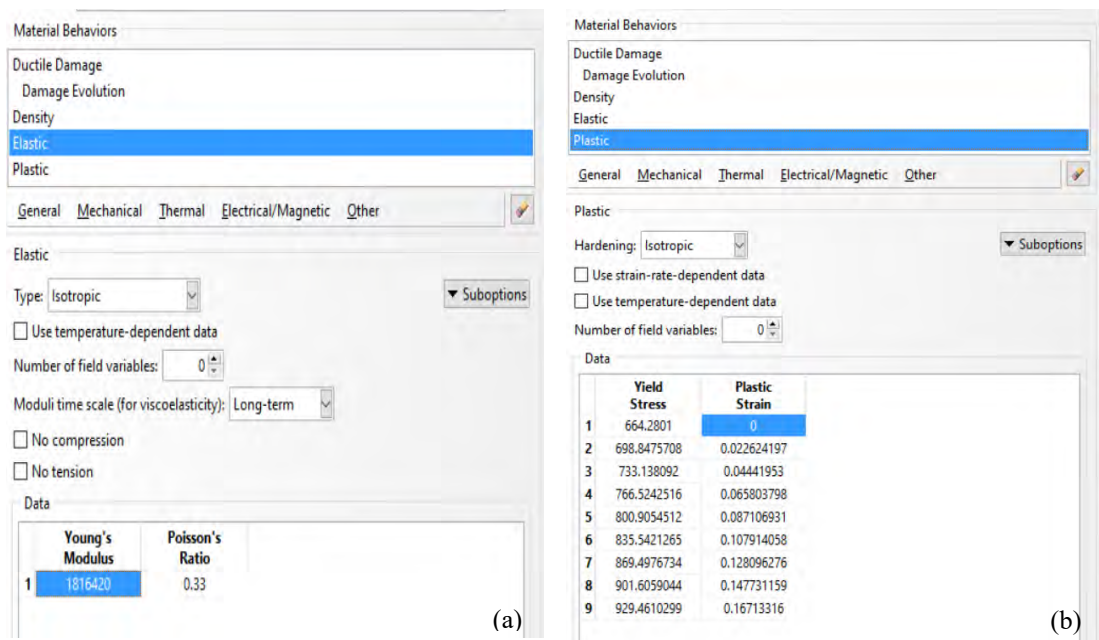
Figure 6.14 (a) Elastic and (b) Plastic data for alloy 1 .

(a)

(b)
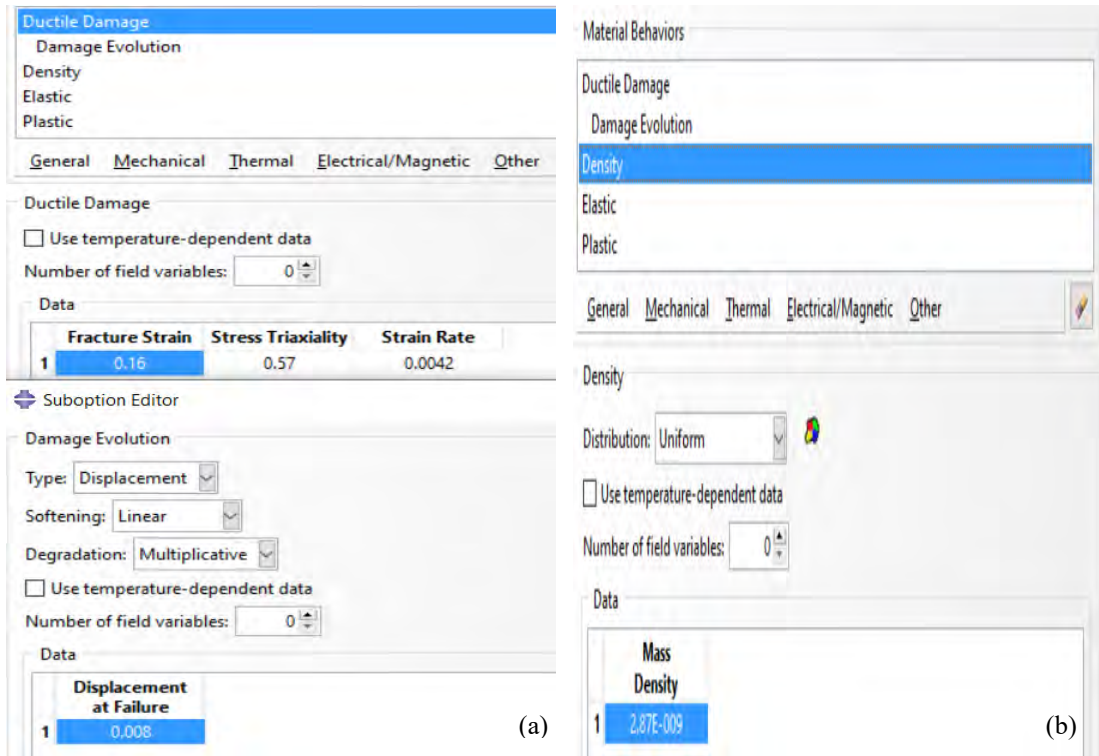
Figure 6.15 (a) Ductile damage data (b) Density data for alloy 1 .

Figure 6.16 shows the elastic and plastic material properties data and figure 6.17 shows the ductile damage data and the density data for alloy 2 (Ni added Al 7075).

(a)

(b)
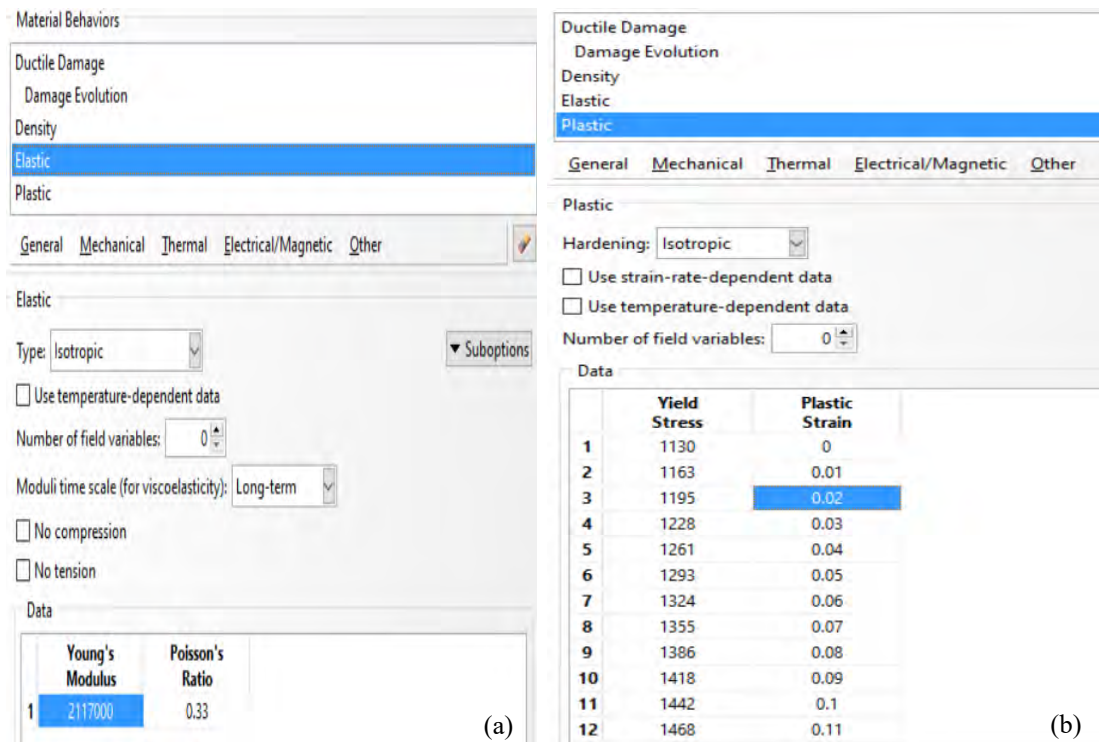
Figure 6.16 (a) Elastic and (b) Plastic data for alloy 2 .
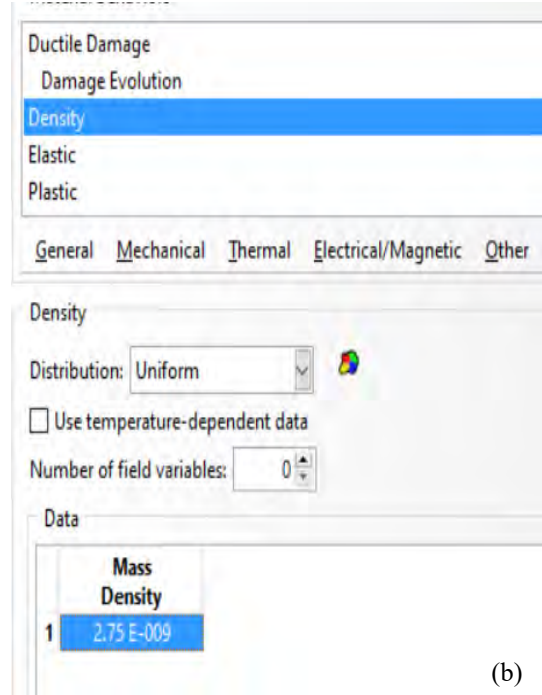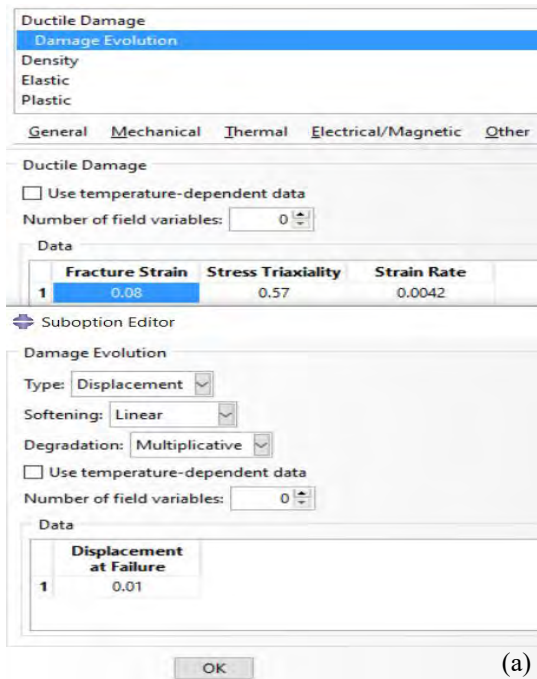
Figure 6.17 (a) Ductile damage data (b) Density data for alloy 2 .

Figure 6.18 shows the elastic and plastic material properties data and figure 6.19 shows the ductile damage data and the density data for alloy 3 (Ni and B added Al 7075).
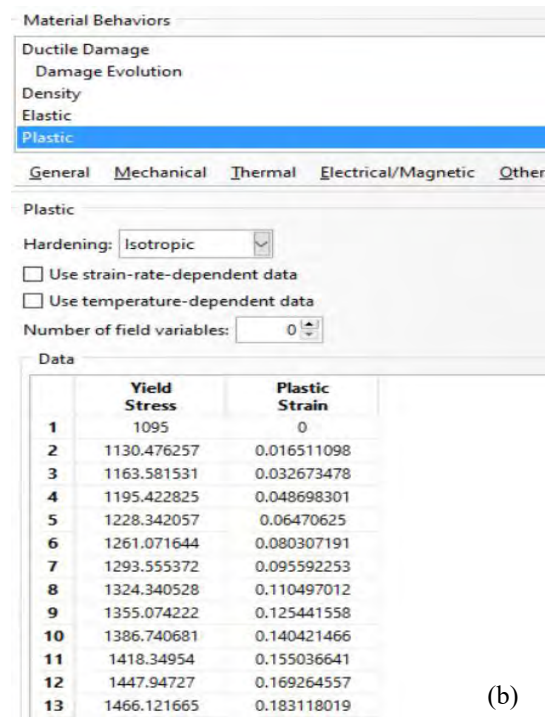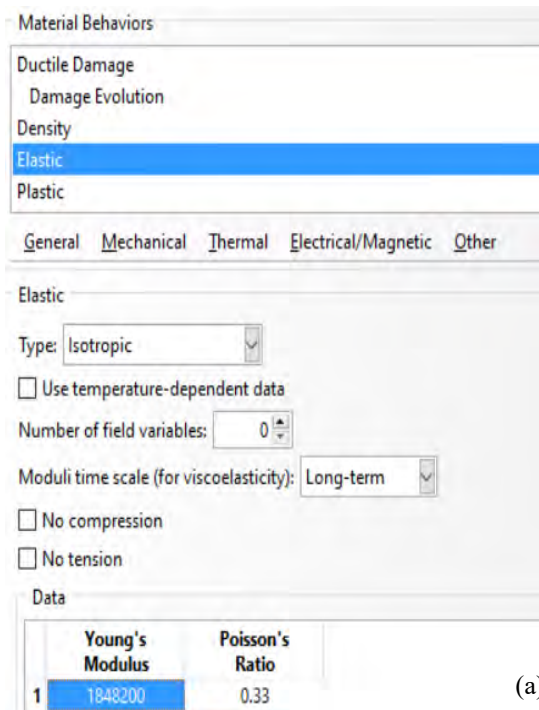
Figure 6.18 (a) Elastic and (b) Plastic data for alloy 3 .

(a)

(b)
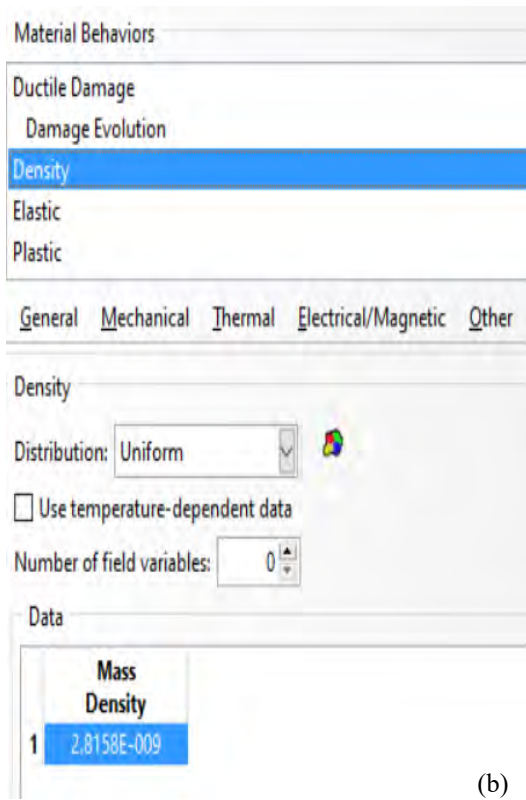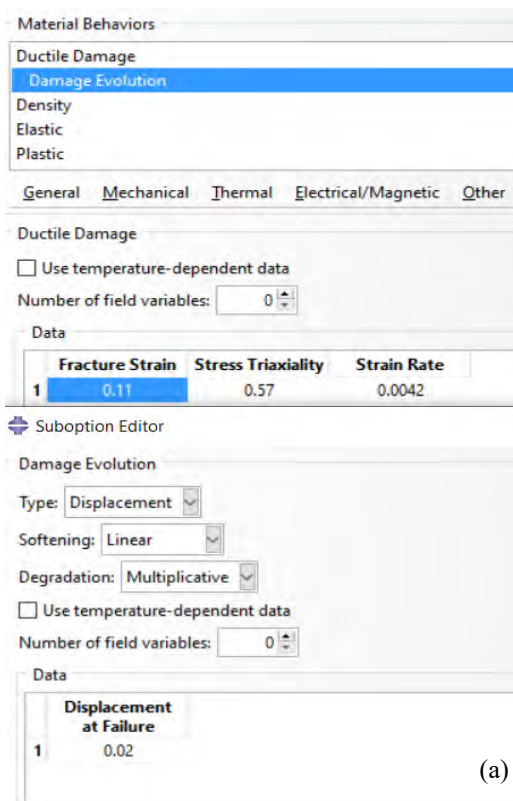
Figure 6.19 (a) Ductile damage data (b) Density data for alloy 3 .

CHAPTER 7 FEA Results

After models were created for each sample they were simulated trying to mimic the original test. Although variations were present but those simulations were not much deviated from original tests. Also, simulations were done with different mesh settings and observed with different output variables in the results that were obtained.

The damages in successive steps were dependent on DMICRT variable. DMICRT was calculated as a total of all damage variable parts that played in the damage in each element. In ductile damage mechanism it can be showed with the equation 7.1.

$$D = \int \bar{\omega}_D = \int \frac{d\epsilon^{pl}}{\epsilon_D^{pl}(\eta)} \tag{7.1}$$

If in this equation D is greater or equals to 1 for an element, then it means that the maximum degradation for that element is reached and it gets deleted from the mesh. This procedure is also known as the element deletion method.

In the results stress triaxiality output variables were asked in Abaqus result portion from the job output field in several important points. This is pointed in the figure 7.1. In each point stress triaxiality was plotted. From there the differences in various points were evaluated.
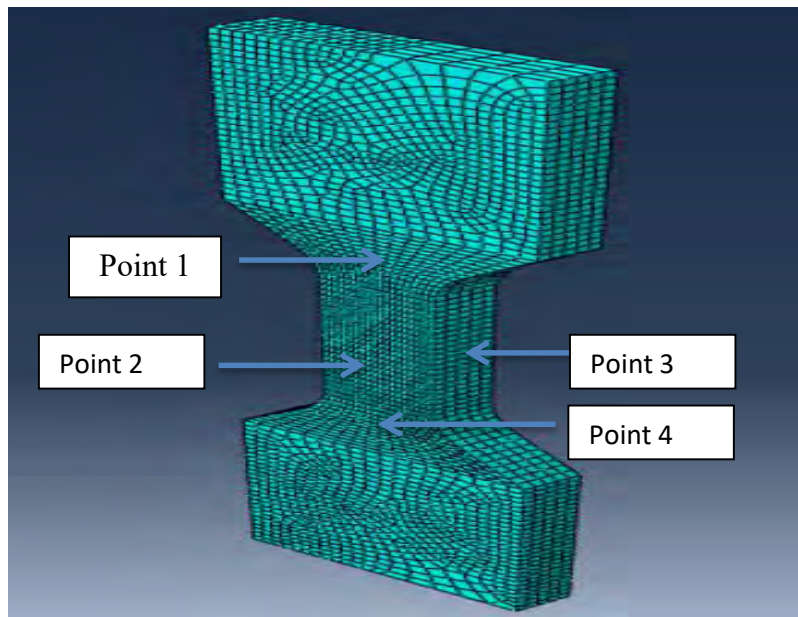
Figure 7.1 Showing the selected areas of the sample evaluated for stress triaxiality.

7.1 Element Quality Checks

Before using the mesh elements in the simulation it is important to check mesh quality of the elements in the model. Four different mesh sizes with two different mesh types were implemented. So, it would be sufficient to check the mesh quality of four different sizes in the model as the two eight node mesh types had same shape functions [114]. So, unlike mesh size, mesh types did not have any impact on mesh quality. Quality of the meshes was determined by using the shape metric element failure criteria limit. Table 7.1 shows the default element shape criteria limits set in Abaqus [105]. But many researchers ask for stricter selection criteria. So, our own selected criteria which are based on commonly used criteria also listed here. Any deviation of this selected criteria would result a yellow marking point on the mesh which is of bad quality.

Table 7.1 Default element shape selection criteria limits

Selection criterion	Quadrilateral	Triangle	Hexahedra	Tetrahedra	Wedge	Selected criteria(Hexahedra)
Shape factor	N/A	0.01	N/A	0.0001	N/A	**N/A**
Smaller face corner angle	10	5	10	5	10	**30**
Larger face corner angle	160	170	160	170	160	**150**
Aspect ratio	10	10	10	10	10	**5**

Since our elements were hexahedral, shape factor selection criterion was not applicable to it. The three selection criteria used in this thesis for the quality check were aspect ratio, smaller face corner angle, larger face corner angle. They are defined below:

Aspect Ratio:

Aspect ratio is the ratio between the longest and shortest edge of an element [100].

Smaller face corner angle

Defined as the elements where two edges meet at an angle smaller than a specified angle [105].

Larger face corner angle:

Defined as the elements where two edges meet at an angle larger than a specified angle [105].

7.1.1 Mesh Size 1.6

Aspect Ratio:

- ➢ Aspect ratio > 5: 0 Elements.
- ➢ Average aspect ratio: 1.69.
- ➢ Worst aspect ratio: 2.34.

Minimum angle on quad faces:

- ➢ Minimum angle < 30: 0 (0%).
- ➢ Average min angle on quad faces: 82.19.
- ➢ Worst min angle on quad faces: 45.

Maximum angle on quad faces:

- ➢ Maximum angle> 150: 0 (0%).
- ➢ Average max angle on quad faces: 97.81.
- ➢ Worst max angle on quad faces: 135.
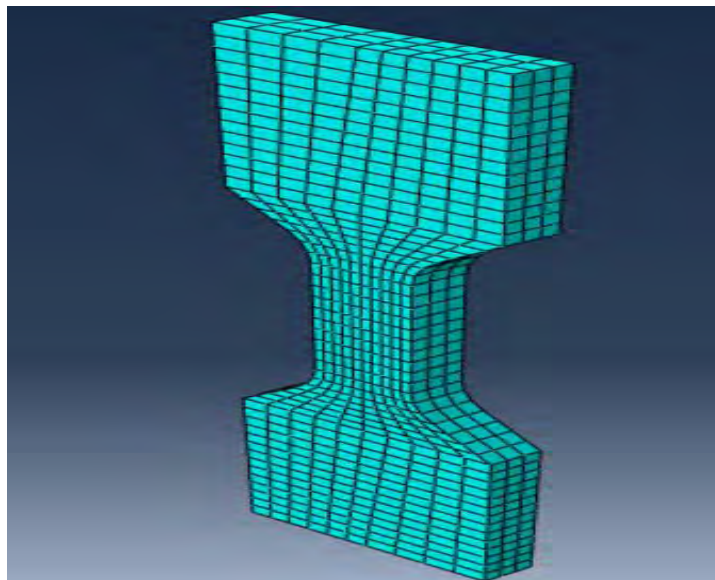
Figure 7.2 Quality of mesh elements in 1.6 mesh sizes.

7.1.2 Mesh Size 1.2

Aspect ratio:

- ➢ Aspect Ratio > 5: 0.
- ➢ Average aspect ratio: 1.63.
- ➢ Worst aspect ratio: 2.13.

Min angle on quad Faces:

- ➢ Minimum angle < 30: 0 (0%).
- ➢ Average min angle on quad faces: 81.64.
- ➢ Worst min angle on quad faces: 45.

Max angle on quad faces:

- ➢ Maximum angle > 150: 0 (0%).
- ➢ Average max angle on quad faces: 98.36.
- ➢ Worst max angle on quad faces: 135.

Figure 7.3 shows the elements with 1.2 mesh sizes. All the elements conformed with the mesh criteria.
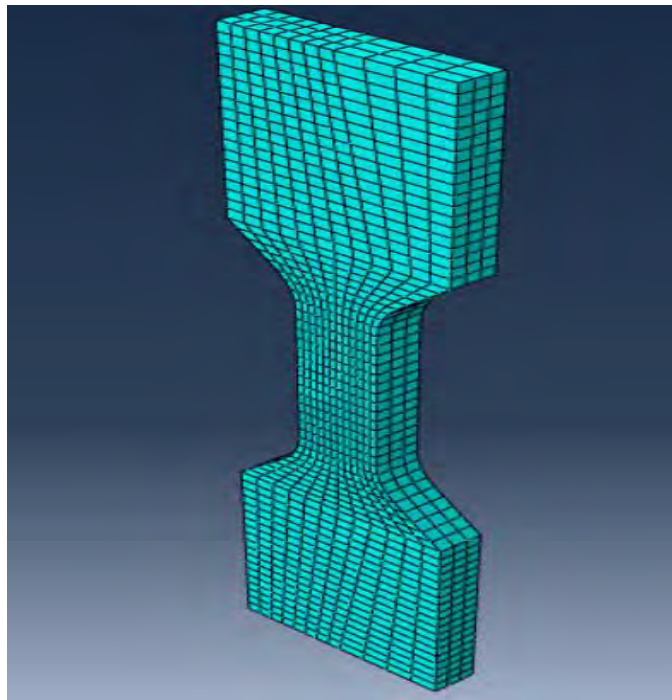
Figure 7.3 Quality of mesh elements in 1.2 mesh sizes.

7.1.3 Mesh Size 0.8

Aspect ratio:

- ➤ Aspect ratio > 5: 0 (0%).
- ➤ Average aspect ratio: 1.46.
- ➤ Worst aspect ratio: 2.5.

Min angle on quad faces:

- ➤ Minimum angle < 30: 0 (0%).
- ➤ Average min angle on quad faces: 79.59.
- ➤ Worst min angle on quad faces: 45.

Max angle on quad faces

- ➤ Maximum angle> 150: 0 (0%).
- ➤ Average max angle on quad faces: 100.76.
- ➤ Worst max angle on quad faces: 135.

All of the elements in the mesh conformed with the required selection criteria.
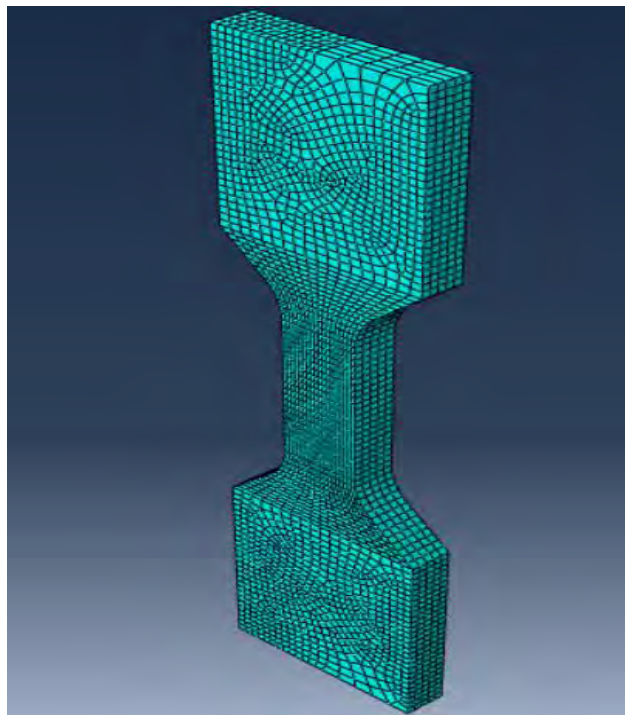
Figure 7.4 Quality of mesh elements with 0.8 mesh sizes.

7.1.4 Mesh Size 0.4

Aspect ratio:

- ➢ Aspect ratio > 5: 0 (0%).
- ➢ Average aspect ratio: 1.47.
- ➢ Worst aspect ratio: 3.37.

Min angle on quad faces:

- ➢ Minimum angle < 30: 0 (0%).
- ➢ Average min angle on quad faces: 81.04.
- ➢ Worst min angle on quad faces: 36.57.

Max angle on quad faces:

- ➢ Maximum angle > 150: 0 (0%).
- ➢ Average max angle on quad faces: 99.93.
- ➢ Worst max angle on quad faces: 137.

All of the elements in the mesh conformed with the required selection criteria.
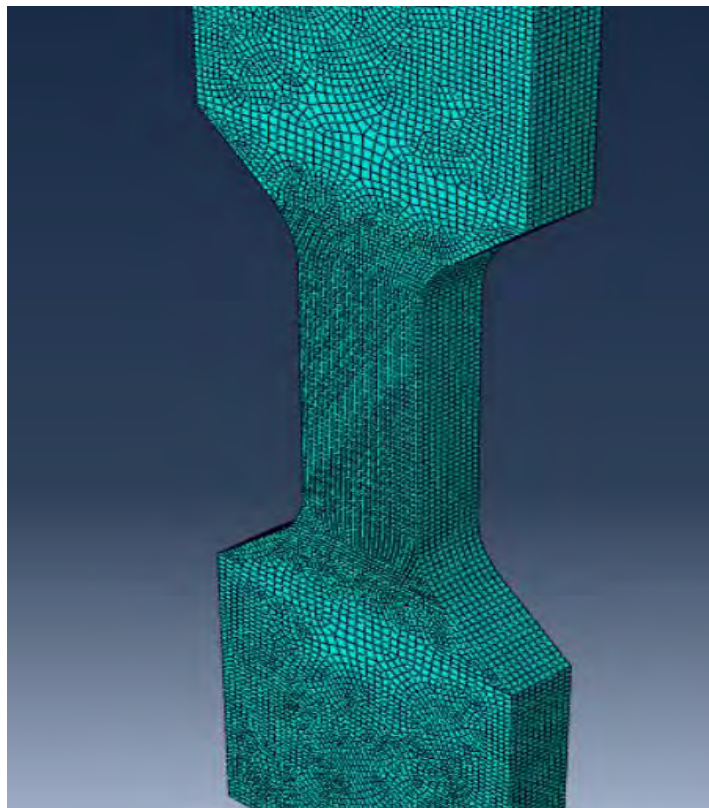
Figure 7.5 Quality of mesh elements with 0.4 mesh sizes.

All of these element sizes were well into the limits of the selection criteria. Still, as the mesh sizes became finer the aspect ratio became better. As seen from the figure 7.6 the aspect ratio became better as the element sizes decreased. The aspect ratio became almost constant after 0.8 mesh sizes. And the average minimum angle and the average maximum angles were nearly constant for every mesh sizes [105].
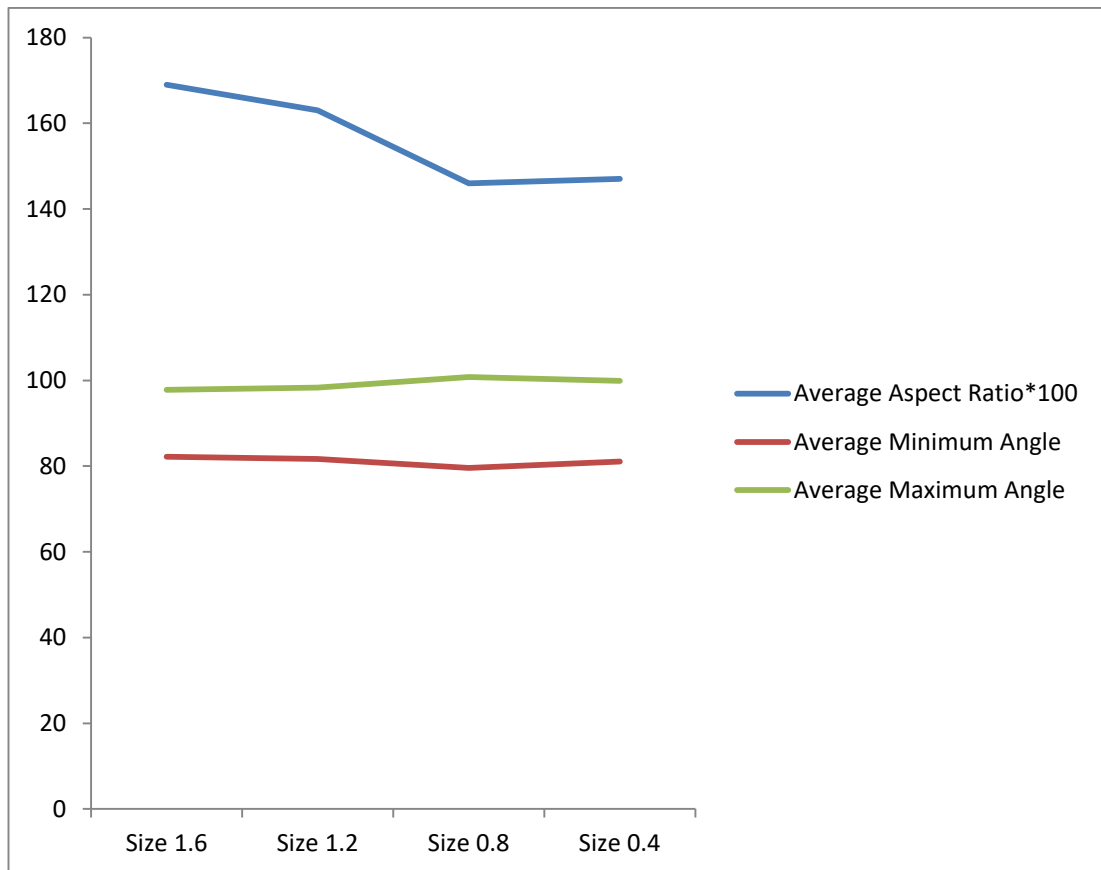
Figure 7.6 Changes in aspect ratio, minimum angle, and maximum angle as the mesh element size changes.

7.2 Aluminium 7075 FEA Results

7.2.1 Mesh Element Size 1.6

In the simulation runs with 1.6 mesh sizes two different mesh types were used namely C3D8 and C3D8R. In figure 7.7 It was found that the damage failure by gradual stiffness reduction happened for C3D8 mesh types a bit different than the C3D8R mesh types. The difference mainly happened due to the fact that C3D8R uses center of the cube as a point of integration whereas C3D8 used 2*2*2 integration [111, 114].

Figure 7.7 Aluminium 7075 progressive damage failure with 1.6 size mesh elements (a) C3D8 mesh type (b) C3D8R mesh type.

Also, time required for the simulation was greater in the C3D8 mesh types because of higher number of integration points which is apparent from table 7.2.

Table 7.2 Obtained results with mesh type C3D8 and C3D8R for 1.6 mesh size.

Mesh type	Number of elements	Number of nodes	Increment	CPU time(s)
C3D8	3360	5096	391186	2539.9
C3D8R	3360	5096	391186	758.1

7.2.2 Mesh Element Size 1.2

Figure 7.8 shows the fractography with 1.2 element sizes in both C3D8 and C3D8R mesh type. The fracture occurred more or less in the same place but the fractography was a bit different. C3D8 showed more ductile failure than its counterpart. Failure was somewhat uniform in the C3D8 mesh elements, but C3D8R did not have smooth failure surface like C3D8 mesh types. And as before, time required for C3D8 elements were much greater.

Figure 7.8 Aluminium 7075 progressive damage failure with 1.2 size mesh elements (a) C3D8 mesh type (b) C3D8R mesh type.

Table 7.3 Obtained results with mesh type C3D8 and C3D8R for 1.2 mesh size.

Mesh type	Number of elements	Number of nodes	Increment	CPU time(s)
C3D8	5820	8568	391393	4510
C3D8R	5820	8568	391393	1229.6

7.2.3 Mesh Element size 0.8

In the mesh element size 0.8 the failure pattern started become quite similar to experimental fracture. In figure 7.9(a) C3D8 element showed ductile failure pattern as it was in the experiment. Whereas, in figure 7.9(b) the failure in C3D8R element showed brittle fracture opposite to the experimental fracture. Also, the time required to run the simulation also had increased exponentially.

Figure 7.9 Aluminium 7075 progressive damage failure with 0.8 size mesh elements (a) C3D8 mesh type (b) C3D8R mesh type.

Mesh type	Number of elements	Number of nodes	Increment	CPU time(s)
C3D8	21420	27528	745783	29199
C3D8R	21420	27528	745783	8502.4

7.2.4 Mesh element size 0.4

In figure 7.10(a) C3D8 mesh type created a fine distribution of ductile fracture pattern in the simulation result. On the other hand, in figure 7.10(b) C3D8R failed in a ductile-brittle manner. Both created a failure pattern that can be described as cup and cone failure, as seen from table 7.5 the time required for 0.4 mesh size increased exponentially thus making C3D8 simulation much time consuming.

Figure 7.10 Aluminium 7075 progressive damage failure with 0.4 size mesh elements (a) C3D8 mesh type (b) C3D8R mesh type.

Table 7.5 Obtained results with mesh type C3D8 and C3D8R for 0.4 mesh size.

Mesh type	Number of elements	Number of nodes	Increment	CPU time(s)
C3D8	173660	197604	605384	316484
C3D8R	173660	197604	605384	59016

7.2.5 Real Samples and Simulated Results

To compare between the real samples and the simulation results, they are grouped in figure 7.11. From the figure it is apparent that simulation having C3D8 mesh type and 0.4 mesh sizes in figure 7.11(c) had finer fracture surface like a true cup and cone failure. This cup and cone failure was not observed in the experiment. Also, from the microstructure and EDS it was found that there were Al-Cu-Mg intermetallics formed in the sample which generally induces somewhat brittle failure [115, 116]. So, pure ductile failure did not happen in the experiment because of chances but this kind of fracture was expected from the microstructural point of view. On the other hand, figure 7.11(b) and 7.11(d) had similar results like experimental failure of Al 7075 sample. But if the time for computations are considered then C3D8 mesh type with 0.8 mesh sizes (29199 CPU time) become the better candidate than the C3D8R mesh type with 0.4 mesh sizes (59016 CPU time).

Figure 7.11 Progressive damage failure of (a) Real sample (b) C3D8 with 0.8 mesh size (c) C3D8 with 0.4 mesh size and (d) C3D8R with 0.4 mesh size.

7.3 Ni Added Aluminium 7075 FEA Results

7.3.1 Mesh Element Size 1.6

C3D8 and C3D8R mesh types were used in Ni added Al 7075 tensile sample. Figure 7.12(a) showed nearly a ductile failure but its relatively coarse element did not allow the simulation results to obtain the failure detail which is mandatory in a simulation. Figure 7.12(b) with C3D8R element also did not show any definite fracture pattern.

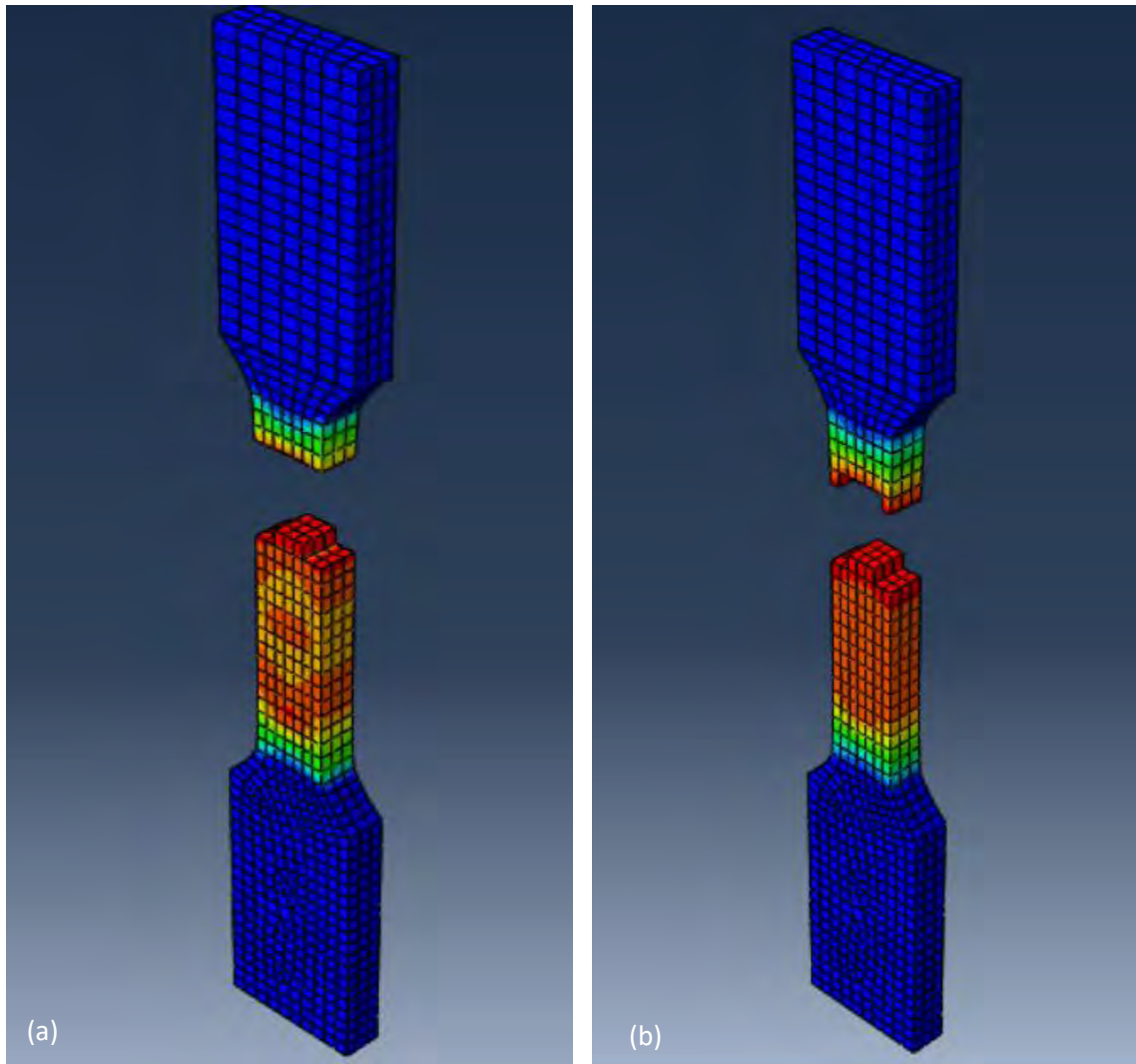**Figure 7.12 Ni added Aluminium 7075 progressive damage failure with 1.6 size mesh elements (a) C3D8 mesh type (b) C3D8R mesh type.**

Table 7.6 Obtained results with mesh type C3D8 and C3D8R for 1.6 mesh size.

Mesh type	Number of elements	Number of nodes	Increment	CPU time(s)
C3D8	3360	5096	429718	2908.2
C3D8R	3360	5096	429718	833.7

7.3.2 Mesh Element Size 1.2

In figure 7.13 point of failure remained in same region. Also, fractography of both sample maintained similar fashioned failure. CPU time increased due to higher number of variables arising from higher number of elements consequently higher number of nodes.
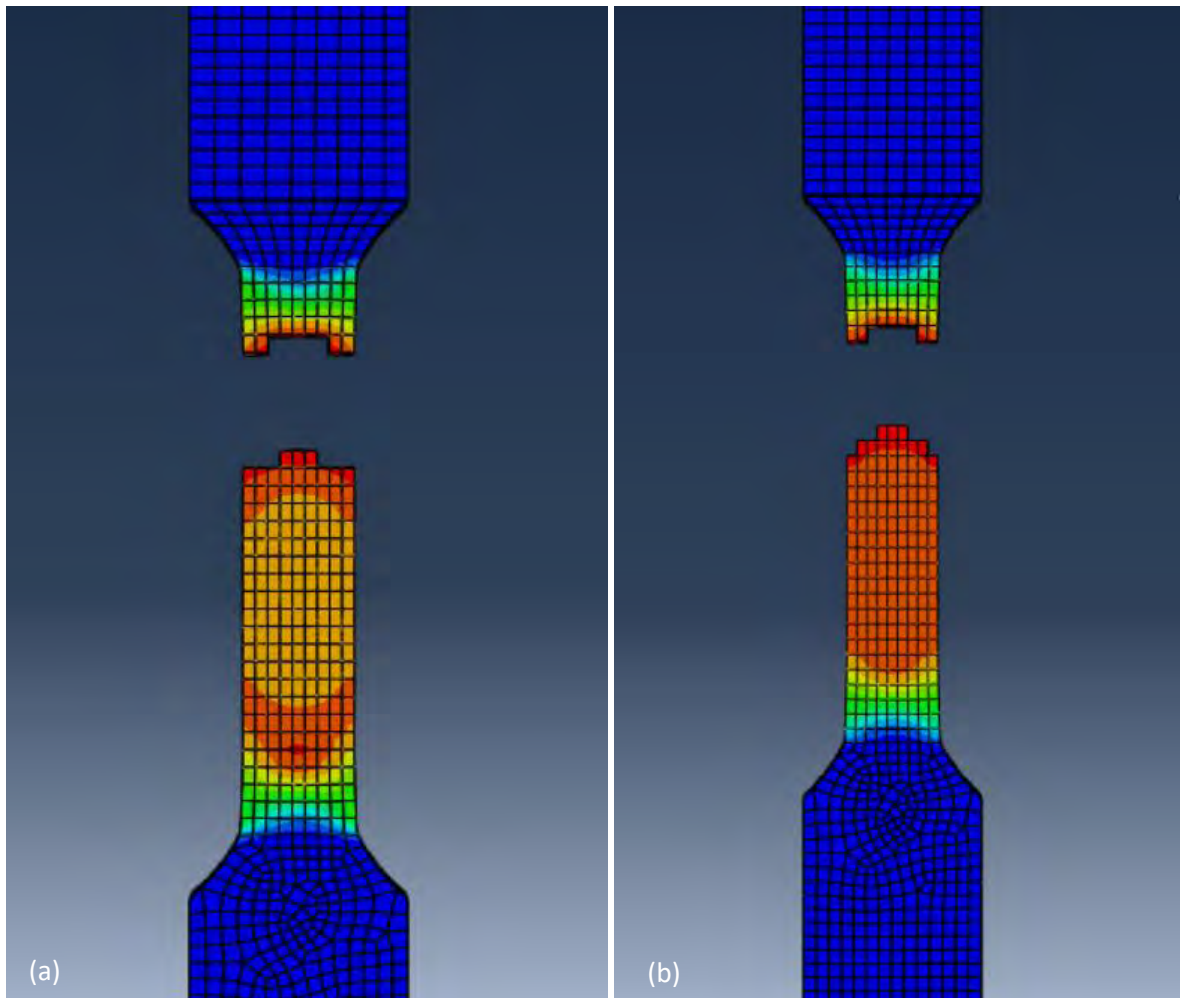

Figure 7.13 Ni added Aluminium 7075 progressive damage failure with 1.2 size mesh elements (a) C3D8 mesh type (b) C3D8R mesh type.

Table 7.7 Obtained results with mesh type C3D8 and C3D8R for 1.2 mesh size.

Mesh type	Number of elements	Number of nodes	Increment	CPU time(s)
C3D8	5820	8568	432081	5000.5
C3D8R	5820	8568	432081	1241

7.3.3 Mesh Element Size 0.8

Fractography in figure 7.14(a) and (b) were quite similar to the experimental fracture. Both of these simulations showed similar point of failure and failed in a bit ductile manner as same as the sample failed in the experiment. But as showed in table 7.8 simulation time for both of the simulations increased exponentially.

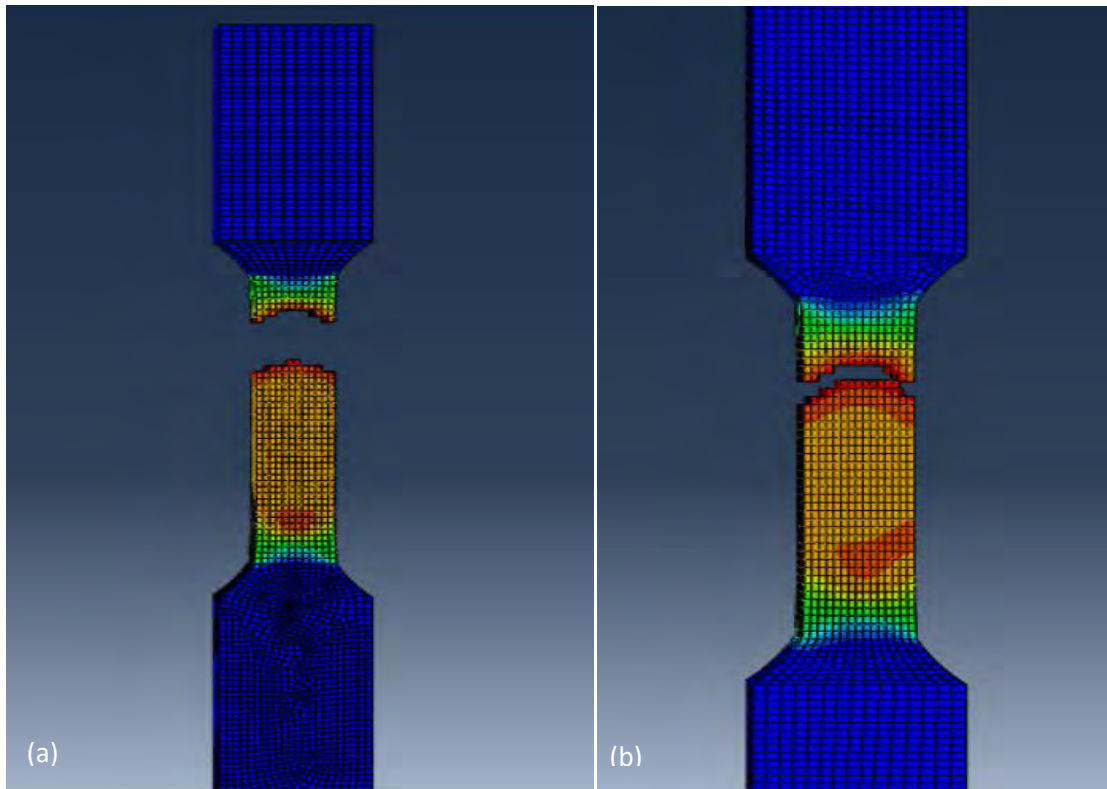**Figure 7.14 Ni added Aluminium 7075 progressive damage failure with 0.8 size mesh elements (a) C3D8 mesh type (b) C3D8R mesh type.**

Table 7.8 Obtained results with mesh type C3D8 and C3D8R for 0.8 mesh size.

Mesh type	Number of elements	Number of nodes	Increment	CPU time(s)
C3D8	20930	26928	437344	19570.19
C3D8R	20930	26928	437344	5368.8

7.3.4 Mesh Element Size 0.4

In figure 7.15(b) C3D8R had the fractography and failure place as same as the original one but in figure 7.15(a) C3D8 model did not fail properly due to shear locking that normally occurs in these mesh types [105].
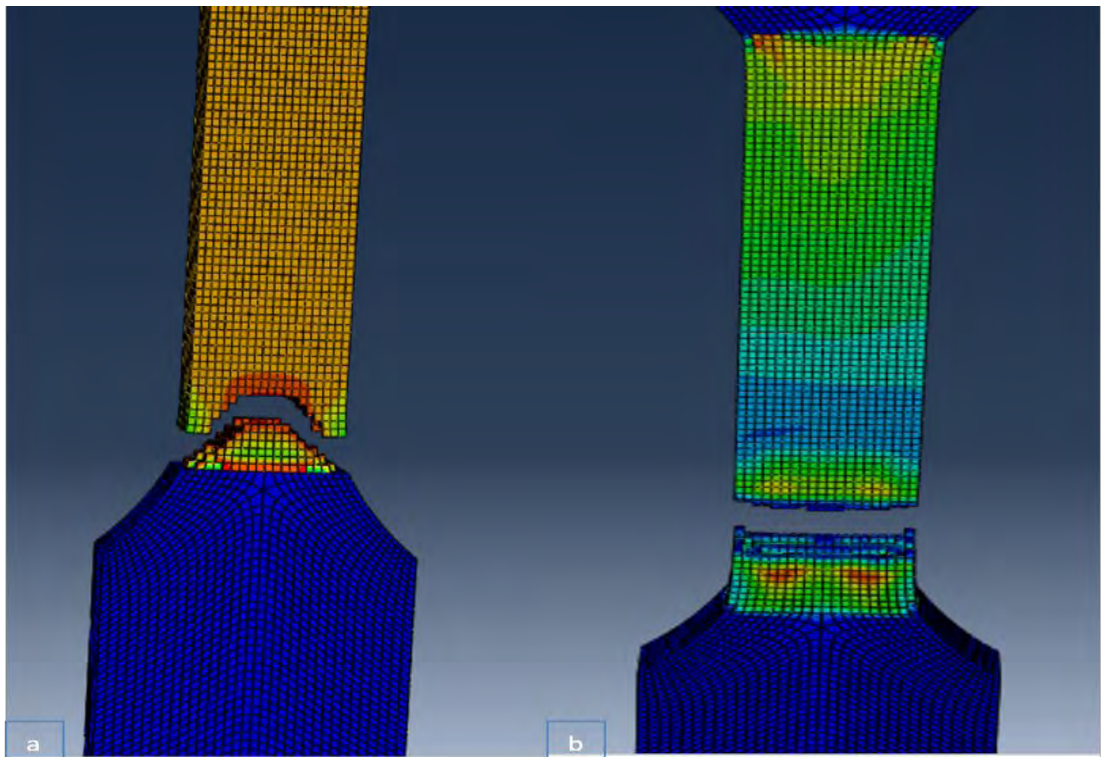

Figure 7.15 Ni added Aluminium 7075 progressive damage failure with 0.4 size mesh elements (a) C3D8 mesh type (b) C3D8R mesh type.

Table 7.9 Obtained results with mesh type C3D8 and C3D8R for 0.4 mesh size.

Mesh type	Number of elements	Number of nodes	Increment	CPU time(s)
C3D8	173660	197604	Shear locked	Shear locked
C3D8R	173660	197604	605384	58745.7

7.3.5 Real Samples and Simulated Results

Real sample and simulated results from C3D8 mesh type with 0.4 and 0.8 mesh sizes and simulated results from C3D8R mesh type with 0.4 mesh size are presented together in figure 7.16. Among them C3D8 mesh type with 0.8 mesh sizes and C3D8R mesh type with 0.4 mesh sizes had failed in a bit ductile manner similar to the experimental fracture. C3D8 mesh type with 0.4 mesh sizes also showed similarities at the beginning of the fracture but could not finish the fracture as it got shear locked. All of the failure pattern shown in figure 7.16 where aluminium lost some of its ductility agrees with the microstructure of the alloy. Aluminium is a ductile metal but presence of alloying elements in Ni added Al 7075 created phases like η phase ($MgZn_2$) and Al-Cu-Ni phase. These phases in turn decrease the ductility by increasing strength and hence fracture surface was found like figure 7.16 [115, 117]. In the simulation of Ni added Aluminium 7075 C3D8 mesh type with 0.8 mesh size and C3D8R mesh type with 0.4 mesh sizes showed agreeable results but if time required to complete simulation is taken in the consideration then the C3D8 mesh type with 0.8 mesh sizes gave the optimum result.
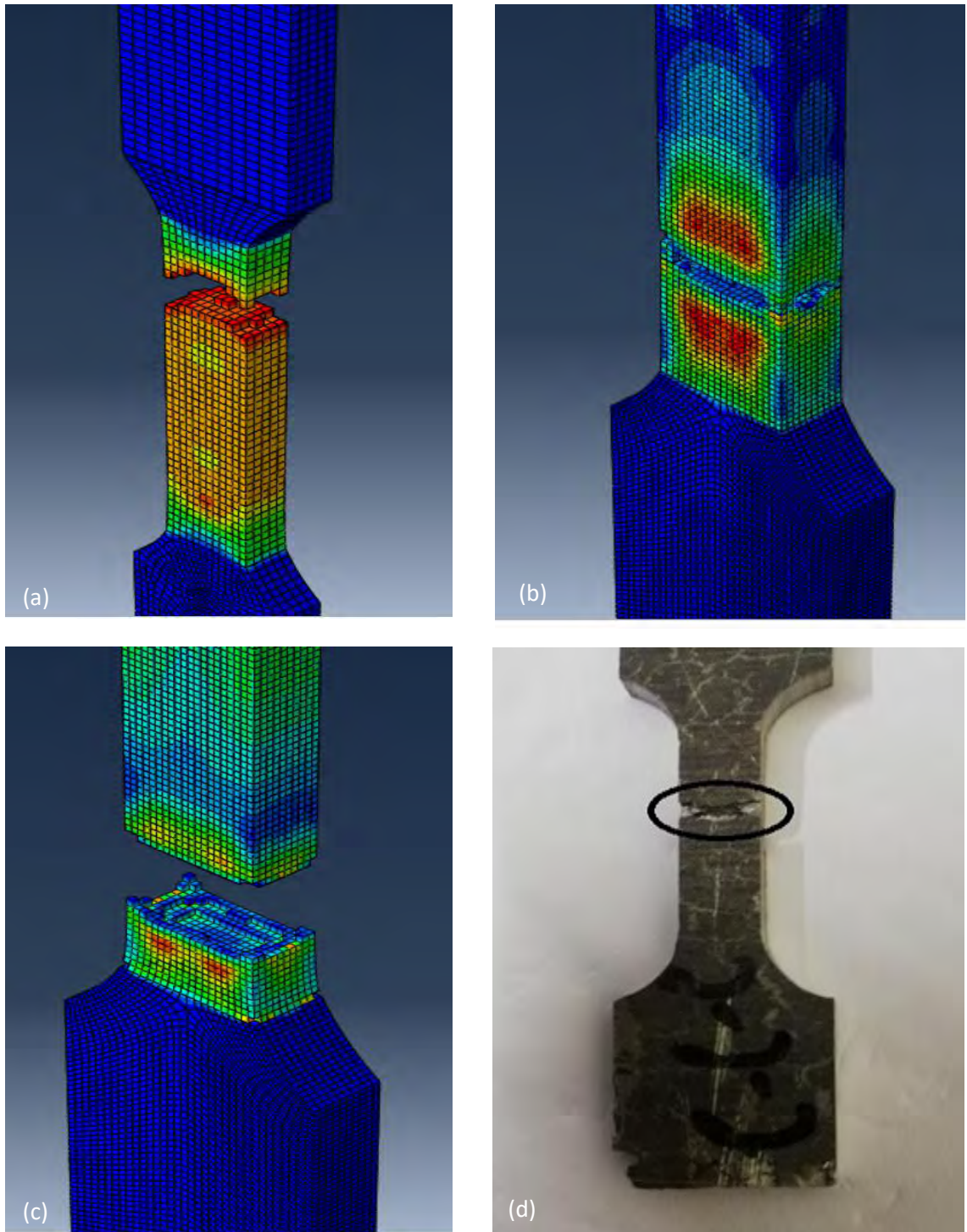
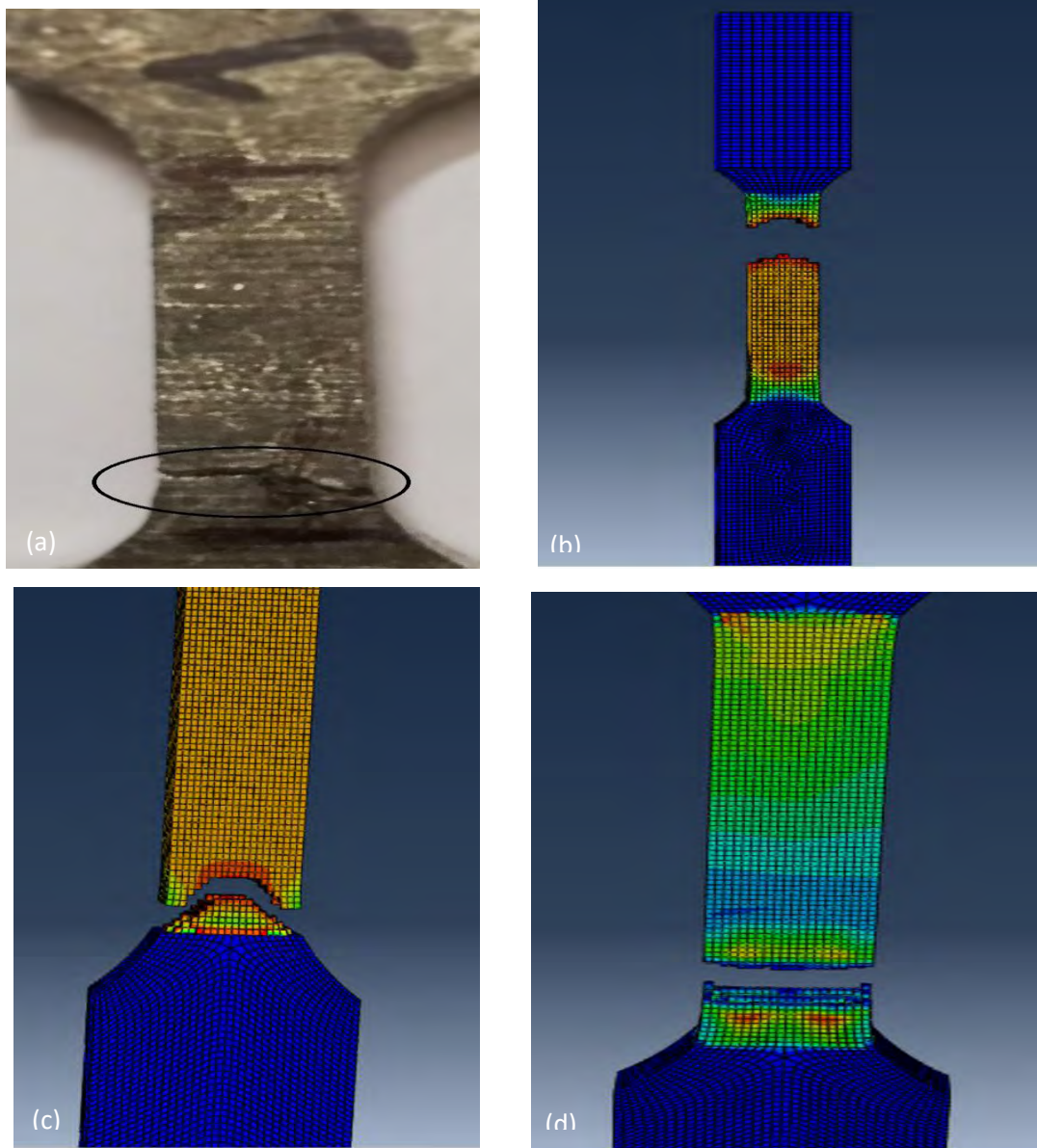**Figure 7.16 Progressive damage failure of (a) C3D8 sample with 0.8 mesh sizes (b) C3D8 with 0.4 mesh size (c) C3D8R with 0.4 mesh size and (d) Real Sample.**

7.4 Nickel and Boron Added Al 7075 FEA Results

7.4.1 Mesh Element size 1.6

C3D8 mesh type with 1.6 mesh sizes in figure 7.17(a) and C3D8R mesh type with 1.6 mesh sizes in figure 7.17(b) both showed inability to depict any ductile failure which had happened in the experiment. Thus both simulation results were not agreeable to the real test.
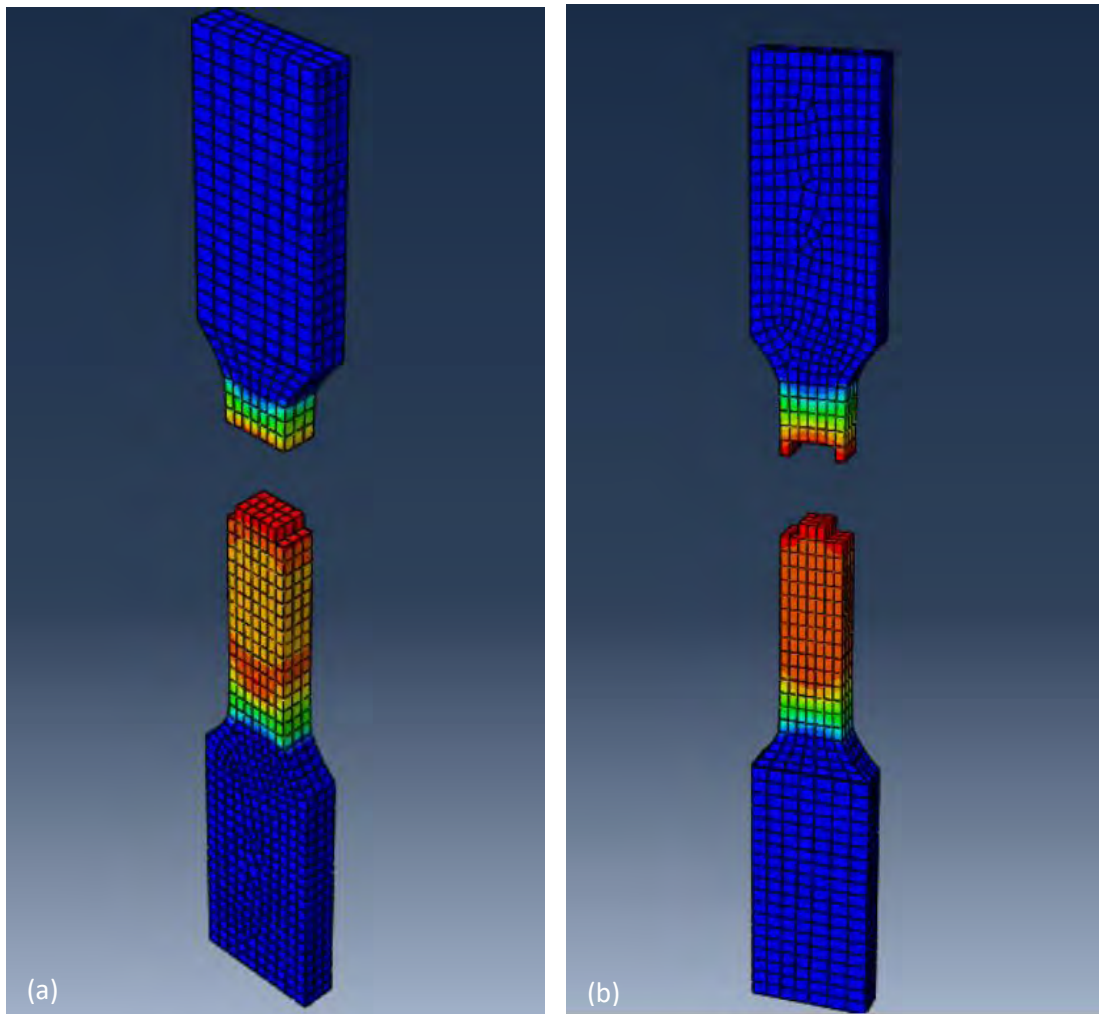

Figure 7.17 Ni and B added Aluminium 7075 progressive damage failure with 1.6 size mesh elements (a) C3D8 mesh type (b) C3D8R mesh type.

Table 7.10 Obtained results with mesh type C3D8 and C3D8R for 1.6 mesh size.

Mesh type	Number of elements	Number of nodes	Increment	CPU time(s)
C3D8	3246	4944	303329	1991.6
C3D8R	3246	4944	303329	619.2

7.4.2 Mesh Element Size 1.2

Figure 7.18(a) shows the simulation results obtained from C3D8 mesh type with 1.2 mesh sizes and figure 7.18(b) shows the results obtained from C3D8R mesh type with 1.2 mesh sizes. It is seen from these figure that both of these results partially mimicked the test which can be interpreted as these simulations started to conform with the experiment.
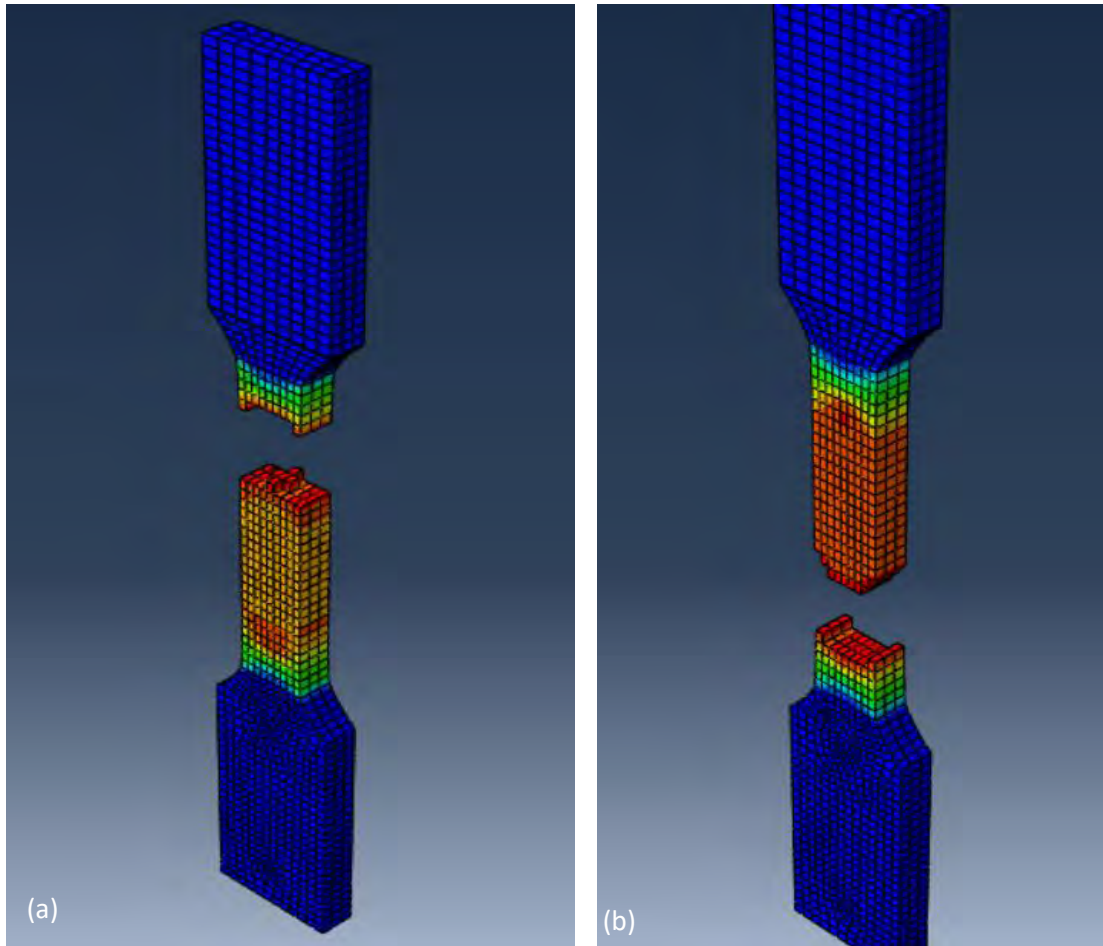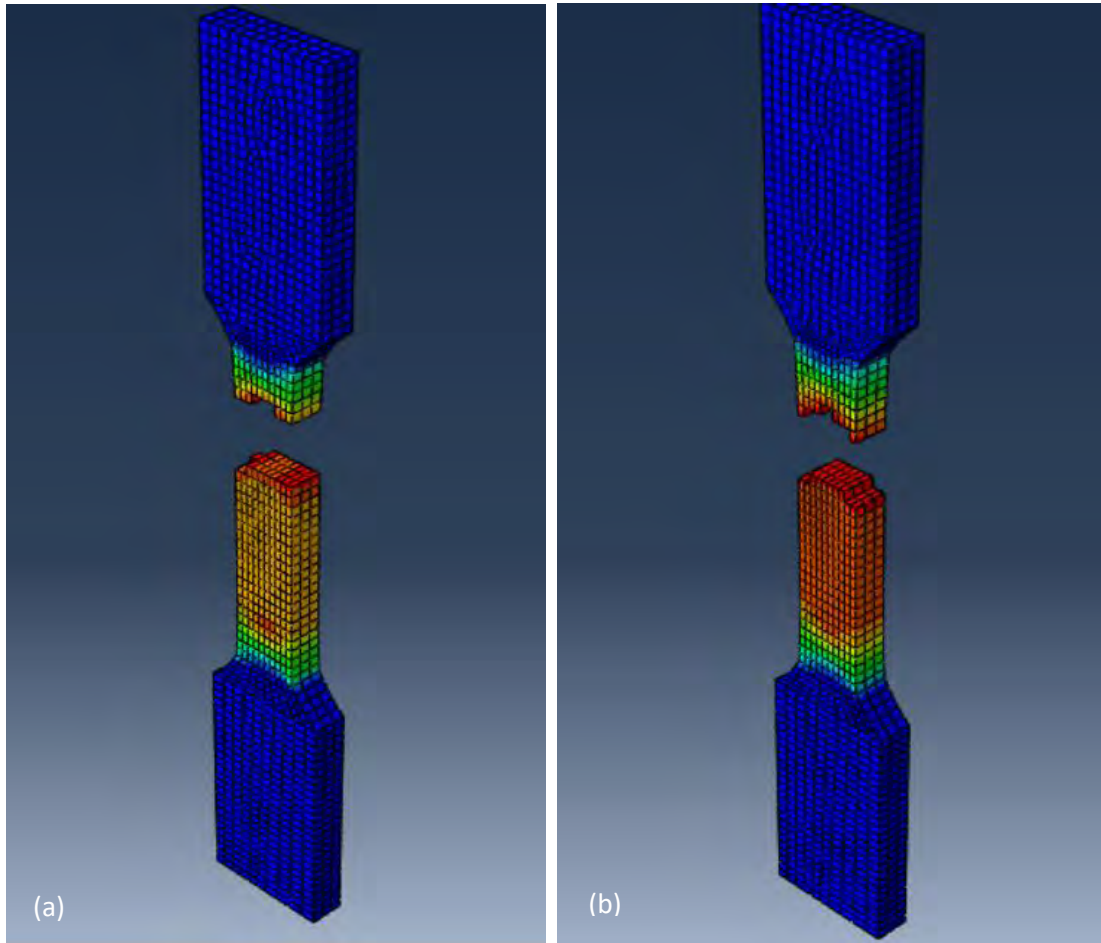

Figure 7.18 Ni and B added Aluminium 7075 progressive damage failure with 1.2 size mesh elements (a) C3D8 mesh type (b) C3D8R mesh type.

Table 7.11 Obtained results with mesh type C3D8 and C3D8R for 1.2 mesh size.

Mesh type	Number of elements	Number of nodes	Increment	CPU time(s)
C3D8	5988	8792	398264	5446.5
C3D8R	5988	8792	398264	1231.6

7.4.3 Mesh Element Size 0.8

Figure 7.19 shows simulation results with 0.8 mesh sizes with 7.19(a) C3D8 mesh type and 7.19(b) C3D8R mesh type. Unlike simulation results from 1.6 mesh sizes (figure 7.17) and 1.2 mesh sizes (figure 7.18) both of the C3D8 and C3D8R simulation result fractography and the point of failure showed convergence to the experimental fracture. But from table 7.10, 7.11 and 7.12 it is apparent that the simulation time also had increased much for both of the simulation.
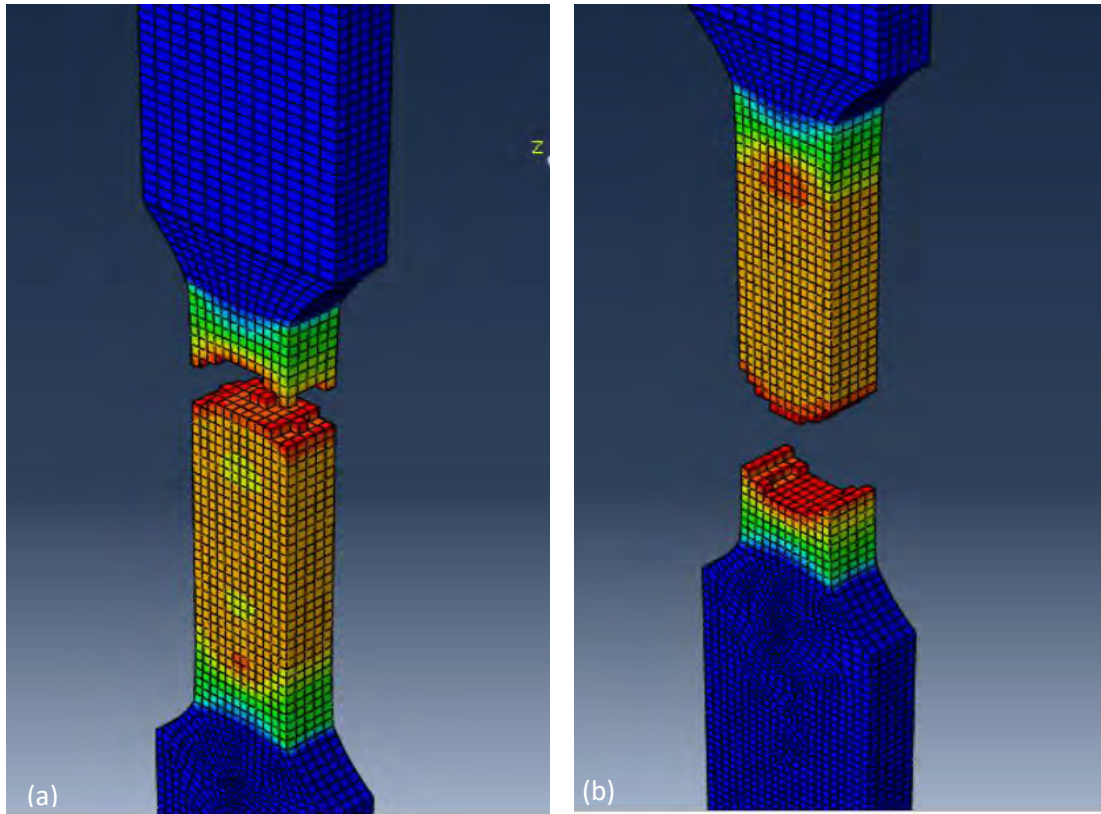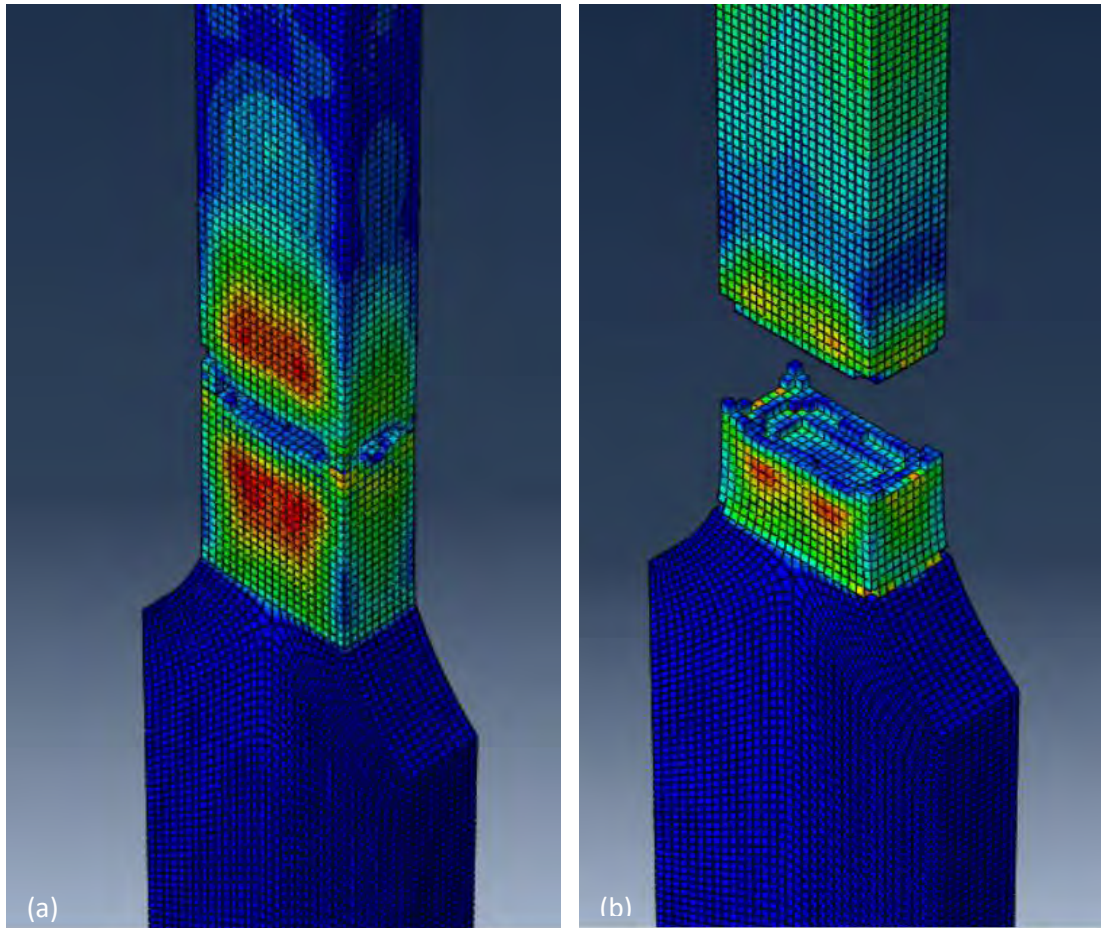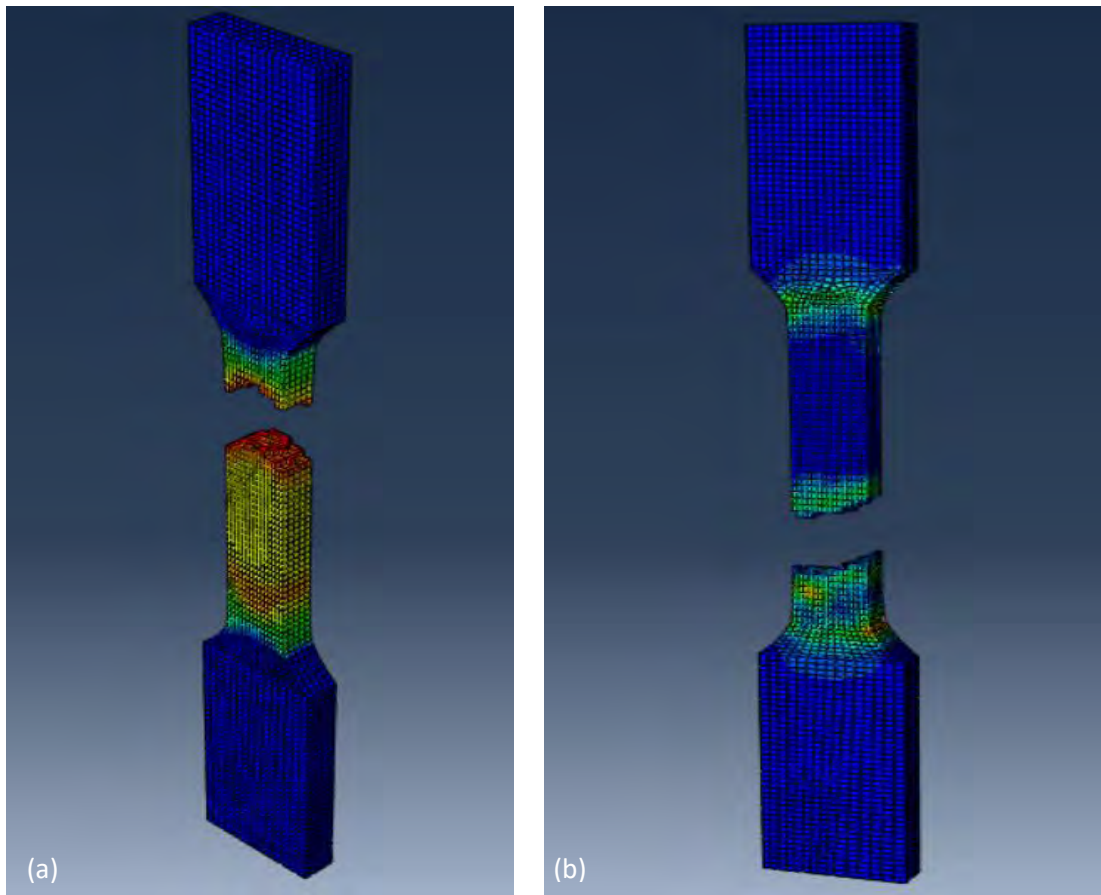

Figure 7.19 Ni and B added aluminium 7075 progressive damage failure with 0.8 size mesh elements (a) C3D8 mesh type (b) C3D8R mesh type.

Table 7.12 Obtained results with mesh type C3D8 and C3D8R for 0.8 mesh size.

Mesh type	Number of elements	Number of nodes	Increment	CPU time(s)
C3D8	21420	27528	756392	31046
C3D8R	21420	27528	756392	9748.27

7.4.4 Mesh Element Size 0.4

In figure 7.20 it is apparent that the simulation result of 0.4 mesh sizes with C3D8 mesh type elements in figure 7.20(a) were much fine and thus do not agree with experimental failure. On the other hand, the simulation result in figure 7.20(b) C3D8R was nearly same as compared to the experimental fracture scenario.
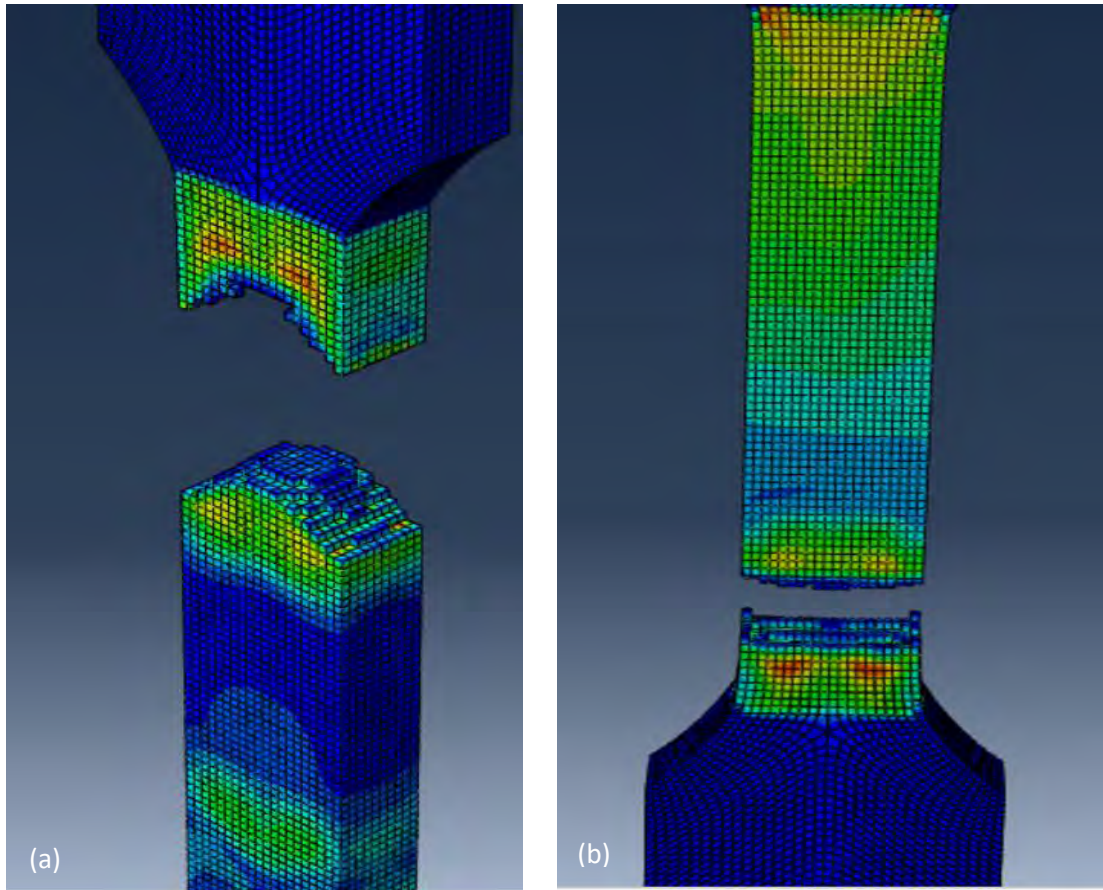
Figure 7.20 Ni and B added aluminium 7075 progressive damage failure with 0.4 size mesh elements (a) C3D8 mesh type (b) C3D8R mesh type.

Table 7.13 Obtained results with mesh type C3D8 and C3D8R for 0.4 mesh size.

Mesh type	Number of elements	Number of nodes	Increment	CPU time(s)
C3D8	84450	95623	994050	34206.4
C3D8R	84450	95623	994050	228468.86

7.4.5 Real sample and Simulated Results

Figure 7.21 represents the nearly matched solution in terms of fractography. Among them figure 7.21(d) C3D8R with 0.4 mesh size and figure 7.21(b) C3D8 with 0.8 mesh size were the near exact solution of the real problem while simulation result in figure 7.21(c) C3D8 with 0.4 mesh size took a large amount of time which discard the results practical validity. From the microstructure and EDS, it was found that there were Al-Cu-Ni intermetallics formed in the sample which generally induces somewhat brittle nature [115, 117]. Addition of boron seemed to have also increased strength but it did not affect ductility [42]. Thus, figure 7.21(d) C3D8R with 0.4 mesh size and figure 7.21(b) C3D8 with 0.8 mesh size shows result that mimics the test and fulfills theoretical assumption from the microstructure. Finally, among all the solutions C3D8 with 0.8 mesh had lowest computational time requirements. Thus making it the best choice.
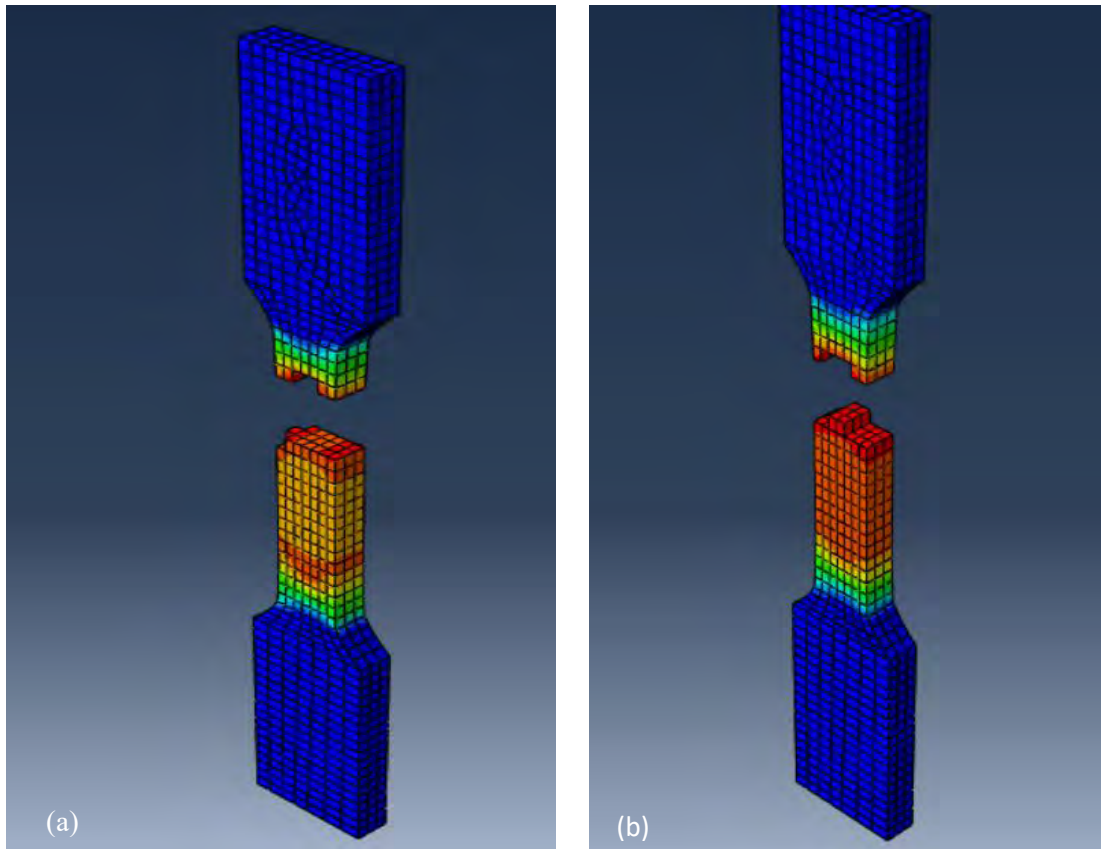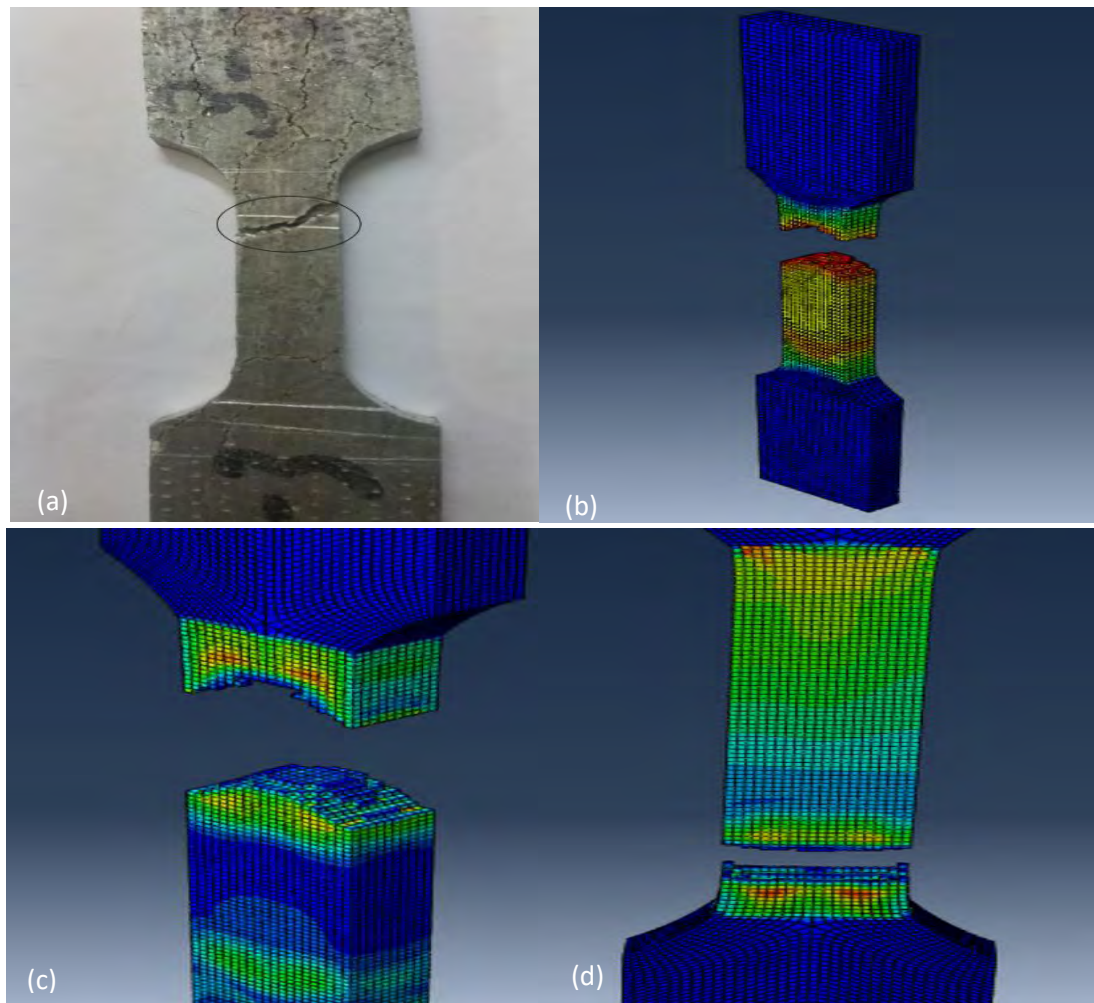

Figure 7.21 Progressive damage failure of (a) Real sample (b) C3D8 with 0.8 mesh size. (c) C3D8 with 0.4 mesh size and (d) C3D8R with 0.4 mesh size.

7.5 Parametric Study of Numerical Parameters

In any fracture simulation study, the stress triaxiality and the fracture strain relation is a very important one. Again, the cost of simulation directly depends on the time required for the simulation. The study of these parameters in relation to the real test and simulations thus demand high attention. Also, to be a successful simulation a simulation must conform to not only the shapes and place of failure but also the failure must occur in the same stress level as in the experiment. To understand these factors such as relation between mesh size and the time, stress triaxiality evolution during the test, the relation between the fracture strain and the failure stress at the time of fracture are explored.

7.5.1 Mesh size vs. Simulation Time

In each simulation runtime it was found that as the mesh size decreased, the time required to complete a simulation increased. Table 7.14 describes how required simulation time varied over the mesh sizes and the element type.

Table 7.14 Variation of CPU time with mesh type and mesh sizes.

Alloy	Mesh type	1.6 Mesh sizes(CPU time in s)	1.2 Mesh Sizes(CPU time in s)	0.8 Mesh Sizes(CPU time in s)	0.4 Mesh Sizes(CPU time in s)
Alloy 1	C3D8	2539.9	4510	29199	316484
	C3D8R	758.1	1229.6	8502.4	59016
Alloy 2	C3D8	2908.2	5000.5	19570.19	Shear locked
	C3D8R	833.7	1241	5368.8	58745.7
Alloy 3	C3D8	1991.6	5446.5	31046	228468.9
	C3D8R	619.2	1231.6	9478.27	34206.4

To plot these data into a graph average CPU time were calculated in table 7.15

Table 7.15 Average CPU time required.

Mesh type	Average time required in 1.6 mesh size (CPU time in s)	Average time required in 1.2 mesh size (CPU time in s)	Average time required in 0.8 mesh size (CPU time in s)	Average time required in 0.4 mesh size (CPU time in s)
C3D8	2479.9	4985.67	26605.06	272476.5
C3D8R	737	1234.07	7783.16	50656.03

Figure 7.22 shows simulation time dependencies with mesh sizes. It is apparent from figure 7.22 that the simulation time increased exponentially with decreasing mesh size but also the simulation quality became better with decreasing mesh size. So, it is actually a tradeoff between quality and the time required for simulation. Types of mesh also affects CPU time. For the case of this thesis C3D8 requires a lot more time than the C3D8R types. As discussed earlier in the section 5.4.4.10 the number of integration points were much less in the C3D8R type mesh than the C3D8 mesh types reflected at the number of nodes in the simulation data [111].
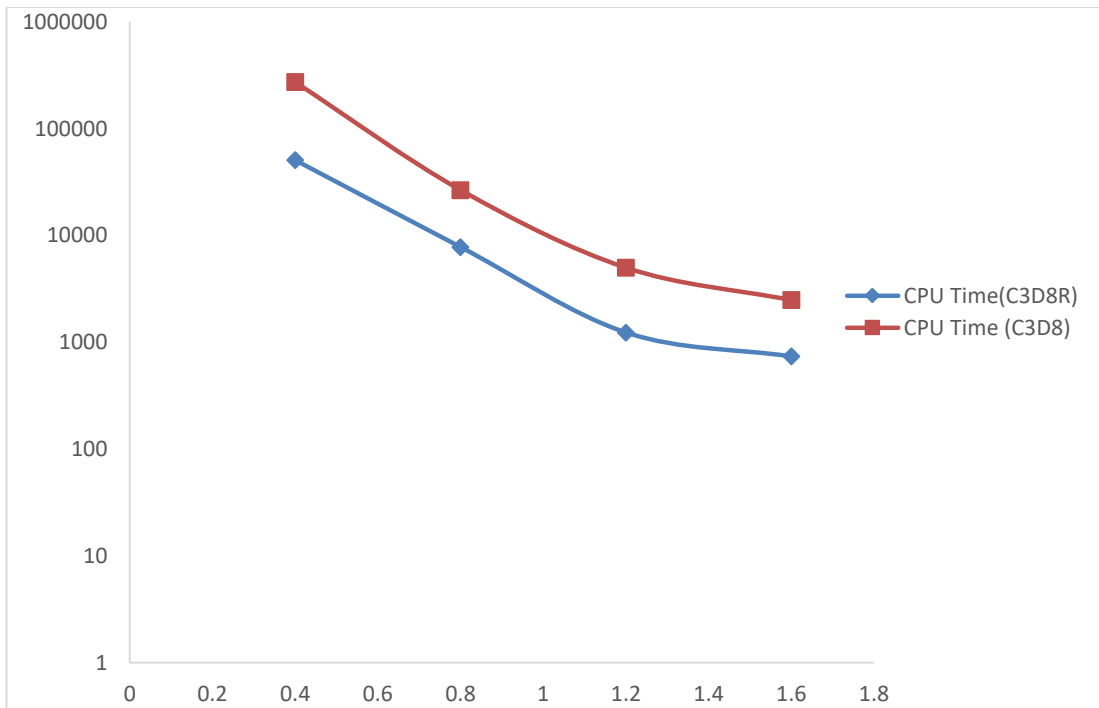
Figure 7.22 Mesh size Vs. log CPU time.

120

7.5.2 Evolution of Stress and Strain During Failure

Stress and strain parameters should be evaluated with the simulation results to verify that the output results in the simulation follows the input parameters. The inputs were in the true stress and plastic strain form and the outputs were in accordance with von Mises yield criterion [111]. This von Mises criterion is defined by

$$\frac{1}{6}[(\sigma_1 - \sigma_2)^2 + (\sigma_2 - \sigma_3)^2 + (\sigma_{33} - \sigma_{11})^2] = k^2 \tag{7.2}$$

Constant k is to be determined from the experiment and σ is the stress tensor.

In uniaxial stress this equation is reduced to

$$\frac{\sigma_y^2}{3} = k^2 \tag{7.3}$$

So, in elastic limit equation 7.3 becomes

$$\frac{\sigma_y^2}{3} = k^2 \tag{7.4}$$

Thus,

$$\frac{1}{6}[(\sigma_1 - \sigma_2)^2 + (\sigma_2 - \sigma_3)^2 + (\sigma_3 - \sigma_1)^2] = \frac{\sigma_y^2}{3} \tag{7.5}$$

The von Mises stress is defined by,

$$\bar{\sigma} = 3k^2 \tag{7.6}$$

So, yield stress and von Mises are related by

$$\bar{\sigma} \geq \sigma_y \tag{7.7}$$

Thus the yielding occurs in uniaxial tension when the von Mises stress is greater than the yield stress [118]. And the failure in all the samples was occurred pretty soon after yielding. Thus von Mises stress during failure should nearly as same as the true uniaxial stress that were obtained during the uniaxial tensile test failure in the real experiments. Optimum results were mainly obtained from C3D8 mesh type 0.8 mesh size simulation. So, in this study only 0.8 mesh size and C3D8 mesh type elements were used for the calculation.

7.5.2.1 Aluminium 7075

Figure 7.23 Von Mises stress showing the resemblance with the original data for alloy 1 experimental data (a) Von Mises stress just before the fracture (b) Von Mises stress after the fracture.

Von Mises stress in figure 7.23 resembles the true stress data from the experiment. Thus, it validates the simulation results. True stress during failure was 894 MPa in the simulation and in the experiments the true stress near the failure was also around 900 MPa (figure 7.24). Here, this high stress was contributed by η' precipitates that was discussed in section 4.8. and the low plastic strain can be attributed to the obtained brittle nature due to the addition of alloying elements which created brittle intermetallics like Al_2CuMg and other types of intermetallics which generally acts as fracture nucleation sites [54,84].
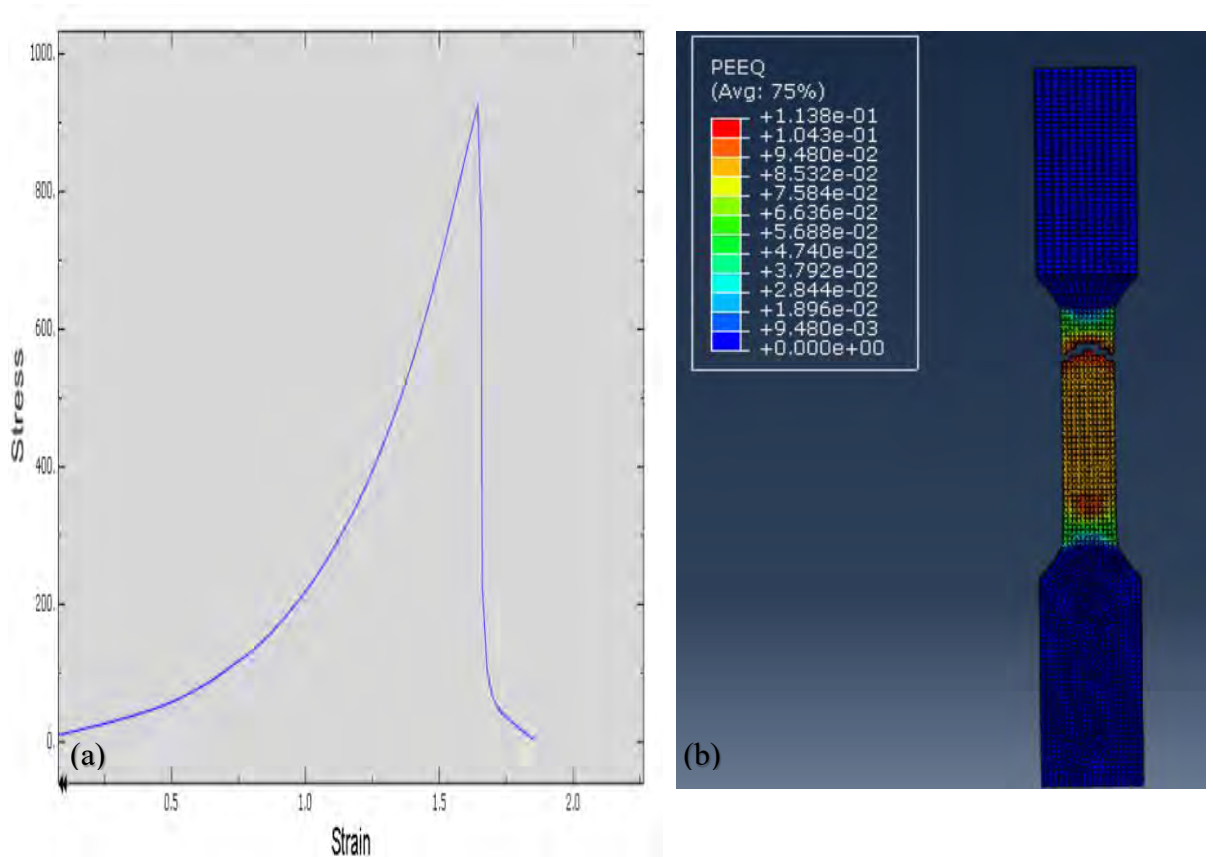
Figure 7.24 (a)True stress and true strain graph from the experiment (b) Equivalent plastic strain at the time of failure.

7.5.2.2   Ni added Al 7075

Again the same methodology was used to determine the feasibility of the simulation model. C3D8 0.8 mesh sizes were used for the simulation model. Von Mises stress was near 1378 MPa before failure as showed in figure 7.25(a). True stress near failure during the experiment was also near 1400 MPa as seen from the figure 7.26(a). Higher stress this time came from both η' phases and from the Al-Cu-Ni intermetallics as explained in chapter 4.
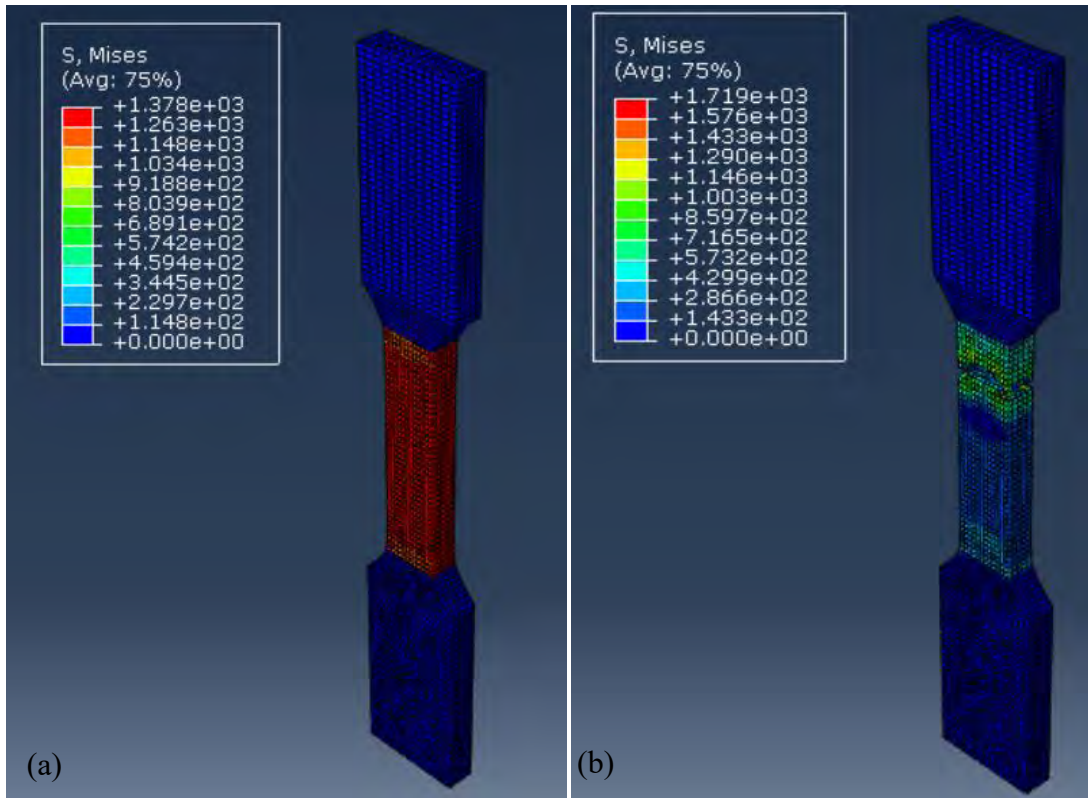
Figure 7.25 Von Mises showing the resemblance with the original data with the alloy 2 experimental data (a) Von Mises stress just before the fracture (b) Von Mises stress after the fracture.
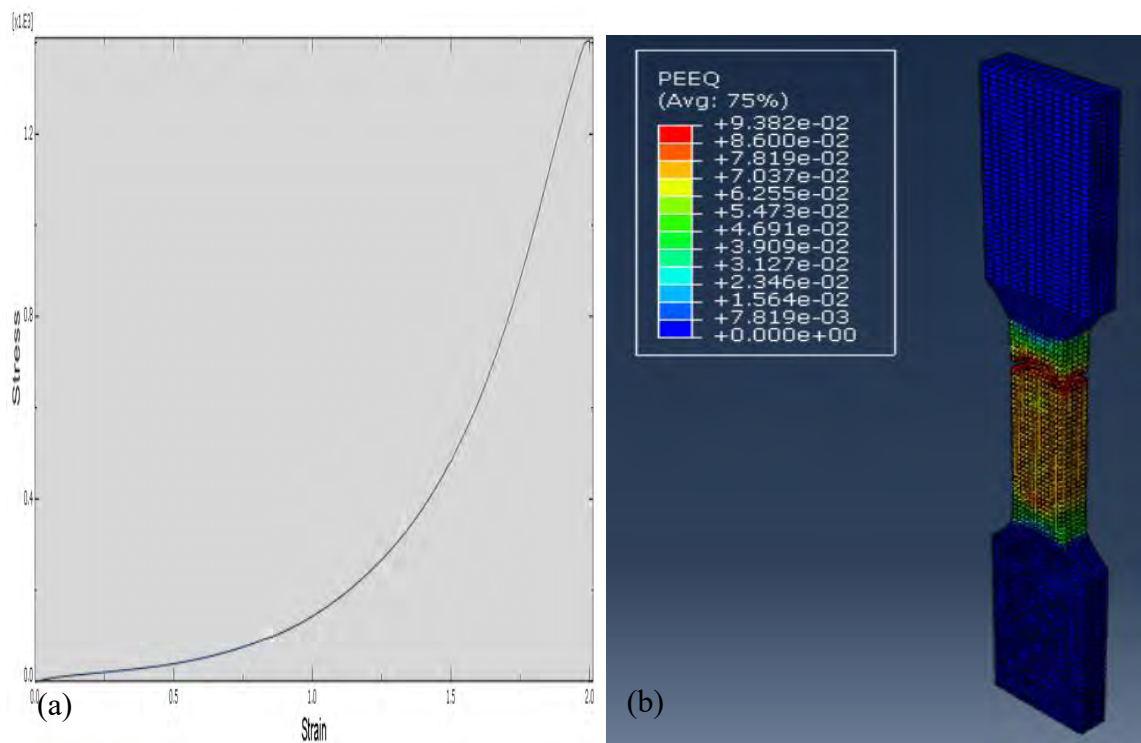
Figure 7.26 (a) True stress and true strain graph from the experiment of Ni added Al 7075 (b) Equivalent plastic strain at the time of failure.

7.5.2.3 Ni and B added Al 7075

As shown in figure 7.27(a) von Mises stress was 1220 MPa before failure. The failure true stress from the graph was also found to be around 1400 MPa (figure 7.28). This high stress was attributed to the formation of η' phase and tougher Al-Ni-Cu intermetallics as it was in alloy 2. Thus Ni and B added Al alloy simulation also validated from the von Mises stress data comparison. As von Mises during failure in a uniaxial test is nearly same as the stress during the experiment, the von Mises stress during the failure agree with the experiment. The plastic strain was in the simulation 0.11 as shown in figure 7.28(b) and which is 5.5% of the true strain. This high increase in plastic strain in comparison to the alloy 1 and alloy 2 was due to the boron addition which made the distribution of the intermetallics finely dispersed. Thus increased overall toughness.
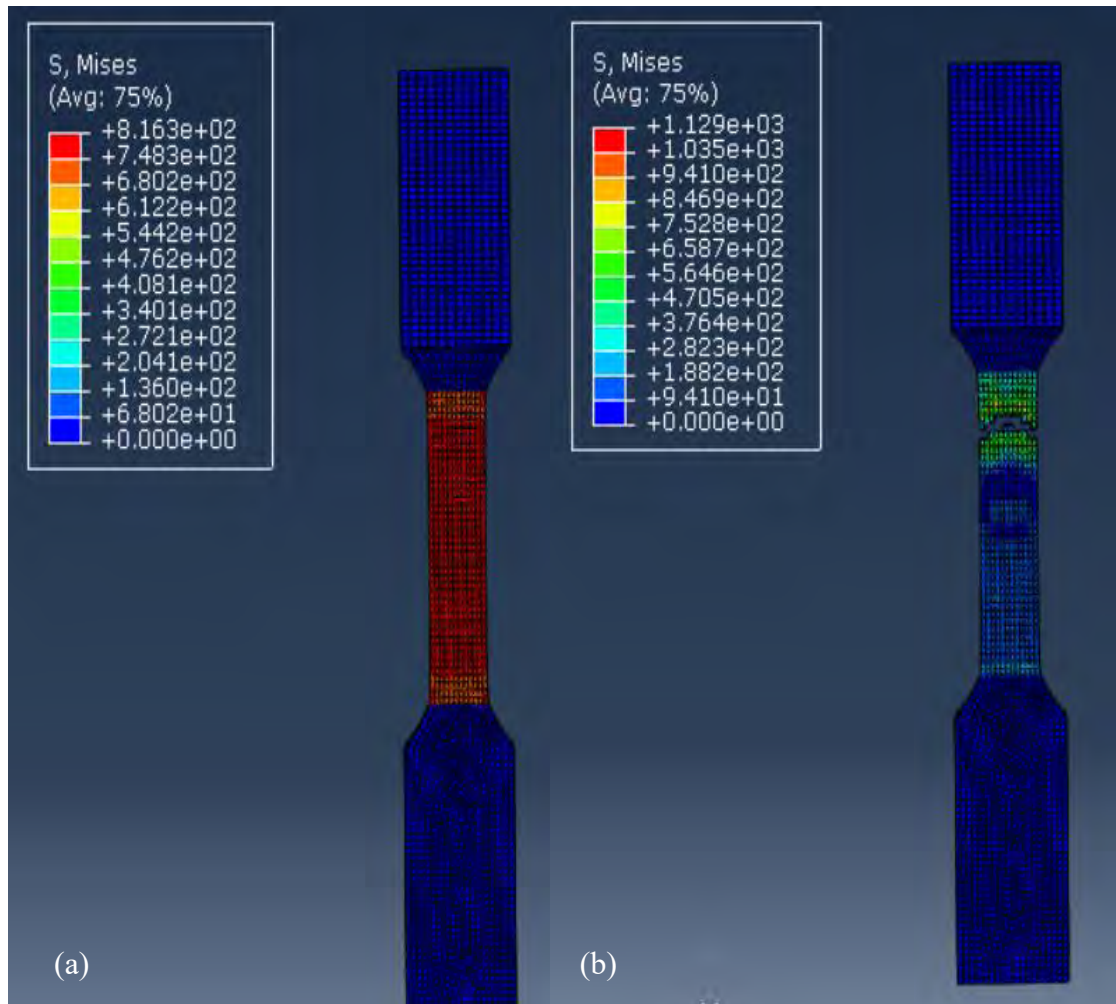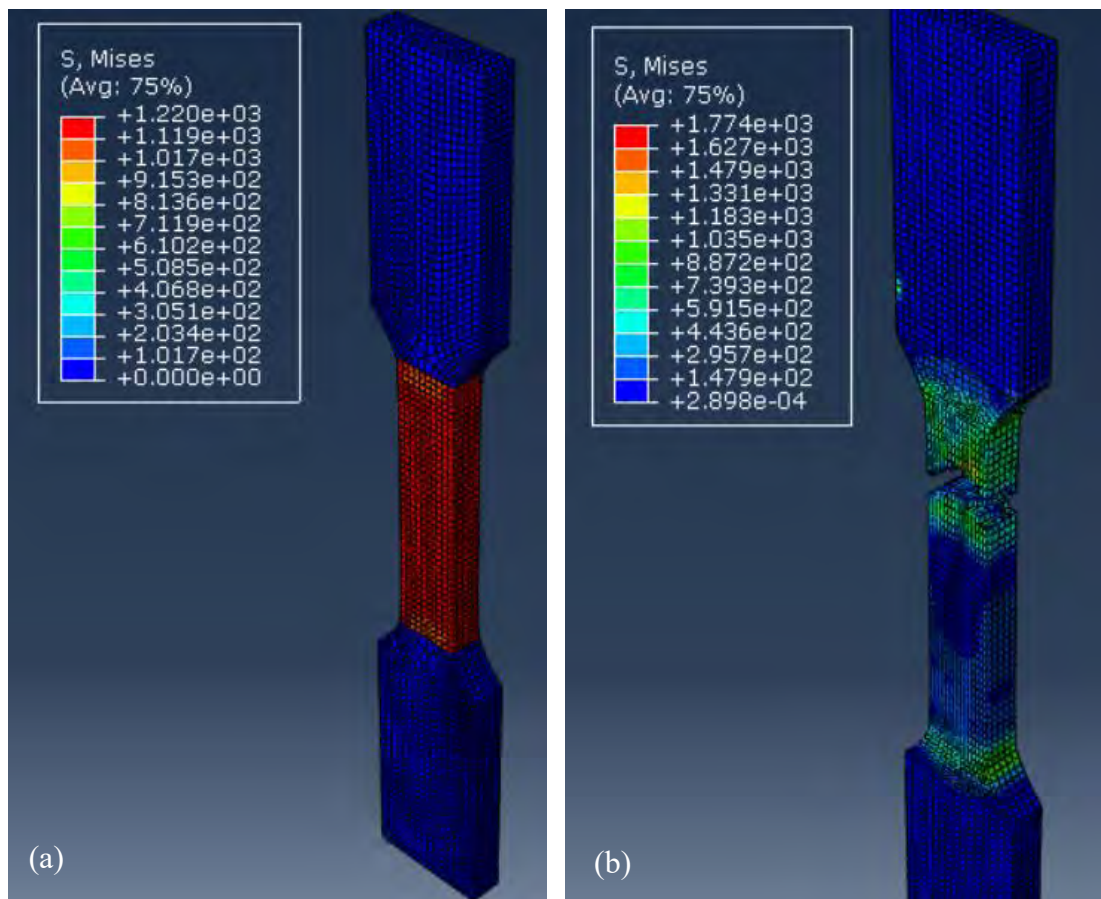

Figure 7.27 Von Mises showing the resemblance of the original data with alloy 3 experimental data (a) Von Mises stress just before the fracture (b) Von Mises stress after the fracture.
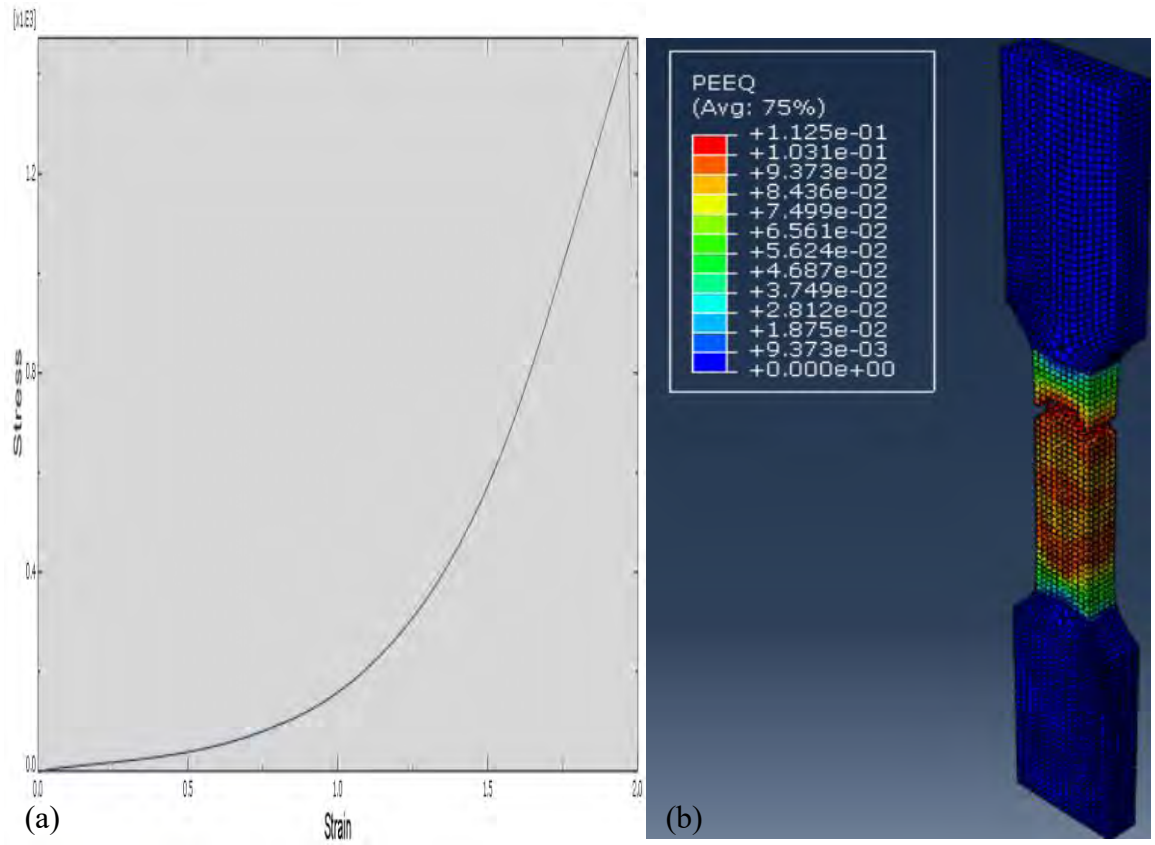
Figure 7.28 (a) True stress and true strain graph from the experiment (b) Equivalent plastic strain at the time of failure.

7.5.3 Stress Triaxiality

7.5.3.1 Al 7075

From figure 7.29 it can be seen that the stress triaxiality varied in different points. Points near the failure region had experienced stress triaxiality near 1.75. The stress triaxiality was very high where lowest plastic deformation could take place. Thus, high stress triaxiality can be attributed to the origin of the fracture in alloy 1.
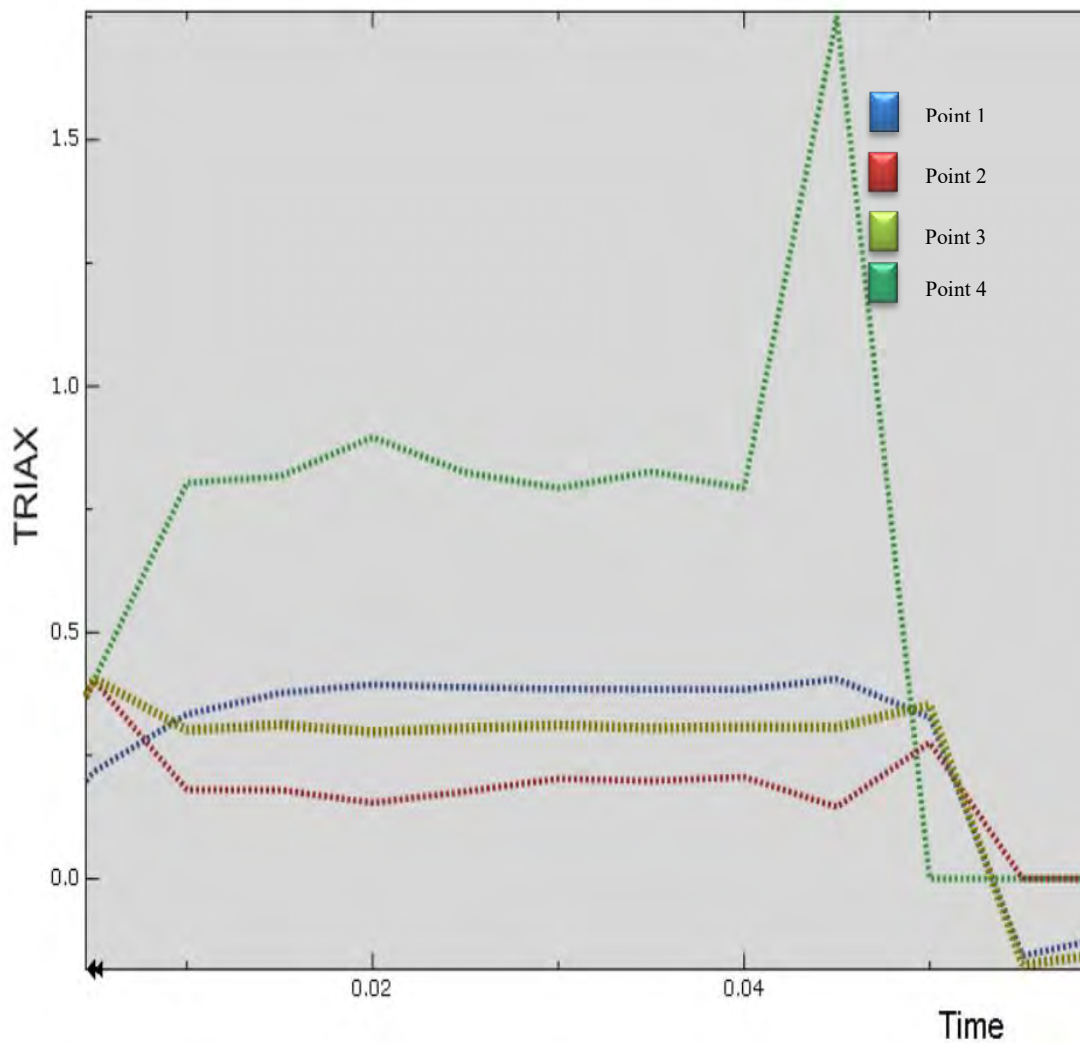
Figure 7.29 Stress triaxiality at different points taken from Al 7075 simulation run with 0.8 mesh size and C3D8 mesh type

7.5.3.2 Ni Added Al 7075

Figure 7.30 describes how stress triaxiality varied over the time span during the simulation analysis. Between point 2 and point 3, point 2 had increased stress triaxiality during failure. Point 1 and 4 both experienced high triaxiality but failure occurred at point 1 as at that point the sample could not accommodate the plastic strain.
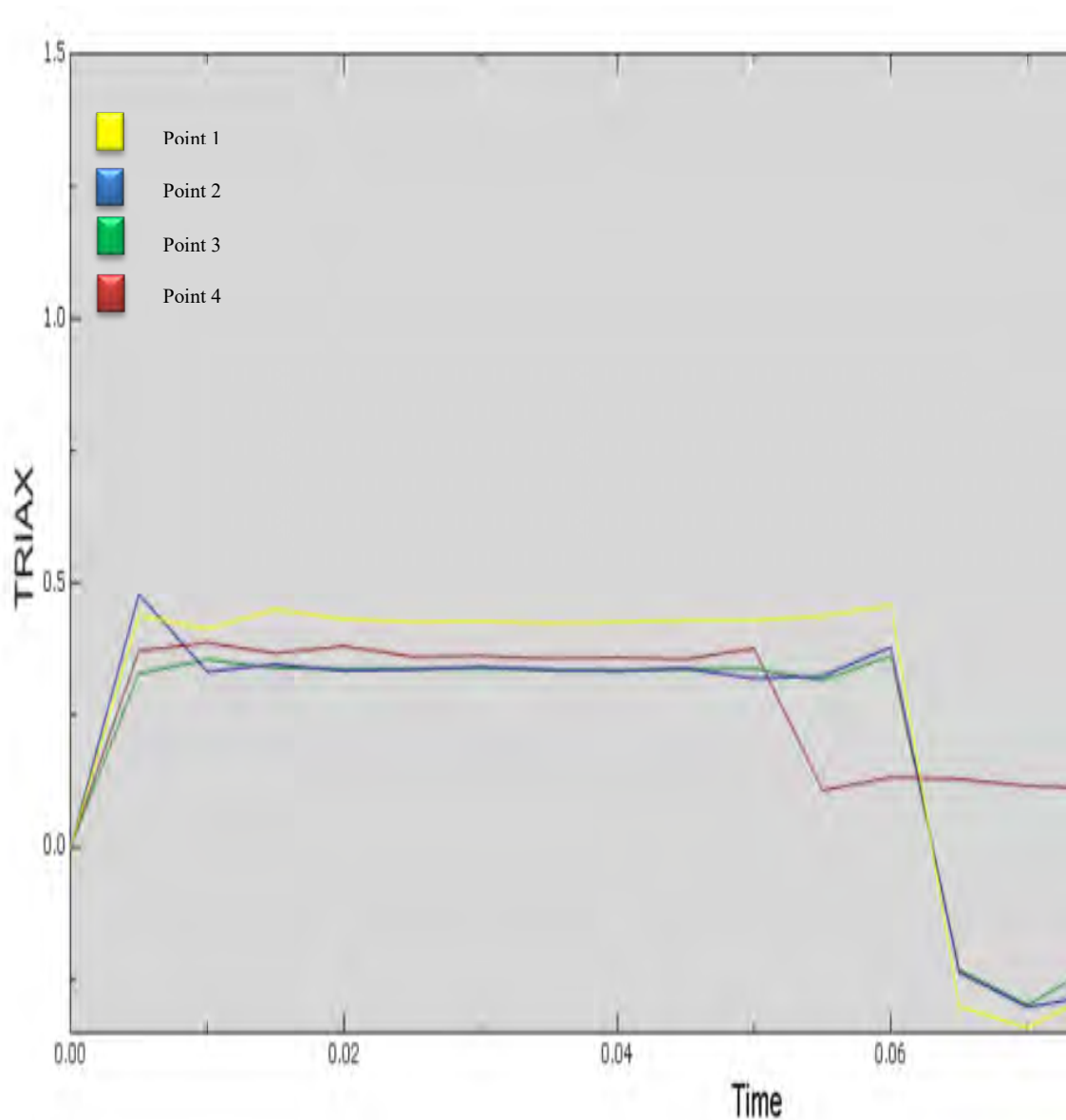
Figure 7.30 Stress triaxiality at different points taken from Ni added Al 7075 simulation run with 0.8 mesh size and C3D8 mesh type.

7.5.3.3 Ni and B added Al 7075

Figure 7.31 shows the stress triaxiality for Ni and B added Al 7075 alloy. Points near the fracture (point 1) had higher stress triaxiality throughout necking and failure. Point 4 on the other hand had lowest stress triaxiality as it could elongate freely. Point 2 and point 3 had experienced similar stress triaxiality except for the fact that point 2 experienced a bit higher stress triaxiality than the later one.
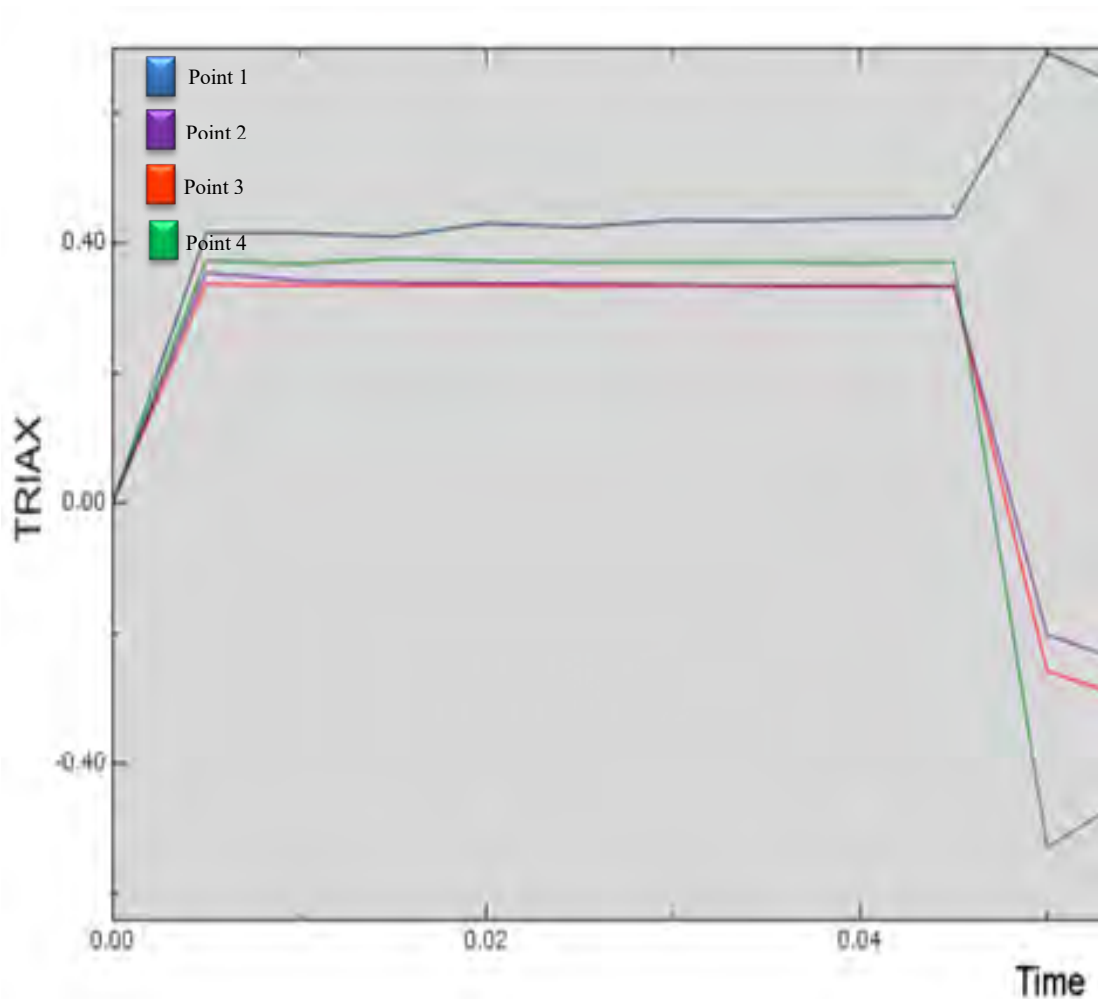
Figure 7.31 Stress triaxiality at different points taken from Ni and B added Al 7075 simulation run with 0.8 mesh size and C3D8 mesh type.

In the three simulations on average the center points had higher stress triaxiality than the points at the situated at the edge. Also, the points near the fracture in all three fracture simulation had the highest stress triaxiality but the points that were symmetrical but at the opposite end had the lowest stress triaxiality. This is because the stress triaxiality increases as the plastic deformation become more difficult [119]. Since, the failure could have occurred in both places point 1 and point 4, both had

experienced void growth and coalescence, and the resistance to the plastic deformation. Thus stress was not uniform in the specimen after necking started. The stress distribution here is characterized by Bridgman's evaluations where stress distribution is a function of the negative surface curvature at the periphery of the necked section. In one case failure occurred due to high stress triaxiality and in another place stress triaxiality increase was offset by plastic deformation. This agrees with the experimental data of provided by Bao and Wierzbicki [100, 101].

7.6 Summary

Experimental data were used to create the simulation of the tensile test. From the simulation data it was found that the most of the failure showed same fractography as the original test. Among them 0.4 mesh sizes with C3D8R mesh type and 0.8 mesh sizes with C3D8 mesh type gave the best results that are identical to the real experiments. 0.4 mesh sizes with C3D8 mesh type also gave identical results but they tended to be shear locked due to its over fineness.

Decrease of mesh sizes increased the quality of the failure appearance but decreasing mesh sizes increased the computational time. Use of C3D8 against C3D8R also increased time exponentially as more equations were involved. Average Time required for C3D8 0.8 mesh sizes (26605.06 CPU time in seconds) is much less than C3D8R 0.4 Mesh sizes (50656.03 CPU time in seconds) although they provided similar results. Thus a tradeoff between quality and cost of time had to enforce. It was found that element with 0.8 mesh sizes with the C3D8 mesh type gave the optimum results.

Once the optimum mesh size and the mesh types were determined the simulations were tested for the von Mises stress and plastic strain with the real tensile test failure. The results in the simulation and the original test failure showed similarities. Thus it confirmed the validity of the used ductile damage progressive failure algorithm through material stiffness degradation that was used for the failure simulation.

Stress triaxiality ratio change with ductile damage failure algorithm was also studied. Stress triaxiality is a function of free flow of plastic deformation. In places where fracture occurred high amount of stress triaxiality was obtained just before the fracture. Also, center elements had showed higher stress triaxiality than the elements that were situated on the edge. These findings also confirmed the validity of the simulation.

CHAPTER 8
Conclusion and Recommendation

8.1 Conclusion

The aim of this thesis was to develop a proper tensile test simulation method of Al 7075 alloys until failure using the experimental data with progressive failure algorithm and to establish structure-property relationship of these alloys. By doing so, several conclusions were reached during this thesis work and these are listed in the next paragraphs.

- All of the produced alloys had higher strength and toughness than the base metal aluminium preliminary due to the formation of the precipitated metastable η phases.

- Higher strength and ductility was found in the modified alloys having new compositions (i.e. alloy 2 and alloy 3) in the same production and experimental setups. These high strength and ductility were attributed to the improved casting, better distribution of harder and finer intermetallics.

- Using the proper experimental data, it was possible to perform the simulation of tensile test until failure of the three different alloys using ductile damage progressive failure algorithm.

- By considering the cost of simulation power in terms of computing time and the quality of the fractography the optimum solution was found by adopting 0.8 mesh size with C3D8 mesh type.

- Validation of the simulation results was achieved by comparing the von Mises stress with the true stress found in the experiment. In all the three simulation the von Mises stress that was obtained from the simulation matched with the experimental results.

- Study of the stress triaxiality variation gave insight how the failure progressed. Fracture sites showed high amount of stress triaxiality just before the failure. On the other hand, lower stress triaxiality was found at the edge in comparison with the stress triaxiality found at the center. All these results do agree with the

theoretical solution of the stress triaxiality. Thus stress triaxiality variations obtained in the simulation also validates the simulation method.

8.2 Recommendation

- Nickel addition in the alloys increased strength, hardness and ductility. As nickel addition formed hard nickel intermetallics; increase in hardness is easily assumable but how Ni addition did increase strength and toughness can be further investigated by varying nickel composition.

- Grain size and strength and ductility changed with the addition of boron. The relation between the properties and the composition with the addition of boron can be further studied.

- The finite element algorithm used to simulate the failure was ductile damage. There are several other algorithms built in Abaqus that can be used to simulate fracture (i.e. Johnson cook, FLD damage etc.). As a tensile failure simulation for aluminium alloys could be established using ductile damage method. It should be possible to implement other failure algorithm by following same procedure.

- Any practical structure experiences different types of loading such as shear, tension and compression. A full profile of aluminium 7075 alloy simulation until failure would allow engineers and researchers to mix these loading in different parts of the structure according to real scenario and anticipate how this would perform in the practical design. So, simulation until failure with shear and compression in addition with the tensile simulation and a suitable method to apply these loadings simultaneously into a specific part of the structure would be advantageous.

- For a dynamic problem Abaqus offers explicit and implicit solutions. In this thesis explicit solutions were explored for various simulations. Implicit methods can also be applied to obtain the simulation results. There might be scopes for implicit solutions as they are better and cost effective when there are a few number of nodes used. This relation with nodes and computational work is interesting to look further into.

- Elements near the failure zone showed high stress triaxiality before the fracture. Thus stress triaxialities may offer new research possibilities to enhance the efficiency of the structure design. I.e. voids growth pattern near high stress triaxiality and low stress triaxiality regions.

References

[1]   A. Heinz, A. Haszler, C. Keidel, S. Moldenhauer, R. Benedictus, and W. . Miller, "Recent development in aluminium alloys for aerospace applications," *Mater. Sci. Eng. A*, vol. 280, no. 1, pp. 102–107, Mar. 2000.

[2]   D. Weiss and O. Rios, "Low Density and Temperature Tolerant Alloys for Automotive Applications," in *SAE Technical Paper Series*, 2017.

[3]   K. R. Ramkumar, S. Sivasankaran, F. A. Al-Mufadi, S. Siddharth, and R. Raghu, "Investigations on microstructure, mechanical, and tribological behaviour of AA 7075–xwt.% TiC composites for aerospace applications," *Arch. Civ. Mech. Eng.*, vol. 19, no. 2, pp. 428–438, Mar. 2019. Çam, G., and Mistikoglu, S. (2014).

[4]   G. Çam and S. Mistikoglu, "Recent Developments in Friction Stir Welding of Al-alloys," *J. Mater. Eng. Perform.*, vol. 23, no. 6, pp. 1936–1953, Jun. 2014.

[5]   P. V. Liddicoat *et al.*, "Nanostructural hierarchy increases the strength of aluminium alloys," *Nat. Commun.*, vol. 1, no. 1, p. 63, Dec. 2010. Fang, H., Chao, H., and Chen, K. (2014).

[6]   H. C. Fang, H. Chao, and K. H. Chen, "Effect of Zr, Er and Cr additions on microstructures and properties of Al–Zn–Mg–Cu alloys," *Mater. Sci. Eng. A*, vol. 610, pp. 10–16, Jul. 2014.

[7]   F. Toptan, A. Kilicarslan, and I. Kerti, "The Effect of Ti Addition on the Properties of Al-B$_4$C Interface: A Microstructural Study," *Mater. Sci. Forum*, vol. 636–637, pp. 192–197, Jan. 2010.

[8]   J. M. Salman, K. F. Al-Sultani, and S. A. Abedulsada, "The Effect of Quenching in Polymer and Addition of 0.1% Zr on Properties of Al-5.6% Zn-2.5%Mg-1.6%Cu Alloy," *Appl. Mech. Mater.*, vol. 110–116, pp. 1305–1312, Oct. 2011.Belov, N., and Zolotorevskiy, V. (2002).

[9]   N. A. Belov and V. S. Zolotorevskiy, "The Effect of Nickel on the Structure, Mechanical and Casting Properties of Aluminium Alloy of 7075 Type," *Mater. Sci. Forum*, 2009.

[10]   A. R. Farkoosh, M. Javidani, M. Hoseini, D. Larouche, and M. Pekguleryuz, "Phase formation in as-solidified and heat-treated Al–Si–Cu–Mg–Ni alloys: Thermodynamic assessment and experimental investigation for alloy design," *J. Alloys Compd.*, vol. 551, pp. 596–606, Feb. 2013.

[11]   B. S. Murty, S. A. Kori, and M. Chakraborty, "Grain refinement of aluminium and its alloys by heterogeneous nucleation and alloying," *Int. Mater. Rev.*, vol. 47, no. 1, pp. 3–29, Feb. 2002.

[12]   T. H. Manjunatha, Y. Basavaraj, M. Nagaral, V. Venkataramana, and J. I. Harti, "Investigations on mechanical behavior of Al7075 - nano B 4 C composites," *IOP Conf. Ser. Mater. Sci. Eng.*, vol. 376, p. 012091, Jun. 2018.

[13]   A. El Amri, I. Hanafi, M. E. Y. Haddou, and A. Khamlichi, "Numerical simulation of damage evolution for ductile materials and mechanical properties study," *IOP Conf. Ser. Mater. Sci. Eng.*, vol. 100, p. 012060, Dec. 2015.

[14]   J. Lemaitre, "A Continuous Damage Mechanics Model for Ductils Fracture," *Trans. ASME, J. Eng. Mater. Technol.*, 1985.Xu, Q., N., Zhao, A., & Song, J. (2018).

[15]   Q. Xu, N. Zhang, A. Zhao, and J. Song, "Nonlinear Finite Element Analysis of Corrugated Steel Web Composite Beam Based on ABAQUS," *IOP Conf. Ser. Earth Environ. Sci.*, vol. 189, p. 022083, Nov. 2018.

[16]   A. Anandarajah, "Methods of Integrating Elasto-Plastic Constitutive Equations," in *Computational Methods in Elasticity and Plasticity*, New York, NY: Springer New York, 2010, pp. 339–374.

[17]   Y. Wang, Y. Zhou, and Y. Xia, "A constitutive description of tensile behavior for brass over a wide range of strain rates," *Mater. Sci. Eng. A*, vol. 372, no. 1–2, pp. 186–190, May 2004.

[18]   D. Samantaray, S. Mandal, and A. K. Bhaduri, "A comparative study on Johnson Cook, modified Zerilli-Armstrong and Arrhenius-type constitutive models to predict elevated temperature flow behaviour in modified 9Cr-1Mo steel," *Comput. Mater. Sci.*, 2009.

[19]   G. T. Gray, S. R. Chen, and K. S. Vecchio, "Influence of grain size on the constitutive response and substructure evolution of MONEL 400," *Metall. Mater. Trans. A Phys. Metall. Mater. Sci.*, 1999.

[20]   G. R. Johnson and W. H. Cook, "Fracture characteristics of three metals subjected to various strains, strain rates, temperatures and pressures," *Eng. Fract. Mech.*, 1985.

[21]   T. Mirzaie, H. Mirzadeh, and J. M. Cabrera, "A simple Zerilli-Armstrong constitutive equation for modeling and prediction of hot deformation flow stress of steels," *Mech. Mater.*, 2016.

[22]   C. Hernandez, A. Maranon, I. A. Ashcroft, and J. P. Casas-Rodriguez, "A computational determination of the Cowper-Symonds parameters from a single Taylor test," *Appl. Math. Model.*, 2013.

[23]   A. K. Maheshwari, K. K. Pathak, N. Ramakrishnan, and S. P. Narayan, "Modified Johnson–Cook material flow model for hot deformation processing," *J. Mater. Sci.*, vol. 45, no. 4, pp. 859–864, Feb. 2010.

[24]   J. Džugan, M. Španiel, A. Prantl, P. Konopík, J. Růžička, and J. Kuželka, "Identification of ductile damage parameters for pressure vessel steel," *Nucl. Eng. Des.*, vol. 328, pp. 372–380, Mar. 2018.

[25]   R. Kiran and K. Khandelwal, "A triaxiality and Lode parameter dependent ductile fracture criterion," *Eng. Fract. Mech.*, vol. 128, pp. 121–138, Sep. 2014.

[26]   J. Ruzicka, M. Spaniel, A. Prantl, J. Dzugan, J. Kuzelka, and M. Moravec, "Identification of Ductile Damage Parameters in the Abaqus," *Bull. Appl. Mech.*, 2012.

[27]   A. Dutt, "Effect of Mesh Size on Finite Element Analysis of Beam," *Int. J. Mech. Eng.*, vol. 2, no. 12, pp. 8–10, Dec. 2015.Anandarajah, A. 2010.

[28]   R. Cobden and A. Banbury, "Aluminium: Physical Properties, Characteristics and Alloys," *Talal*, 1994.

[29]   R. Donahue and P. A. Fabiyi, "Manufacturing Feasibility of All-Aluminum Automotive Engines Via Application of High Silicon Aluminum Alloy," in *SAE Technical Papers*, 2000.

[30]   H. Yoshimura *et al.*, "Study on near dry machining of aluminum alloys," in *LEM 2005 - 3rd International Conference on Leading Edge Manufacturing in 21st Century*, 2005.

[31]   Steel and aluminum, quo vadis? A pathway to growth in challenging times. (2017, February 17). Retrieved from https://www.strategyand.pwc.com/report/steel-and-aluminum.

[32]   H. Ammar, Influence of metallurgical parameters on the mechanical properties and quality indices of Al-Si-Cu-Mg and Al-Si-Mg casting alloys. [Chicoutimi]: Universit. du Québec à Chicoutimi, 2010.

[33] H. R. Ammar, A. M. Samuel, F. H. Samuel, E. Simielli, G. K. Sigworth, and J. C. Lin, "Influence of Aging Parameters on the Tensile Properties and Quality Index of Al-9 Pct Si-1.8 Pct Cu-0.5 Pct Mg 354-Type Casting Alloys," *Metall. Mater. Trans. A*, vol. 43, no. 1, pp. 61–73, Jan. 2012.

[34] P. S. Bulson, "Aluminium structures - a guide to their specifications and design," *Eng. Struct.*, 1996.

[35] *Couplages entre pr. cipitation et plasticité dans un alliage daluminium 7xxx: Application à des traitements thermomécaniques de réduction des distorsions dans des composants aéronautiques* (Unpublished master's thesis). Thèse de doctorat: Matériaux, mécanique, génie civil, électrochimie: Grenoble INPG.

[36] G. Mathers, *The welding of aluminium and its alloys*. Woodhead Publishing Limited, 2002.

[37] Z. Ahmad, *Principles of Corrosion Engineering and Corrosion Control*. 2006.

[38] W. D. Callister and D. G. Rethwisch, *Materials Sciences and an Engineering Introduction*. 2014.

[39] J. R. Davis, "Light Metals and Alloys," *Alloy. Underst. Basics*, 2001. H. E.

[40] H. E. Boyer, "Heat Treating of Nonferrous Alloys," *Metallogr. Microstruct. Anal.*, vol. 2, no. 3, pp. 190–195, Jun. 2013.

[41] J. G. Kaufman, *Introduction to Aluminium Alloys and Tempers*. 2000.

[42] Aluminum Alloys – Effects of Alloying Elements. (2002, September). Retrieved from http://www.totalmateria.com/Article55.htm.

[43] L. Sobrin, Predictions of precipitation reaction mechanisms for 7xxx series aluminum alloys cast by CDS technique (master's thesis). University of Windsor.2014.

[44] L. K. Berg *et al.*, "GP-zones in Al-Zn-Mg alloys and their role in artificial aging," *Acta Mater.*, 2001. Waterloo, G., Hansen, V., Gjønnes, J., & Skjervold, S. R. (2001).

[45] G. Waterloo, V. Hansen, J. Gjønnes, and S. R. Skjervold, "Effect of predeformation and preaging at room temperture in Al-Zn-Mg-(Cu,Zr) alloys," *Mater. Sci. Eng. A*, 2001.

[46] J. D. Embury and R. B. Nicholson, "The nucleation of precipitates: The system Al-Zn-Mg," *Acta Metall.*, 1965.

[47] A. J. Ardell, "Precipitation hardening," *Metall. Trans. A*, 1985.

[48] M. J. Starink and S. C. Wang, "A model for the yield strength of overaged Al–Zn–Mg–Cu alloys," *Acta Mater.*, vol. 51, no. 17, pp. 5131–5150, Oct. 2003.

[49] A. Garg, Y. C. Chang, and J. M. Howe, "Precipitation of the Ω phase in an Al-4.0Cu-0.5Mg alloy," *Scr. Metall. Mater.*, 1990.

[50] I. J. Polmear, "The Influence of Small Additions of Silver on the Structure and Properties of Aged Aluminum Alloys," *JOM*, 1968.

[51] K. Matsuda, K. Kido, T. Kawabata, Y. Uetani, and S. Ikeno, "Effects of Cu, Ag and Au addition on total elongation and fracture morphology in Al-Mg-Si alloys," *Keikinzoku/Journal Japan Inst. Light Met.*, 2003.

[52] Computational Thermodynamics Calculation of Phase Diagrams using the CALPHAD Method. Retrieved from www.calphad.com/phase_diagrams.html

[53] J. E. Hatch, "Aluminum Properties and Physical Metallurgy," In *ASM ,Ohio, US*. 1984.

[54] L. F. Mondolfo, "Aluminum Alloys: Structure and properties," *Butterworths*. 1976.

[55]   S. P. Ringer, W. Yeung, B. C. Muddle, and I. J. Polmear, "Precipitate stability in AlCuMgAg alloys aged at high temperatures," *Acta Metall. Mater.*, 1994.

[56]   J. D. Robson, "Microstructural evolution in aluminium alloy 7050 during processing," *Mater. Sci. Eng. A*, vol. 382, no. 1–2, pp. 112–121, Sep. 2004.

[57]   H. Luffler, I. Kovacs, and J. Lendvai, "Decomposition processes in Al-Zn-Mg alloys," *J. Mater. Sci.*, vol. 18, no. 8, pp. 2215–2240, Aug. 1983.

[58]   P. N. Unwin, G. Lorimer, and R. Nicholson, "The origin of the grain boundary precipitate free zone," *Acta Metall.*, vol. 17, no. 11, pp. 1363–1377, Nov. 1969.

[59]   J. Martin, "The microstructure of precipitation-hardened alloys," in *Precipitation Hardening*, Elsevier, 1998, pp. 1–78.

[60]   I. Polmear, D. St. John, J. F. Nie, and M. Qian, *Light Alloys: Metallurgy of the Light Metals: Fifth Ed.* 2017.

[61]   G. E. Dieter, *Mechanical metallurgy.* New York,: McGraw-Hill, 1961.

[62]   R. Nicholson, G. Thomas, & J. Nutting, Electron-microscopic studies of precipitation in aluminum alloys. ," Journal of the Institute of Metals, 87, 429-438. 1959.

[63]   R. B. Nicholson, G. Thomas, & J. Nutting, The interaction of dislocations and precipitates. *Acta Metallurgica.* https://doi.org/10.1016/0001-6160(60)90125-5.1960.

[64]   E. Orowan, "Fracture and strength of solids," *Reports Prog. Phys.*, vol. 12, no. 1, p. 309, Jan. 1949.

[65]   N. Hansen, "Polycrystalline strengthening," *Metall. Trans. A*, vol. 16, no. 12 , Dec. 1985.

[66]   A. H. Cottrell and D. L. Dexter, "Dislocations and Plastic Flow in Crystals," *Am. J. Phys.*, vol. 22, no. 4, pp. 242–243, Apr. 1954.

[67]   D. Godard, P. Archambault, E. Aeby-Gautier, and G. Lapasset, "Precipitation sequences during quenching of the AA 7010 alloy," *Acta Mater.*, vol. 50, no. 9, pp. 2319–2329, May 2002.

[68]   F. Xie *et al.*, "A study of microstructure and microsegregation of aluminum 7050 alloy," *Mater. Sci. Eng. A*, vol. 355, no. 1–2, pp. 144–153, Aug. 2003.

[69]   J. D. Robson and P. B. Prangnell, "Dispersoid precipitation and process modelling in zirconium containing commercial aluminium alloys," *Acta Mater.*, vol. 49, no. 4, pp. 599–613, Feb. 2001.

[70]   X. Fan, D. Jiang, Q. Meng, B. Zhang, and T. Wang, "Evolution of eutectic structures in Al-Zn-Mg-Cu alloys during heat treatment," *Trans. Nonferrous Met. Soc. China*, vol. 16, no. 3, pp. 577–581, Jun. 2006.

[71]   D. Dumont, A. Deschamps, Y. Bréchet, C. Sigli, and J. C. Ehrström, "Characterisation of precipitation microstructures in aluminium alloys 7040 and 7050 and their relationship to mechanical behaviour," *Mater. Sci. Technol.*, vol. 20, no. 5, pp. 567–576, May 2004.

[72]   A. Guinier, "Structure of Age-Hardened Aluminium-Copper Alloys," *Nature*, vol. 142, no. 3595, pp. 569–570, Sep. 1938.

[73]   G. D. Preston, "Structure of Age-Hardened Aluminium-Copper Alloys," *Nature*, vol. 142, no. 3595, pp. 570–570, Sep. 1938.

[74]   L. Berg *et al.*, "GP-zones in Al–Zn–Mg alloys and their role in artificial aging," *Acta Mater.*, vol. 49, no. 17, pp. 3443–3451, Oct. 2001.

[75] X. Z. Li, V. Hansen, J. GjØnnes, and L. R. Wallenberg, "HREM study and structure modeling of the η′ phase, the hardening precipitates in commercial Al–Zn–Mg alloys," *Acta Mater.*, vol. 47, no. 9, pp. 2651–2659, Jul. 1999.

[76] M. Murayama and K. Hono, "Pre-precipitate clusters and precipitation processes in Al–Mg–Si alloys," *Acta Mater.*, vol. 47, no. 5, pp. 1537–1548, Mar. 1999.

[77] T. Engdahl, V. Hansen, P. Warren, and K. Stiller, "Investigation of fine scale precipitates in Al–Zn–Mg alloys after various heat treatments," *Mater. Sci. Eng. A*, vol. 327, no. 1, pp. 59–64, Apr. 2002.

[78] N. Q. Chinh, J. Lendvai, D. H. Ping, and K. Hono, "The effect of Cu on mechanical and precipitation properties of Al–Zn–Mg alloys," *J. Alloys Compd.*, vol. 378, no. 1–2, pp. 52–60, Sep. 2004.

[79] A. Abolhasani, A. Zarei-Hanzaki, H. R. Abedi, and M. R. Rokni, "The room temperature mechanical properties of hot rolled 7075 aluminum alloy," *Mater. Des.*, vol. 34, pp. 631–636, Feb. 2012.

[80] S. P. Bathurst and S. G. Kim, "Designing direct printing process for improved piezoelectric micro-devices," *CIRP Ann.*, vol. 58, no. 1, pp. 193–196, 2009.

[81] G. Srikant, N. Chollacoop, and U. Ramamurty, "Plastic strain distribution underneath a Vickers Indenter: Role of yield strength and work hardening exponent," *Acta Mater.*, vol. 54, no. 19, pp. 5171–5178, Nov. 2006.

[82] K. Mills, *Metals handbook*. Metals Park, OH: American Society for Metals.1985.

[83] M. Tajally and E. Emadoddin, "Mechanical and anisotropic behaviors of 7075 aluminum alloy sheets," *Mater. Des.*, vol. 32, no. 3, pp. 1594–1599, Mar. 2011.

[84] A. J. Morris, R. F. Robey, P. D. Couch, and E. De los Rios, "A Comparison of the Damage Tolerance of 7010 T7451 and 7050 T7451," *Mater. Sci. Forum*, vol. 242, pp. 181–186, Jan. 1997.

[85] C. L. Chen, G. D. West, and R. C. Thomson, "Characterisation of Intermetallic Phases in Multicomponent Al-Si Casting Alloys for Engineering Applications," *Mater. Sci. Forum*, vol. 519–521, pp. 359–364, Jul. 2006.

[86] S. Tougaard, "Algorithm for automatic x-ray photoelectron spectroscopy data processing and x-ray photoelectron spectroscopy imaging," *J. Vac. Sci. Technol. A Vacuum, Surfaces, Film.*, vol. 23, no. 4, pp. 741–745, Jul. 2005.

[87] S. Tougaard and B. Jørgensen, "Inelastic background intensities in XPS spectra," *Surf. Sci.*, vol. 143, no. 2–3, pp. 482–494, Aug. 1984.

[88] H.-M. Tung, J.-H. Huang, D.-G. Tsai, C.-F. Ai, and G.-P. Yu, "Hardness and residual stress in nanocrystalline ZrN films: Effect of bias voltage and heat treatment," *Mater. Sci. Eng. A*, vol. 500, no. 1–2, pp. 104–108, Jan. 2009.

[89] S. Rai, B. . Choudhary, T. Jayakumar, K. B. S. Rao, and B. Raj, "Characterization of low cycle fatigue damage in 9Cr–1Mo ferritic steel using X-ray diffraction technique," *Int. J. Press. Vessel. Pip.*, vol. 76, no. 5, pp. 275–281, Apr. 1999.

[90] D. Richard and P. N. Adler, "Calorimetric studies of 7000 series aluminum alloys: I. Matrix precipitate characterization of 7075," *Metall. Trans. A*, vol. 8, no. 7, pp. 1177–1183, Jul. 1977.

[91] D. J. Lloyd and M. C. Chaturvedi, "A calorimetric study of aluminium alloy AA-7075," *J. Mater. Sci.*, vol. 17, no. 6, pp. 1819–1824, Jun. 1982.

[92] E. O. Hall, "The Deformation and Ageing of Mild Steel: III Discussion of Results," *Proc. Phys. Soc. Sect. B*, vol. 64, no. 9, pp. 747–753, Sep. 1951.

[93] T. L. Anderson, *Fracture Mechanics: Fundamentals and Applications, Fourth Edition*. 2017.

[94] X. Gao, T. Zhang, J. Zhou, S. M. Graham, M. Hayden, and C. Roe, "On stress-state dependent plasticity modeling: Significance of the hydrostatic stress, the third invariant of stress deviator and the non-associated flow rule," *Int. J. Plast.*, vol. 27, no. 2, pp. 217–231, Feb. 2011.

[95] R. von Mises, "Mechanik der festen Körper im plastisch-deformablen Zustand," *Nachrichten von der Gesellschaft der Wissenschaften zu Göttingen, Math. Klasse*, 1913.

[96] Y. Bai, X. Teng, and T. Wierzbicki, "On the Application of Stress Triaxiality Formula for Plane Strain Fracture Testing," *J. Eng. Mater. Technol.*, vol. 131, no. 2, Apr. 2009.

[97] F. A. McClintock, "A Criterion for Ductile Fracture by the Growth of Holes," *J. Appl. Mech.*, vol. 35, no. 2, pp. 363–371, Jun. 1968.

[98] J. R. Rice and D. M. Tracey, "On the ductile enlargement of voids in triaxial stress fields∗," *J. Mech. Phys. Solids*, vol. 17, no. 3, pp. 201–217, Jun. 1969.

[99] Simulia 3DS, "Abaqus Analysis User's Manual (version 6.12)," *University of Cambridge - Faculty of Mathematics*, 2015.

[100] Y. Bao, "Prediction of ductile crack formation in uncracked bodies," *PhD Thesis*, 2003.

[101] Y. Bao and T. Wierzbicki, "On fracture locus in the equivalent strain and stress triaxiality space," *Int. J. Mech. Sci.*, 2004.

[102] Y. Bai and T. Wierzbicki, "A new model of metal plasticity and fracture with pressure and Lode dependence," *Int. J. Plast.*, vol. 24, no. 6, pp. 1071–1096, Jun. 2008.

[103] Y. Bao and T. Wierzbicki, "On the cut-off value of negative triaxiality for fracture," *Eng. Fract. Mech.*, vol. 72, no. 7, pp. 1049–1069, May 2005.

[104] P. Bridgman, "Studies in Large Plastic Flow and Fracture: With Special Emphasis on the Effects of Hydrostatic Pressure," *New York-London McGraw-Hill*, 1952.

[105] Dassault Systèmes, "Manual Abaqus 6.14," *Documentation*, 2014.

[106] Choosing between explicit and implicit analysis. In *Dassault Systemes. Abaqus 6.14 Online Documentation*.

[107] Advantages of the explicit time integration method *Dassault Systemes. Abaqus 6.14 Online Documentation.*

[108] Cost of mesh refinement in implicit and explicit analyses *Dassault Systemes. Abaqus 6.14 Online Documentation*

[109] Hibbett, Karlsson, & Sorensen. (1998). Abaqus/standard: User's Manual. In *Inc. vols* (Vol. 1).

[110] R. D. Cook and H. Saunders, "Concepts and Applications of Finite Element Analysis (2nd Edition)," *J. Press. Vessel Technol.*, vol. 106, no. 1, pp. 127–127, Feb. 1984.

[111] CalculiX CrunchiX user's manual version 2.7. [cited 2019Oct22]. Available from: http://web.mit.edu/calculix_v2.7/CalculiX/ccx_2.7/doc/ccx/ccx.html

[112] ESI-Group: The Virtual Space Try Out Company. "FEM-FDM". [powerpoint slides] Available from: http://www.delcamural.ru/files/R007%20FEM-FDM.pdf.

[113] M. R. Mudge, L. Lapidus, and G. F. Pinder, "Numerical Solution of Partial Differential Equations in Science and Engineering," *Math. Gaz.*, vol. 84, no. 499, p. 187, Mar. 2000.

[114]   O. Zienkiewicz, R. Taylor, and J. Z. Zhu, *The Finite Element Method: its Basis and Fundamentals*. Elsevier, 2013.

[115]   Y. Kimura and D. P. Pope, "Ductility and toughness in intermetallics," *Intermetallics*, vol. 6, no. 7–8, pp. 567–571, Jan. 1998.

[116]   Q. G. Wang, "Microstructural Effects on the Tensile and Fracture Behavior of Aluminum Casting Alloys A356/357." *Metallurgical and Materials Transactions A: Physical Metallurgy and Materials Science*, pp. 2887–2899, 2003.

[117]   H. T. Naeem, K. S. Mohammed, K. R. Ahmad, and A. Rahmat, "The Influence of Nickel and Tin Additives on the Microstructural and Mechanical Properties of Al-Zn-Mg-Cu Alloys," *Adv. Mater. Sci. Eng.*, vol. 2014, pp. 1–10, 2014.

[118]   A. E. Green and R. Hill, "The Mathematical Theory of Plasticity," *Math. Gaz.*, vol. 35, no. 313, p. 208, Sep. 1951.

[119]   G. Maresca, P. Milella, and G. Pino, "A critical review of triaxiality based failure criteria," *Convegno IGF XIII*, 1997.